1-1-2015

Identification of High Energy Cosmic Ray Electrons Using Advanced Techniques in CALET and Fermi LAT

Aaron James Worley
University of Denver

Identification of High Energy Cosmic Ray Electrons using Advanced Techniques in CALET and Fermi LAT

A Dissertation

Presented to

the Faculty of Natural Sciences and Mathematics

University of Denver

in Partial Fulfillment

of the Requirements for the Degree

Doctor of Philosophy

by

Aaron J. Worley

November 2015

Advisor: Jonathan F. Ormes

Author: Aaron J. Worley

Title: Identification of High Energy Cosmic Ray Electrons using Advanced Techniques in CALET and Fermi LAT

Advisor: Jonathan F. Ormes

Degree Date: November 2015

Abstract

Measurements of the cosmic ray electron spectrum have received much attention over the last decade as anomalies in both electron and positron observations have been detected independently by several experiments. The profound possible implications in the fields of high energy astrophysics and particle physics have allowed for many interpretations on the origin of these inconsistencies in the spectra. This research focuses on two space-borne cosmic radiation experiments at different stages in their mission lifetimes: the Calorimetric Electron Telescope (CALET) and the Fermi Large Area Telescope (LAT). We explore the proton-electron discriminating capabilities of the CALET instrument through Monte Carlo simulations. Additionally, we present our efforts in electron identification using dedicated information of the tracking region of the LAT, exploiting calibration data from the beam test campaign. Within both studies, we employ multivariate techniques to improve the identification of cosmic ray electrons from the vast background.

Acknowledgements

I would like to start by thanking my dissertation advisor Dr. Jonathan F. Ormes, who has been an invaluable friend and mentor over the years. His endless knowledge, motivation, patience, and sense of humor has made my experience remarkable and one I will never forget. Thank you Jonathan, I am forever in your debt. I would also like to thank my committee members Dr. Davor Balzar, Dr. Robert Stencel, and Dr. Jennifer Hoffman for their advice and encouragement.

My sincere gratitude also goes to Dr. John F. Krizmanic and Dr. Alex Moiseev at Goddard Space Flight Center, who provided me an immense amount of support during my work with the collaborations. Furthermore, thank you to the friends I made at DU for sharing this journey with me.

Last but not least, I would like to thank my wife for always supporting me and for being by my side no matter what. Everything to this point I have done for myself, but I promise from here, everything I do will be for you and our son.

Table of Contents

List of Tables

List of Figures

Introduction

The centenary of the cosmic ray discovery was recently observed, though their study still presents some of the most important problems in the fields of physics and astrophysics. Fundamental questions regarding their origin remain open, continuing it's tradition of unveiling elementary aspects of our universe.

Figure i: Viktor F. Hess following a successful balloon expedition in 1912. Credit: `APS News.`

The existence of cosmic rays were uncovered in the fall of 1912, when an Austrian physicist by the name of Viktor F. Hess published his observations of a mysterious penetrating radiation "entering our atmosphere from above ..." [1] during his long series of high altitude balloon flights over the previous two years. His efforts provided the first definitive evidence of extraterrestrial ionizing radiation, though the true magnitude of this achievement would later be recognized. Nearly twenty years later, Carl Anderson discovered the first antimatter particle, the positron (or *negatron*), while investigating cosmic ray track in cloud chambers at the California Institute of Technology [2]. Following Anderson's finding, the nature of of "cosmic rays" was determined to be highly energetic particles, not in fact, gamma rays emanating from space. Viktor Hess and Carl Anderson equally shared the Nobel Prize in Physics

for their discoveries in 1936. Cosmic rays went on to play an instrumental role in the birth elementary particle physics, this natural source provided the only means at the time to study beyond the limits of the atom and resulted in the discoveries of the muon ($\mu^{\pm} - lepton$), pion ($\pi^{\pm} - meson$), and several other particles that occur in cosmic ray showers.

During the 1950s, the development of high performance particle accelerators in terrestrial laboratories guided the attention of high energy physicists away from the field of cosmic ray physics, allowing them to continue studying the growing particle *zoo* in a controlled environment. Additionally, with the emergence of the cosmic ray astrophysics field, investigation into the origin of cosmic radiation became more prevalent. The makeup of cosmic rays were already well established to be predominately hadronic at this time, though the existence of a cosmic ray electron component had been suspected from indirect evidence. In 1961, two independent observations offered the first definitive evidence of the existence of primary cosmic ray electrons; achieved concurrently by James Earl of the University of Minnesota [3], and by Peter Meyer and Rochus Vogt of the University of Chicago [4]. The discovery of the primary cosmic ray positron occurred a few years later in 1964, again by Peter Meyer, Roger Hildebrand of the University of Chicago and James DeShong at Argonne National Laboratory [5]. Despite the fact comic ray electrons[1] only contribute $\sim 2\%$[2] to the overall galactic cosmic ray composition, they provide invaluable information to the nature of comic rays and our local galactic space.

Over the last several years, we have seen a renewed excitement in the field of cosmic rays physics that has captured much of the attention of the scientific community. Prior to 2008, published measurements of cosmic ray electrons were only

[1]This term will refer to the sum of electrons and positrons unless explicitly stated.

[2]Measured by the balloon and space-borne experiments, as influenced by the Earth's magnetic field.

by balloon-borne experiments and one space based mission (AMS-01 [6]). Within their respective margins of error, these experiments all showed results consistent with theoretical interpretations. Subsequent measurements of cosmic ray electrons presented results that are inconsistent with predictions given by conventional propagation models. In 2008, the ATIC [7] and PBB–BETS [8] experiments published results suggesting a spectral excess bump in the range of 300 – 800 GeV. The most notable results were reported by the PAMELA mission, showing the clear increasing of the positron–electron fraction with increasing energy above 10 GeV [9]. There has been extensive debate on the origin of these features with interpretations theorizing the excess is the result of: (1) needed refinement to conventional cosmic ray propagation models, (2) the presence of an unresolved local source (e.g. supernovae and/or pulsars), or (3) new exotic physics, where dark matter annihilation and/or decay are producing electrons and positrons. These scenarios will be discussed further in the chapter to follow.

The focus of this study will be on two space-born cosmic ray experiments, the Fermi Large Area Telescope (LAT)[10], and the Calorimetric Electron Telescope (CALET) [11]. The Fermi LAT is a current orbiting observatory, launched into space in the summer of 2008, which has provided unprecedented statistics on the cosmic ray electron spectrum (here in [12, 13, 14]). CALET is a recently deployed cosmic ray mission on the International Space Station in August of this year and will provide the highest direct energy measurements of electrons to date.

Measurements on the cosmic ray electron spectrum is an extremely challenging and nontrivial task. Isolating the signals of diffuse cosmic ray electrons from the vast hadronic and gamma-ray background requires very robust and meticulous distinguishing techniques. We will present our efforts in aiding cosmic ray electron detection in support of the instruments discussed above. We concentrate on applying modern techniques in particle identification based multivariate analysis and machine

learning methods. We have extensively studied these techniques by applying them to large statistics generated from Monte Carlo simulations of the detectors and have developed analysis on the background rejection power of the instruments. Furthermore, these detectors are based on similar technology and are at various stages in their mission lifetime, this has allowed for adaptability and improvements in this analysis.

This dissertation is structures into three parts as followed: Part One will review the physics foundation for this study. In Chapter 1 we examine cosmic ray astrophysics necessary for the development or insights gained in the field of cosmic ray research and focus on the theory related to the objectives of this dissertation. In Chapter 2 we will study the relevant detector physics needed to accurately describe events traversing the instruments for particle identification. Part two will provide an overview of the two experiments we are investigating, Chapter 3 and 4 will address the Calometric Electron Telescope and the Fermi Large Are Telescope , respectively. Finally in Part three, we introduce in Chapter 5 the multivariate analysis method applied within for discriminating electrons from background events. Then, we present the the analysis of the calibration data and/or simulation data of the experiments, for CALET in Chapters 6 and Fermi LAT in Chapter 7. In the closing remarks, we will discuss the the lessons learned in the analysis and the future direction.

Part I

Physics Foundation

Chapter 1

Cosmic Rays Astrohysics

An overview of the physics governing high energy cosmic rays is presented in this chapter. In section 1.1 we review the characteristics of cosmic rays as observed by the ground and space based experiments. Section 1.2 will present the acceleration mechanisms believed to account for the enormous energy transferred to cosmic rays. We will discuss in section 1.3 the diffusion of cosmic rays in the galaxy. Lastly, section 1.4 examines the cosmic ray electron component and their possible origins in the Universe.

1.1 Composition and Spectrum of Cosmic Rays

Cosmic rays are broadly defined as all charged particles and nuclei entering the Earth's Atmosphere from interstellar space, and the term is often applied to high energy photons, neutrinos, or exotic particles. These particles are conventionally separated into two subgroups, *primaries* and *secondaries*, dependent upon their origin. Primary cosmic rays are particles and nuclei that are created and accelerated at astrophysical sources, while secondary cosmic rays are generated in interactions of the primaries with the interstellar medium (ISM). The composition of primaries are electrons, protons, helium, and heavier nuclei produced in stars. Secondaries consist

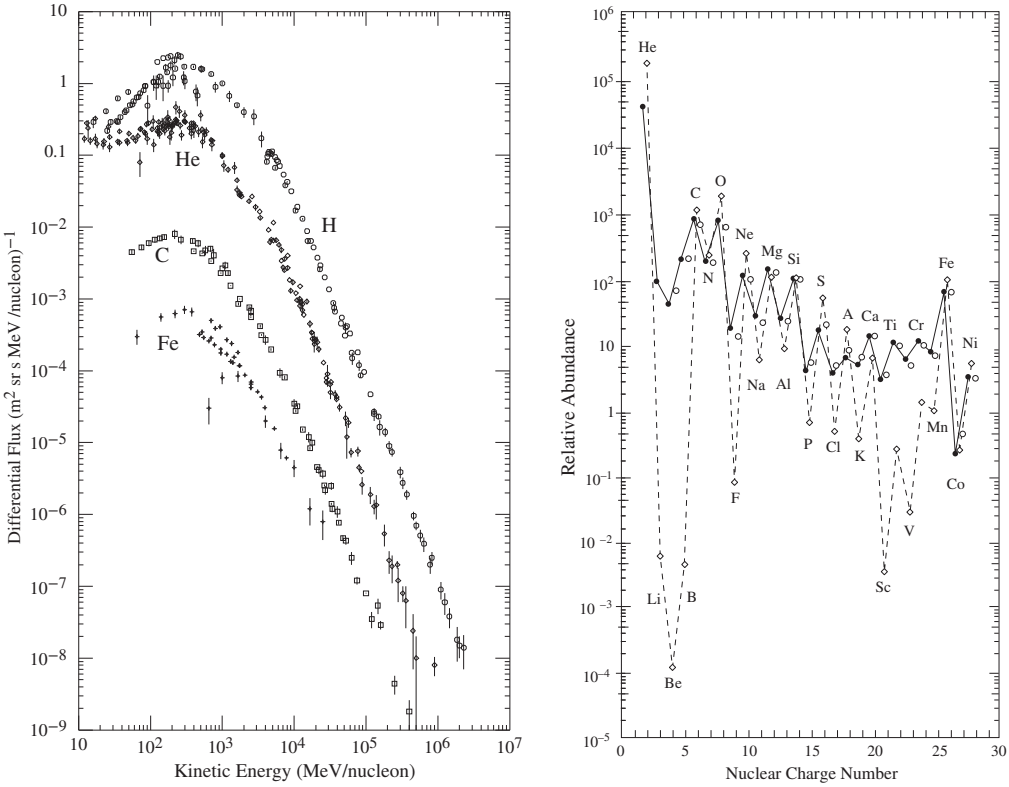

(a) (b)

Figure 1.1: (a) Fluxes of the major components of the primary cosmic radiation. (b) Relative abundances of primary cosmic ray nuclei (solid line) to solar elements (dashed line). He–Ni is normalized to Silicon. Both from [15].

of antiprotons, positrons, and nuclei that are not a resulting product of stellar nucleosynthesis such as lithium, beryllium, and boron. It should be noted that a small fraction of these antiprotons and positrons have been suggested to be a component of primary cosmic rays, which is of current interest and will be discussed in a later section (1.4).

The distribution of the components of cosmic rays are approximately 98% nuclei and approximately 2% electrons, antiprotons, and positrons. Summing over all energies, primary nucleons are about 87% fully ionized hydrogen (or free protons), and

about 12% of nucleons constitute helium nuclei, with remaining 1% forming heavier elements [15]. Above 10^{12} GeV to about 10^{15} GeV, the composition of nuclei may become more enriched in heavy nuclei [16]. The fluxes and differential spectra of the major components of the primary cosmic ray ($Z > 1$) are shown in Figure 1.1. The similarities suggests a universal mechanism is controlling these spectra. Recent research suggests slight differences in the spectral slopes [17], which will provide information on the details of the acceleration mechanism. As shown in Figure 1.1b, the chemical composition of primary cosmic nuclei exhibit close similarities to the solar elemental abundances, with some significant differences that beg explanation. Both abundances display the odd-even effect of stability, where the more strongly bounded even atomic number(Z) and even mass number (A) nuclei are more abundant than the odd A and/or Z nuclei. This is direct result of thermonuclear reactions in stars, where even–even (even Z and even A) nuclei are more frequently a product of nucleosynthesis. The similarities in the peaks of C, N, O, and Fe abundances suggest the many of the cosmic ray nuclei may be from stellar origin. The substantial difference between Li, Be, and B relative abundances are attributed to *spallation* of cosmic ray C and O nuclei as they traverse the interstellar medium. The same effect can be seen with the abundances of Sc, Ti, and Mn due to spallation of Fe and Ni nuclei.

The *all–particle* primary cosmic ray spectrum is shown in figure 1.2, nearly extending 11 orders of magnitude in energy and over almost 30 magnitudes in flux. The differential energy spectrum appears roughly featureless. However, there are two transition points that may indicate different origins of the cosmic rays in the different energy ranges. The first transition point occurs at $\sim 3 \times 10^6$ GeV, this feature is the so-called the *knee*. The knee is presumably a consequence of the upper limits of the acceleration mechanism of some sources and understanding the knee is believed to be the key in understanding of the origin of galactic cosmic rays. This feature

is commonly attributed to either the breakdown of the mechanism by which cosmic rays are trapped in our galaxy [18], or to the maximum energy to which supernova remnants are able to accelerate charge particles to [19]. The second transition point, the so-called *ankle*, is located at $\sim 4 \times 10^9$ GeV and the nature of this feature is still debatable; the common assumption is an onset of penetrating extra-galactic cosmic rays with a harder spectrum.

A theoretical upper limit on the energy of cosmic rays, with an energy of 5×10^{19} eV, is referred to as the Greisen–Zatsepin–Kuzmin (GZK) limit [20, 21]. Cosmic rays originating in extragalactic sources would interact with the cosmic microwave background photons, producing a pion cascade and $cut - off$ the spectrum.

$$p + \gamma_{cmb} \rightarrow p + \pi^0 \qquad , \qquad p + \gamma_{cmb} \rightarrow n + \pi^+ \tag{1.1.1}$$

Ground based cosmic ray experiments have observed a suppression in the energy spectrum at the highest energies that are consistent with the GZK limit [22, 23] but several fundamental questions still remain.

These transition points established several energy regions in the cosmic ray spectrum, each following a simple power law:

$$\frac{dN}{dE}(E) = k \cdot E^{-\gamma}. \tag{1.1.2}$$

where $N(E)$ is the number of particles between E and $E+\Delta E$, k is the normalization constant, and γ is the spectral index of the cosmic ray flux (i.e. slope). The spectral index above a few GeV is ~ -2.7 for energies up to the knee. The spectrum falls off rapidly following the knee to the ankle, with a spectral index of ~ -3.0 and then hardens to an index of ~ -2.69 until reaching the GZK cutoff. As one can

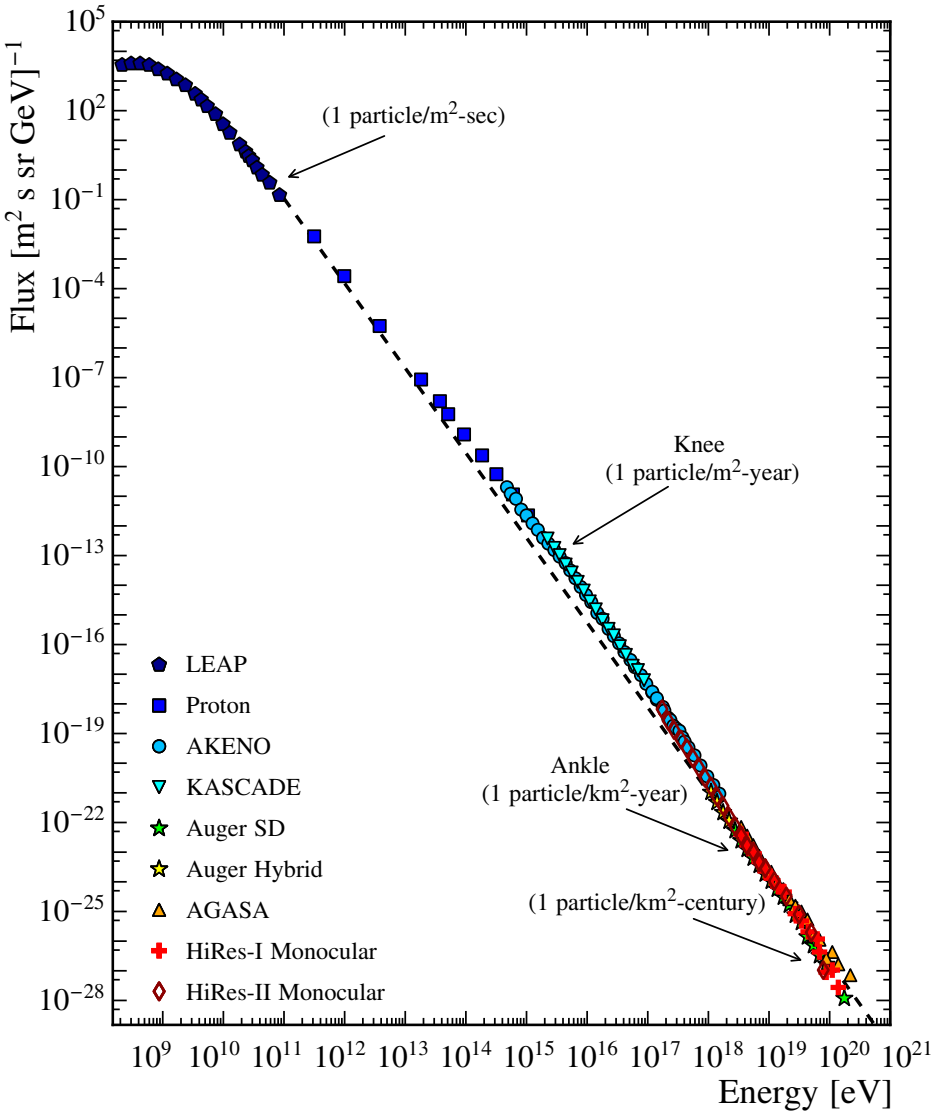

Figure 1.2: Differential cosmic ray flux as observed above 100 MeV [24, 25, 26, 27, 28, 29]. The *dashed* line represents an spectrum of $E^{-2.86}$.

see in Figure 1.2, as the energy increases, the corresponding cosmic rays become increasingly rare. At energies above 10 GeV, the influence of the magnetic field of the Earth and Sun become negligible and the cosmic radiation exhibits isotropic

behavior [30]. One should note, solar modulation will only be moderately discussed in this study since we concern ourselves with highly energetic cosmic rays.

1.2 Cosmic Ray Acceleration

The understanding of acceleration mechanisms responsible for the extensive energy range of cosmic rays remains an open question today and establishment of their origin present many challenges. Models of how high energy cosmic rays are created may be distinguished into two classes: the so-called "top-down" and "bottom-up" scenarios. In the former, cosmic rays are created at such high energies as a product of the decay or annihilation of extremely massive relic particles [31], thus no acceleration is necessary. The latter scenario, conventional matter is accelerated to high energies in specific astrophysical environments and does not require new physics to address their existence. The bottom-up scenario is examined here, and we restrict ourselves to the standard acceleration mechanisms of cosmic rays while discussing the underlying processes in this section.

Several decades following the discovery of cosmic radiation, various sources were proposed but their respective acceleration processes were absent from the literature. The first mechanism for cosmic ray acceleration was postulated by Enrico Fermi in 1949 [32], demonstrating charged particles could be accelerated to high energies through collisions with magnetic inhomogeneities in the interstellar medium (see Fig. 1.3). Assuming these clouds have random velocities, Fermi argued that the inherent magnetic fields would act as reflectors and transfer energy to the particles with an average gain of:

$$\left\langle \frac{\Delta E}{E} \right\rangle \propto \left(\frac{u}{c} \right)^2 \tag{1.2.1}$$

where u is the velocity of the gas cloud and the particle's velocity is $v \sim c$ (for

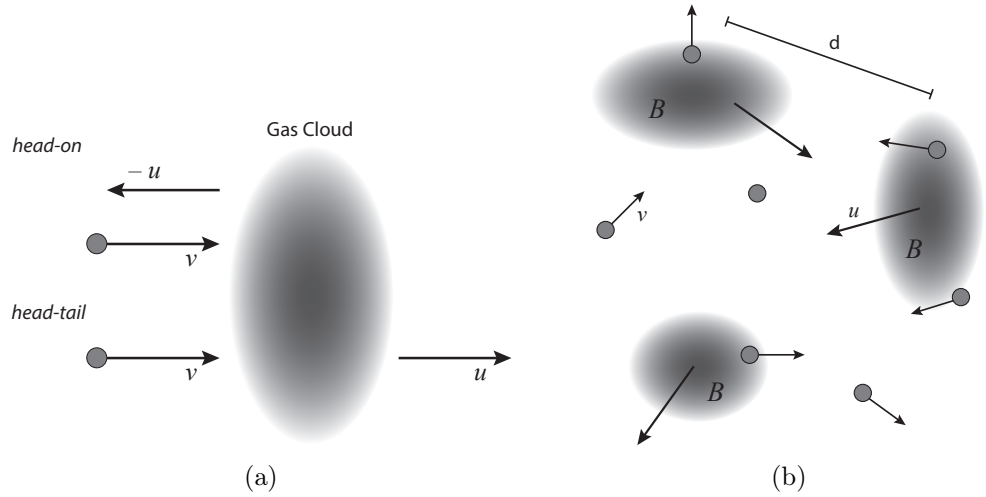

Figure 1.3: Schematic representation of 2*nd* order Fermi acceleration. (a) Energy gain from head-on collision and loss from head-tail collision, Probability(head-on) > Probability(head-tail). (b) Interstellar clouds move randomly and particles are accelerated from collisions.

detailed calculation, refer to [33]). This process is known today as the *second order Fermi acceleration* shown by the quadratic nature of the energy increase. In consideration of $u \ll v$ and the large mean free path between clouds (d), the rate energy gain per collision of this stochastic mechanism is on the order of $\sim u^2/d$, very moderate and ineffiecient. A required minimum injection energy would be necessary to balance the energy loss of the particles through interactions in the ambient medium and achieve the observed energies presented in Figure 1.2.

In the late 1970s, several scientists [34, 35, 36] independently expanded upon the ideas of Fermi and introduced what is considered the leading acceleration mechanism of cosmic rays, known as *diffusive shock acceleration*. The thought is that particles could gain energy more efficiently and effectively in collisions when the macroscopic motion is relatively high and coherent, as found in strong shock waves produced by *supernovae explosions* where velocities are much greater than gas clouds in the interstellar medium. As illustrated in Figure 1.4, relativistic particles diffusing the

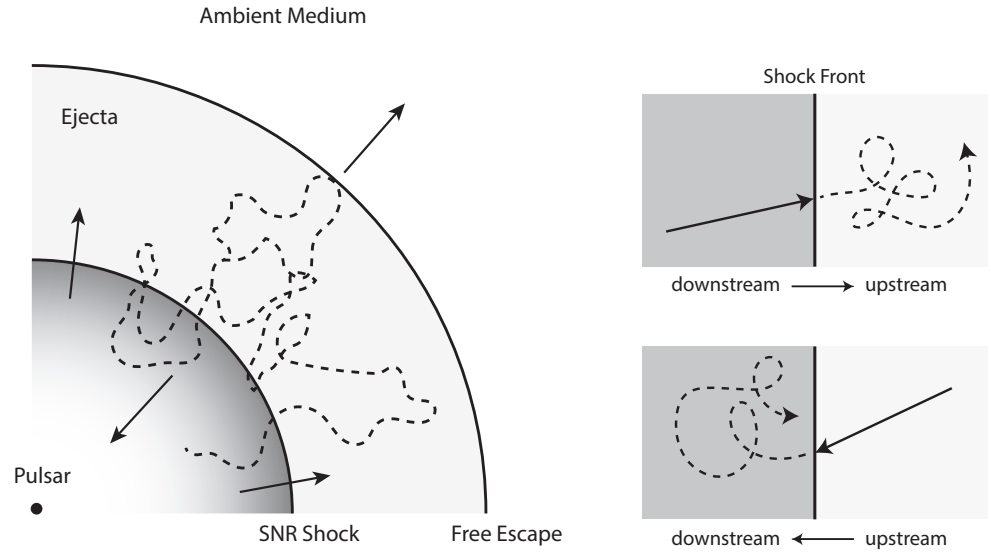

Figure 1.4: Schematic representation of 1*st* order Fermi acceleration. (a) Supernova diagram: Particle traverse shock front, gaining energy before escaping. (b) Particle motion in the rest frame of the shock: head-on collisions in the both downstream $\rightarrow$ upstream and upstream $\leftarrow$ downstream.

shock front from downstream to the upstream region and vice versa will engage in head-on collisions in the both directions. The average gain in energy can be shown [33] in one roundtrip to be:

$$\left\langle \frac{\Delta E}{E} \right\rangle \propto \left(\frac{u}{c} \right), \tag{1.2.2}$$

where u is the velocity of the gas behind the shock. This process is commonly referred to as *first order Fermi acceleration* and has shown diverse application.

Equation 1.2.2 leads to a very significant result for high energy particles, the power law differential energy spectrum derived from first order Fermi accelerations is [33]:

$$N(E)dE \propto E^{-2}dE. \tag{1.2.3}$$

The observed spectral index of 2.7 (as previously mentioned) is not achieved here,

however, equation 1.2.3 does provide encouraging results and the disagreement can be attributed to cosmic ray propagation mechanisms. One possible explanation is that the escape probability of cosmic rays from the galaxy increases with energy and may affect the overall observed spectral index. One should also note, more detailed theories produce slightly larger indices for equation 1.2.3, up to ~ 2.2, further validating this acceleration mechanism. The maximum particle escape energy achievable by supernova shock acceleration has been shown to be as large as $E_{max} \sim Z \times 10^6$ GeV, accounting for cosmic rays up to the knee [37, 38]. The presence of strong shock waves are expected to be not only in supernovae remnants but in various astrophysical environments throughout the universe.

1.3 Cosmic Ray Propogation

Understanding the dynamics of cosmic rays is essential to interpretations of many high energy astrophysics phenomena. Once these energetic particles are injected into the galactic environment, they must propagate through the interstellar medium before our detection. In Figure 1.5, a schematic top and side view of the luminous matter in Milky Way is shown to illustrate the complexity of the structure and extent of our galaxy. During their lifetimes, GeV cosmic rays are estimated to traverse 5-10 g/cm^2 equivalent hydrogen between injection and detection, resulting in distances up to thousands of times greater than the thickness of our galactic disk (10^{-3} g/cm^2)[39]. The particles are subject to a number of processes during the propagation stage, altering their initial injection energy through interactions with matter, magnetic fields, and radiation. Diffusion, convection, and reacceleration processes contribute in the observe characteristics of cosmic rays.

The transport of high energy cosmic rays through the interstellar medium may be sufficiently expressed for the treatment of propagation and acceleration by the

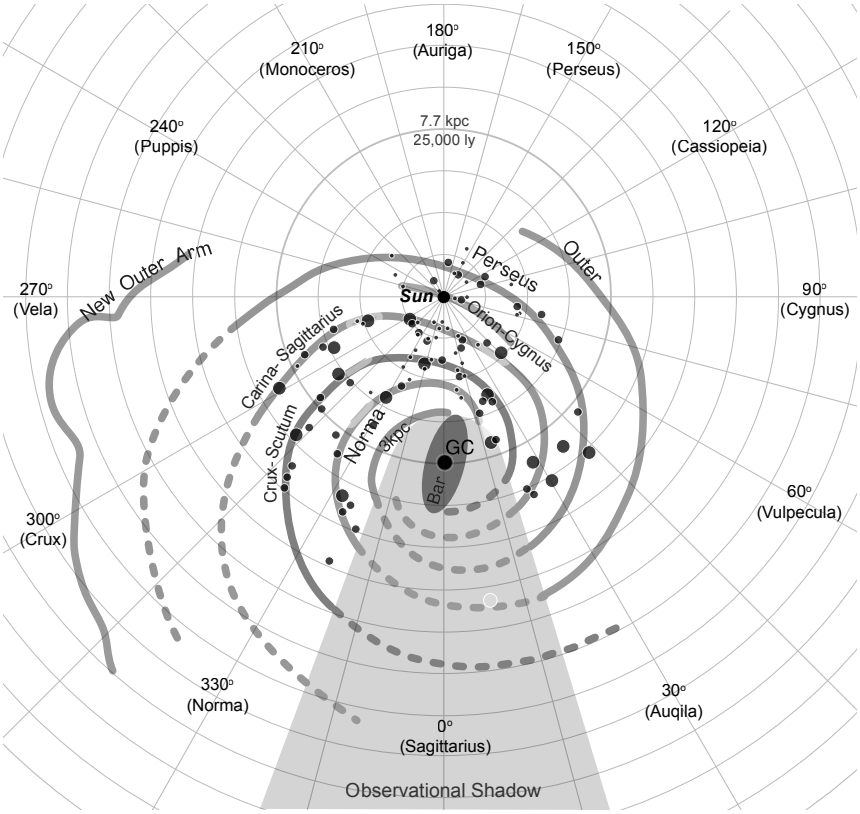

(a) Top schematic view of the Milky Way galaxy with observed and extrapolated structure in galactic coordinates.

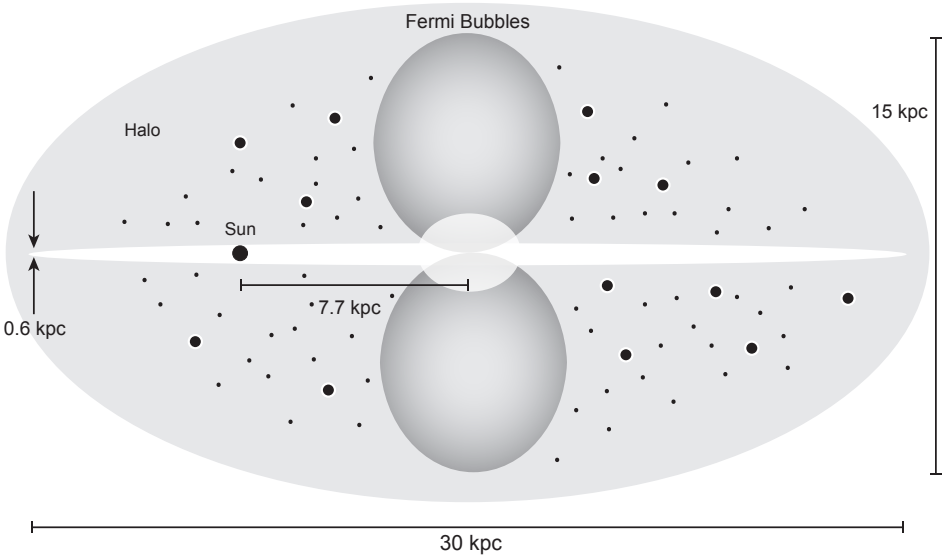

(b) Side schematic view of the Milky Way galaxy with gamma-ray bubbles extending above and below the galactic center, known as *Fermi Bubbles*[40].

Figure 1.5: Schematic of the Milky Way Galaxy: Top and Side View

diffusion–loss equation [33]:

$$\frac{\partial \mathcal{N}_i}{\partial t} = \nabla \cdot (D_i \nabla \mathcal{N}_i) + \frac{\partial}{\partial E}[b_i(E)\mathcal{N}_i(E)] + Q_i(E,t) - \frac{\mathcal{N}_i(E)}{\tau_i} + \sum_{j>i} \frac{P_{ji}}{\tau_j}\mathcal{N}_j(E') \quad (1.3.1)$$

where $\mathcal{N}_i(E, \mathbf{x}, t)dE$ is the number density of particles of type i between E and $E + dE$. The first term, $\nabla \cdot (D_i \nabla \mathcal{N}_i)$, describes the spatial diffusion process of particles where D is the diffusion coefficient proportional to the velocity of the particle and the diffusion mean free path ($\propto v\lambda_d$) [39]. The diffusion coefficient is commonly estimated by measuring the ratio of secondary-to-primary cosmic rays. Normal values for the diffusion coefficient are D $(3-5) \times 10^{28}$ cm^2/s at an energy of 1 GeV/nucleon, and increases with magnetic rigidity (R). Different scattering processes give $\mathrm{R}^{0.33}$ to $\mathrm{R}^{0.5}$, depending on the details of the physical scattering processes. The evolution of the particle energy spectrum is represented by the following term, $\partial[b_i(E)\mathcal{N}_i(E)]/\partial E$, subject only to continuous energy gains and losses, where $b_i(E) \equiv dE/dt$. The injection rate of particles per unit volume is represented by the source term $Q_i(E,t)$.

The two subsequent terms relate to the effects of spallation to species i losses and gains from heavier species $j > i$, respectively. Particle species lifetimes are characterized by τ_i and τ_j, where P_{ji} is the probability of the of producing species i from spallation of particle type j [33]. The last term may also be used to estimate the lifetime of cosmic rays by examining the ratio of *cosmic clocks* or radioactive isotopes (e.g. ^{10}Be/^{7}Be). Under steady-state conditions, the estimated average lifetime of cosmic rays can be shown to be $\sim 10^7$ years [41], which is very long compared to the light crossing time of the galaxy.

Equation 1.3.1 may be extended to include other processes influencing cosmic rays as these high energy particles propagate through the galaxy. The following two terms are often appended to the diffusion–loss equation equation:

$$\frac{1}{2}\frac{\partial^2}{\partial E^2}[d(E)N(E)] \qquad \text{and} \qquad \nabla \cdot \mathbf{u}\mathcal{N}_i,$$

in order to account for stochastic *reacceleration* of the particle through random collisions where $d(E)$ is the mean square energy change per unit time (as describe in[42]), and convection from galactic winds of velocity $\mathbf{u}$, respectively.

1.4 Cosmic Ray Electrons + Positrons

Cosmic ray electrons (CREs) are a very small component of the overall cosmic ray composition ($\sim 1\%$), nevertheless, may provide invaluable information on astrophysical processes within the galaxy. The origin of CREs are predominately *primary* in nature, produced and accelerated in astrophysical sources such as supernovae. *Secondary* CREs are generated from hadronic interactions in the interstellar medium, such as

$$p + H \rightarrow \pi^0 X, \;\; \pi^0 \rightarrow 2\gamma, \;\; \gamma \rightarrow e^+ + e^-, \tag{1.4.1}$$

$$p + H \rightarrow \pi^{\pm} X, \;\; \pi^{\pm} \rightarrow \mu^{\pm}\nu_e(\bar{\nu_e}), \;\; \mu^{\pm} \rightarrow e^{\pm}\nu_e(\bar{\nu_e})\nu_\nu(\bar{\nu_\nu}), \tag{1.4.2}$$

where X is all by-products of the interaction process. Proton-proton interactions will dominate this mechanism, though spallation of heavier cosmic ray nuclei (e.g. p+He, α+H, etc.) in the ISM will also produce secondary electrons through hadronic cascades. Energetic electrons may have other origins and will be discussed further in this section.

1.4.1 Properties

CREs are subject to a number of electromagnetic energy loss mechanisms throughout their lifetime due to the small mass ($m_e = 0.511$ MeV/c^2), in addition to collisions losses other charged particles experience (see [43] for detailed review). At high energies ($E > 10$ GeV), energy losses of CREs are dominated by: *synchrotron radiation* emitted while traversing cosmic magnetic fields; and *inverse Compton scattering* while moving through radiation fields (i.e. optical, infrared, and CMB radiation). Synchrotron radiation may limit the maximum injection energy of an electron, as in the case of acceleration in the supernova shock discussed in section 1.2. The maximum energy achievable with synchrotron energy loss can be expressed as [39]:

$$E_{max}^{synch} = 2.3 \times 10^4 \ \text{GeV} \ \frac{u}{c} \cdot \frac{B^{-1/2}}{G}, \tag{1.4.3}$$

where u is the shock velocity and B is the magnetic field within. Thus, using fiducial values of $u = 10^9$ cm/s and $B = 5$ μG, a maximum injection electron energy with energy loss is $E_{max}^{synch} \approx 340$ TeV. The magnetic field within the shock front is assumed to be relatively small, nonetheless, the maximum energy may be severely limited in the presence high magnetic fields as with neutron stars interacting with the neighboring matter.

Since cosmic ray electrons do not undergo the same processes as charged nuclei, the diffusion–loss equation (eq. 1.3.1) reduces to the the form of:

$$\frac{dN(E)}{dt} = \nabla \cdot (D \nabla N(E)) + \frac{d}{dE}[b(E)N(E)] + Q(E,t). \tag{1.4.4}$$

The energy loss term can be expressed in terms of synchrotron radiation and inverse

Compton scattering at high energies [33]:

$$b(E) = -\frac{dE}{dt} = b_0 E^2, \qquad \text{where} \qquad b_0 = \frac{4\sigma_T c}{3(m_e c^2)^2}\left(w_{mag} + w_{rad}\right). \tag{1.4.5}$$

The Thomson cross section is denoted as σ_T, with the energy density of the magnetic field and radiation field represented by w_{mag} and w_{rad}, respectively. Typical values for the galactic magnetic energy density is $w_{mag} = 0.2$ eV/cm^3 ($B = 5\mu$G) and the average energy density of interstellar photons within the galactic disk is $w_{rad} = 0.6$ eV/cm^3. Using the previous values, the lifetime of high energy CREs in the galaxy may be estimated from the energy loss rate:

$$\tau_{e^\pm}(E) = \frac{E}{dE/dt} = \frac{1}{b_0 E}. \tag{1.4.6}$$

Therefore, 100 GeV electrons will have a lifetime of $\tau_{e^\pm} \sim 10^6$ yrs and 1 TeV electrons are limited to a lifetime of $\tau_{e^\pm} \sim 10^5$ yrs. These lifetimes restrict the distances of which we may observe high energy electron sources, limiting to several hundred parsecs for TeV sources up to a two kiloparsecs for GeV sources [44]. This may provide advantages to other cosmic ray species, allowing us to effectively probe the nearby galactic space.

The strong energy loss dependence ($b(E) \propto E^2$) of electrons additionally produces a solution to equation 1.4.4 of

$$N(E) \propto E^{-(p+1)}, \tag{1.4.7}$$

where $p+1$ is the primary spectral index. If we use the injection index from second order Fermi acceleration in equation 1.2.3, the observational flux would have an upper limit of hardness as $N(E) \propto E^{-3}$ at energies above 10 GeV. Comparatively,

the electron flux falls off more rapidly than that of protons with an spectral index of $\sim$ 2.7 within the same energy range (seen in sect. 1.1), as a result of considerable energy loss during propagation. While cosmic rays is considered to be nearly isotropic at most energies owing to propagation in the galactic magnetic field, we would expect to observe some anisotropy in the arrival directions, considering sources for high energy electrons are limited to the local space where only a small number exist [45].

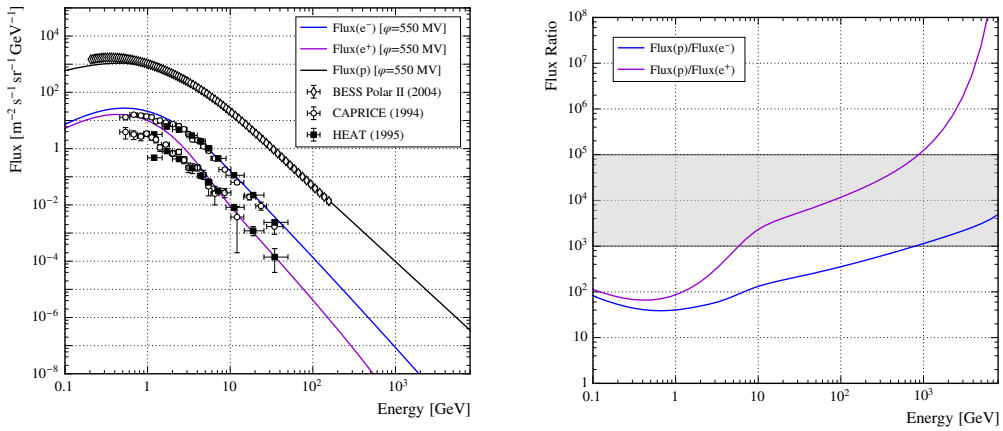

(a) (b)

Figure 1.6: (a) Cosmic ray electrons and positrons fluxes from balloon flights results of CAPRICE94 [46] and HEAT [47],and protons from BESS Polar II [17]. Solid lines are standard `GALPROP` propagation models for protons (black line) [48] and electrons/positrons (blue/purple line) [49]. (b) Ratio of electron/positron to proton fluxes, shaded region is the range of current experiments rejection factors.

As previously stated, cosmic ray electrons and positrons contribute only a small fraction to the overall cosmic ray spectrum, overshadowed by the vast proton background. In Figure 1.6a, the low intensity of electron + positron signals can be seen in contrast to the proton flux employing theoretical calculations based on conventional diffusion models from the `GALPROP` propagation package [50], with results from notable balloon-borne experiments. In order to efficiently detect $e^{\pm}$ at high energies, a large proton rejection factor greater than 10^3 is necessary, as exhibited in Figure 1.6.

This is an increasingly difficult task as the energy increases, and interacting protons may mimic the behavior of an electron or positron (see further discussion in Chapter 2).

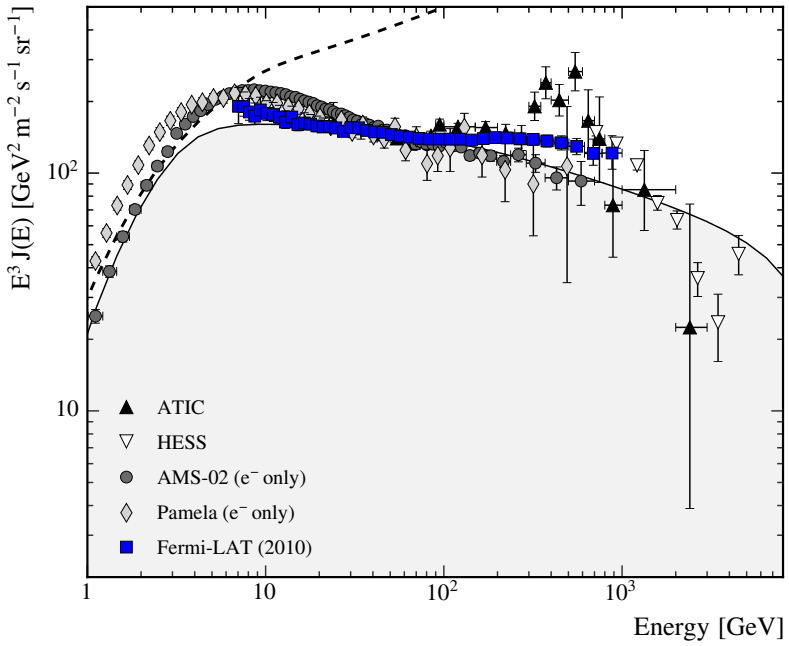

Figure 1.7: Differential spectrum of electrons plus positrons (except PAMELA and AMS) $\times$ E^3 [7, 51, 52, 53, 12]. Dashed black line shows the proton spectrum [48] multiplied by 0.01. Solid line is conventional diffusive propagation model for e^- + e^+ [49].

1.4.2 Current Spectrum

Modern era experiments have ushered in a new phase in the study of cosmic ray electron and positrons, inclusively and independently, with high precision measurements. The CRE spectrum is shown in Figure 1.7, measurements from three satellites PAMELA [53], Fermi-LAT [12], and most recently AMS-02 [52]; with the ground-based array HESS (*indirect* measurements) [51], and the balloon-borne instrument ATIC [7]. The differential flux is multiplied by E^3 to accentuate spectral

shapes. The ATIC experiment first reported a strong spectral feature in excess of the standard diffusion model [49] at energies between 300 and 800 GeV. The HESS telescope array indirectly measured electron air showers from 340 GeV, confirming the excess in the spectrum but not the pronounced peak as indicted by ATIC. The Fermi LAT observatory also measured with high statistics an excess in the electron spectrum without evidence of a peak, but did display spectral hardening above approximately 100 GeV and slight softening starting at around 500 GeV.

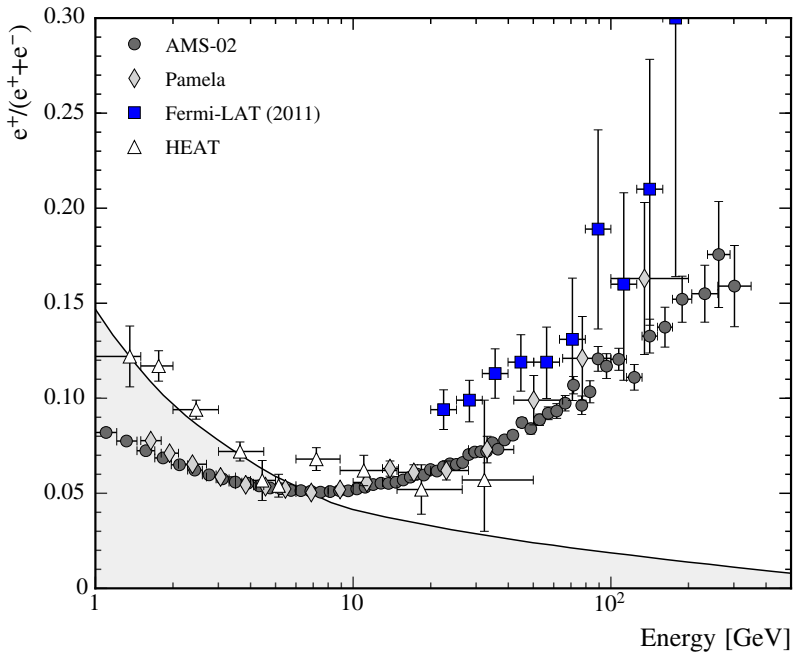

Figure 1.8: The positron fraction (ratio of the e^+ flux to the combined $e^- + e^+$ flux) [47, 52, 54, 14]. Solid black line is a model for pure secondary positron production [49].

The positron fraction in the electron flux ($e^+/(e^-{+}e^+)$) is shown in Figure 1.8. PAMELA measured the first rise in the positron fraction above 10 GeV to 100 GeV [9], deviating from the expected decrease of positrons with exclusively secondary [49]. This confirmed earlier hints from the HEAT balloon-borne experiment [47], which showed a slight increase in the positron fraction, but measurements contained large

uncertainties up to 30 GeV. The Fermi LAT also reported a rise in the positron fraction from 20 GeV to 200 GeV exploiting the *east-west effect* of the Earth's magnetic field to measure the individual components [14]. AMS-02 recently provided high precision results up to 500 GeV that were also consistent with a rise in the positron fraction [52].

1.4.3 Observational Interpretation

The inconsistencies in the CRE spectrum shown in Figure 1.7 and positron fraction Figure 1.7 below 10 GeV may be easily explained by solar modulation during the time of measurement. However, the excess in the total flux of electrons and the increase in the positron fraction beyond standard assumptions suggest an additional source(s) of electrons and positrons may be present. Possible explanations of these anomalies are generally separated into the following three categories ([55] and Refs. therein):

Astrophysical Origins: Local Supernova Remnants and Pulsars

Artifacts of supernova explosions, Pulsars and Supernova Remnants (SNRs), are uncontested sources of highly energetic electrons. It has been long discussed that nearby pulsars and SNRs could determine fundamental characteristics of the electron spectrum at high energies. Pulsars are believed to be powerful factories of electron-positron pairs in the magnetosphere, and subsequently reaccelerated by the pulsar winds or the SNR shocks before merging with the ISM. SNRs have also been suggested to not only accelerate electrons but positrons as well in the shock fronts. Others have argued that positrons may be additionally produced in beta-decay in the explosion, as well as, in the reverse shock of the supernova. There have been many discussions on this topic and an astrophysical origin of the electron-positron anomalies continues to be leading theory.

Exotic Origin: Dark Matter Annihilation and/or Decay

Weakly Interacting Massive Particles (WIMPs) are considered to be the most attractive candidate for Dark Matter (DM). Widely discussed in the literature, DM in galactic halo and subhalos may supplement the cosmic ray electron and positron spectrum by: (1) majorana (i.e. a particle that is its own antiparticle) WIMP annihilation $\chi\chi \rightarrow \cdots \rightarrow e^+e^-$, where multiple channels could result in leptonic final states; (2) WIMP decay $\chi^* \rightarrow \cdots \rightarrow \chi e^+e^-$, producing a electron-positron pair. If the excess in the total electron flux and positron fraction is attributed to DM, the preferred mass of the dark matter particles lies between 400 GeV and 2 TeV, which would produced strong spectral features in the energy range of interest. One should note, there is no physical evidence of this mechanism and, as of today, it is highly theoretical.

Secondary Production: Interactions with Interstellar Medium

Conservative explanations attempt to preserve conventional diffusive models with cosmic ray positrons are purely secondary. The addition of nearby sources are able to account for features in the total electron flux measurements, however, not the anomaly in the positron fraction. Some have suggested that large scale inhomogeneities in the distribution of sources may account for these deviations but provide insufficient conclusions. However, it is clear that if propagation effects are in fact the culprit, one needs to consider unconventional positron sources.

Chapter 2

Principles of Detector Physics

The area of particle detector physics is an extensive field that is continually evolving with the emergence of new technologies and more complex constructions, improving efforts in studying the most elementary aspects of nature. In this chapter, we will restrict ourselves to the fundamental detector physics relevant to this body of work. Section 2.1 will introduce the basic design of an *astroparticle* detector and the underlying functions of each subsystem. In sections 2.2 through 2.4, the fundamental physics related to electromagnetic particle interactions will be reviewed. Finally, section 2.5 will discuss how hadronic particles may contaminate the electron signal.

2.1 Particle Astrophysics Detectors

High-energy gamma ray telescopes, with which we are concerned here, are commonly referred to as *pair-conversion* telescopes. To study high energy gamma rays, they are required to detect high energy photons in space while filtering out the cosmic ray background. The pair-conversion designation arises from the fact that incident gamma-ray photons, with energy greater than twice the electron rest mass ($E_\gamma > 2 \times 0.511$ MeV), can convert to electron-positron pairs while traversing the dense material in the detectors [56]. The basic overall structure of a pair-conversion

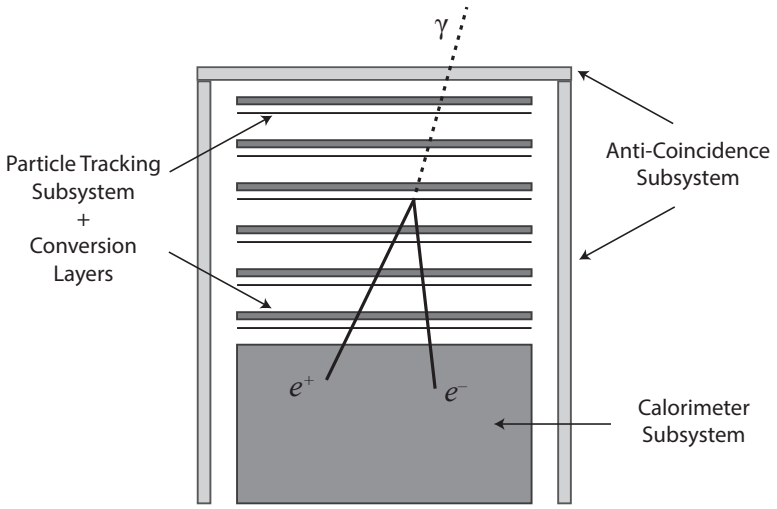

Figure 2.1: Simple Pair-Conversion Telescope Schematic.

telescope is shown in Figure 2.1, consisting of three main detector subsystems:

Anti-coincidence Detector

Measures the charge of incident particle to screen out the cosmic ray particle background, commonly with plastic scintillator detectors for fast response and sensitivity to large energy range. To operate successfully at high energy, this subsystem must be highly segmented to reduce the occurrence of *self-veto* from backsplash of particle showers.

Tracking Detector

Measures the particle(s) trajectory to reconstruct arrival direction while initiating pair-conversion. The construction of this subsystem is generally alternating layers of highly granulated active material to measure the position of a traversing charged particle and high-Z material (e.g. tungsten or lead) to induce particle cascades.

Calorimeter Detector

Measures the total energy of the incident particle(s) with fully active hodoscope

structure of homogeneous material. For total absorption of electromagnetic particles, calorimeters are frequently constructed of inorganic crystals (e.g. cesium iodide or lead tungstate), dense and fast scintillating material.

In principle, pair-conversion telescopes were developed to observe high energy gamma-rays, however, have demonstrated great success in measuring the cosmic ray electron spectrum using their electromagnetic cascade properties. Since this type of detector is not able to inherently distinguished charge of same mass particles, electromagnetic calorimetric techniques for each subsystem will be discussed below.

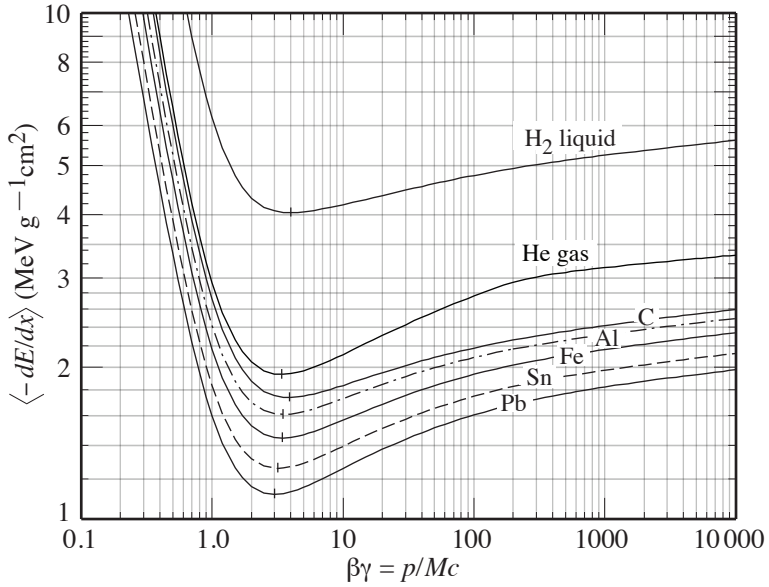

Figure 2.2: Mean energy loss rate in different mediums. Taken from [57].

2.2 Anti-Coincidence Detector

A relativistic charged particle traversing a medium will lose energy through interactions with target electrons, primary due to excitation or ionization of atoms in the detector. The signal produced in the anti-coincidence detector from scintillating photons is proportional to the ionization energy loss of the incident charged particle,

and can be well described by the *Bethe-Bloch formula* for heavy particles [57]:

$$-\left\langle \frac{dE}{dx} \right\rangle = Kz^2 \frac{Z}{A} \frac{1}{\beta^2} \left[\frac{1}{2} \ln \frac{2m_e c^2 \beta^2 \gamma^2 T_{max}}{I^2} - \beta^2 - \frac{\delta(\beta\gamma)}{2} \right]. \tag{2.2.1}$$

Where

K	: $4\pi N_A r_e^2 m_e c^2$	δ	: Density correction
z	: Charge of incident particle	N_A	: Avogardo's Number = 6.022×10^{23}
M	: Mass of incident particle	r_e	: Classical electron radius
Z	: Charge number of medium	m_e	: Electron mass = 511 keV)
A	: Atomic mass of medium	β	: Velocity = v/c
I	: Mean excitation energy of medium	γ	: Lorentz factor = $1/(1\text{-}\beta^2)^2$.

The maximum energy transferred during a single collision of an incident particle of mass M is

$$T_{max} = \frac{2m_e c^2 \beta^2 \gamma^2}{1 + 2\gamma \frac{m_e}{M} + \left(\frac{m_e}{M}\right)^2}. \tag{2.2.2}$$

In Figure 2.2, the mean energy loss is shown for various mediums as a function of incident particle momentum. At low energies, dE/dx falls off by $1/\beta^2$ with momentum until reaching the minimum, where particles near this point are characterized as *minimum ionizing particles* (MIPs). These MIPs play a crucial role in the calibration of the instruments *in situ*. At high energies ($\beta\gamma > 50$, i.e. energetic cosmic rays), the ionization energy loss becomes nearly energy independent and only depends the charge of the particle.

The *Bethe-Bloch formula* for electrons, accounting for incident and target electrons having the same mass, is [58]:

$$-\left\langle \frac{dE}{dx} \right\rangle_{e^\pm} = K \frac{Z}{A} \frac{1}{\beta^2} \left[\ln \frac{m_e c^2 \beta^2 \gamma^2 T}{2I^2} + F(\gamma)^\pm \right], \tag{2.2.3}$$

where $T_{max} = T/2$, and $F(\gamma)^{\pm}$ is the moments of the *Møller* and *Bhabha* scattering cross section for electrons and positrons, respectively. The basic foundation of the anti-coincidence detectors to identify incident charged cosmic rays on the telescope via $dE/dx \propto z^2$, however, can additionally provide measurements used to distinguish electrons from hadrons.

2.3 Tracking Detectors

As tracking detectors are essentially thin sampling calorimeters, we can also study a particle's *preshower* through lateral distribution of secondary particles generated in the cascade throughout the tracking layers with high precision. In addition to ionization energy loss, electrons interacting with matter are subject to radiative loss known as, *bremsstrahlung*:

$$-\left(\frac{dE}{dx}\right)_{Total} = \left(\frac{dE}{dx}\right)_{Ion} + \left(\frac{dE}{dx}\right)_{Brems}, \tag{2.3.1}$$

where

$$\left(\frac{dE}{dx}\right)_{Brems} = -\frac{E}{X_0}. \tag{2.3.2}$$

Energy is carried away by emitted photons scattering in the electric field of target nuclei [59] at a rate governed by the radiation length, X_0, a characteristic amount of matter for which the energy of the incident electron is reduced by $1/e$ ($\sim 37\%$). Above the *critical* energy ($E_c \sim$ few MeV), where the ionization energy loss rate equals that of radiative energy loss in the medium, the bremsstrahlung process dominates and initiates an electromagnetic particle shower. The emitted photons can subsequently produce an electron-positron pair, and this process will continue reiteratively, increasing the number of secondary particles around the track of the incident electron.

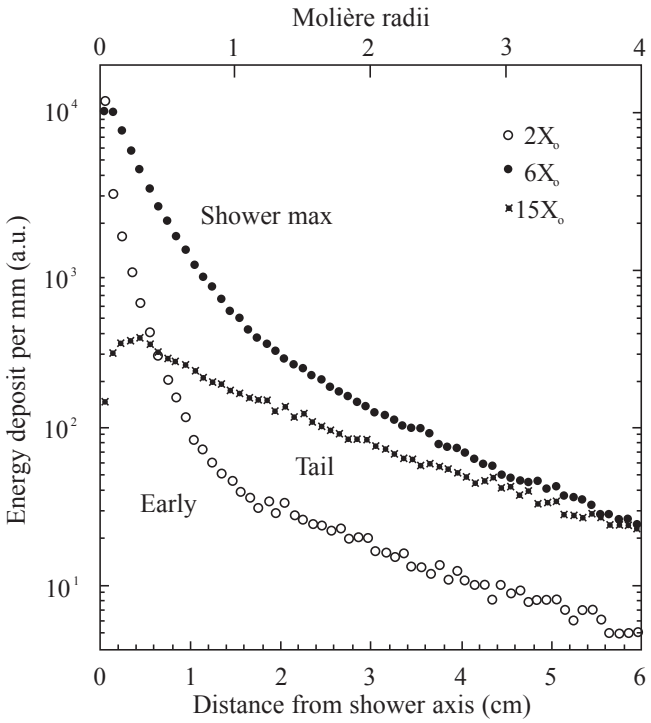

Figure 2.3: The radial distributions of the energy deposited by an incident 10 GeV electron showers on copper at various depths of X_0 (EGS4 calculation). Taken from [60].

The transverse development of electron showers are described by a material constant, known as the *Molière radius* [57]:

$$R_M = \frac{21MeV}{E_c} X_0. \tag{2.3.3}$$

In a fully contained shower, an average of 90% of the shower's energy is deposited cylindrically around the shower axis (i.e. particle track) at one R_M and 95% at two R_M. Shown in Figure 2.3, is the lateral spread of an electron shower at various depths of X_0, where *early* distribution represents the *preshower* and exhibits a more narrow distribution of deposited energy with radii considering the shower is still de-

veloping. The inner core of the shower is a result of multiple scattering of particles, and the outer core is due to low energy photons, broadening the radial distribution. The longitudinal development of preshower, especially the starting point, is also of importance given equation 2.3.2. At a particular depth, approximately one X_0, one would expect the shower to begin.

One should also note, high energy particle interacting the material in the tracking detector may effectively knock-out orbiting electrons, producing free electrons with substantial energy that could create their own tracks far from the parent particle trajectory and showers. These electrons are known as δ–$rays$, or $knock$–on electrons.

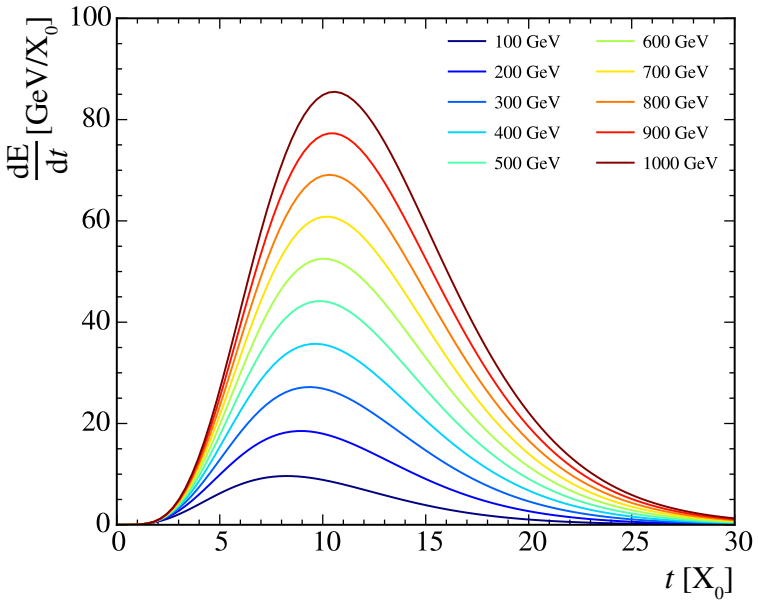

Figure 2.4: Longitudinal profile of an electron shower at various incident energies in lead tungstate ($PbWO_4$) using equation 2.4.1.

2.4 Calorimeters

The particle shower initiated in the tracking detector will continue to produce secondaries at a multiplicative rate in the homogenous calorimeter until secondaries

fall below the critical energy (E_c). The maximum point in the shower (i.e. *shower maximum*) is characterized by the maximum energy deposition and maximum number of particles produced in the cascade. Beyond that depth, the shower experiences a slow exponential decay as a result of electrons dissipating their energy through ionization and excitation rather then secondary creation; and photon attenuation is predominantly responsible for the energy loss [57].

The longitudinal development of the electromagnetic shower (shown in Fig. 2.4) can be well described by [61]

$$\frac{dE}{dt} = E_0 b \frac{(bt)^{a-1} e^{-bt}}{\Gamma(a)} \tag{2.4.1}$$

where E_0 is the energy of the incident particle, a and b are free parameters of the model, $\Gamma(a)$ is Euler's Gamma function, and t is the distance measured in radiation lengths ($t = x/X_0$). In this model framework, the shower maximum may be expressed as

$$t_{max} = \frac{a-1}{b} = \ln\left(\frac{E_0}{E_c}\right) + C_{e,\gamma}, \tag{2.4.2}$$

where $C_e = -0.5$ for a electron induced shower and $C_\gamma = +0.5$ for a gamma induced cascade. The shower profile exhibits near energy independence at large depths, a direct result of the photon attention rates ($\lambda_{att} = 1/b$) dependence on the medium rather then energy [58]. Additionally, the longitudinal shower depth with 95% containment may be estimated from equations 2.4.1 and 2.4.2 as [62]:

$$L(95\%) \approx t_{max} + 0.08Z + 9.6[X_0], \tag{2.4.3}$$

in terms of radiation lengths. The transverse shower profile may also be studied extensively with calorimeters, as shown in Figure 2.3, provided that the calorimeters

are segmented on the order of their respective radiation lengths and the lateral distribution can be extracted using equation 2.3.3.

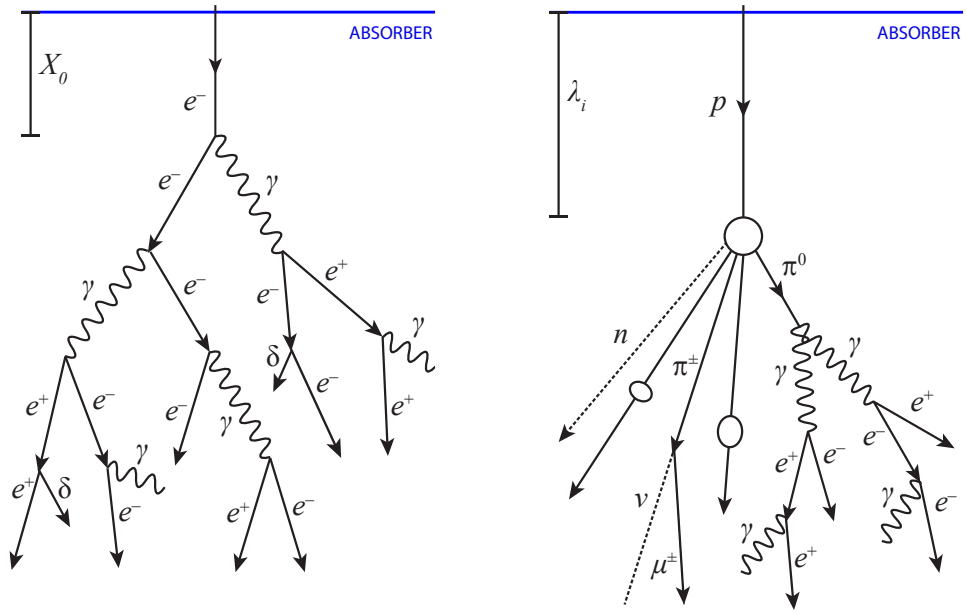

(a) (b)

Figure 2.5: (a) Schematic of an electromagnetic shower (electron). (b) Schematic of a hadronic shower (proton).

2.5 Hadronic Contamination

The leading concern in astoparticle physics experiments measuring the electromagnetic component of cosmic radiation is hadronic contamination in the signal. Analogous to X_0, the nuclear interaction length (λ_i) is much larger and scales as:

$$\frac{\lambda_i}{X_0} \propto Z^{4/3}. \tag{2.5.1}$$

This allows hadrons to penetrate deeper in a medium before secondary production begins from interaction with target nuclei. The schematics of particle showers for

electrons and protons is shown in Figure 2.5a and 2.5b, respectively, to illustrate the differences and similarities between them. The hadronic shower is much more complex than that of electromagnetic particles, consisting of two components, a strong interaction component ($left - side$ of Fig. 2.5b) and an electromagnetic component ($right - side$ of Fig. 2.5b). The fractional energy lose experienced by hadrons through electromagnetic processes via the π^0 channel may be estimated by [63]

$$f_{em} \simeq 1 - \left(\frac{E}{\text{GeV}}\right)^{-0.15}, \tag{2.5.2}$$

where the f_{em} approaches 1 at very high energies. Since hadronic showers will not be fully contained within the electromagnetic calorimeter, high energy protons can imitate lower energy electrons if substantial energy is transferred to π^0s. Therefore, experiments must utilize all information from each subsystem to aid in the discrimination of electrons from the considerable background in order to avoid contamination.

Part II

Instrument Overview

Chapter 3

The Calorimetric Electron Telescope Experiment

The CALorimetric Electron Telescope (CALET) is a forthcoming cosmic ray space-borne experiment involving a multinational collaboration represented by universities and institutes from the United States, Italy, and Japan (Table 3.1). The experiment will build on observations made from other space-based experiments, balloon instruments, and ground-based telescopes. The design of the CALET detector allows for the experiment to provide the highest direct energy measurements of the cosmic ray electron spectrum. There are two instruments aboard the CALET payload: the primary instrument is the Calorimeter (CAL), and the secondary instrument is the Gamma-ray Burst Monitor (CGBM); this study concentrates on the former. In this chapter, will summarize the CALET experiment in it's entirety. In section 3.1, we will briefly discuss the mission and deployment of the CALET payload to the ISS. Section 3.2 will review the scientific objectives of the CALET observations. Finally, section 3.3 will provide an technical overview of the main instrument, CAL.

Table 3.1: CALET International Collaboration

CALET Collaboration

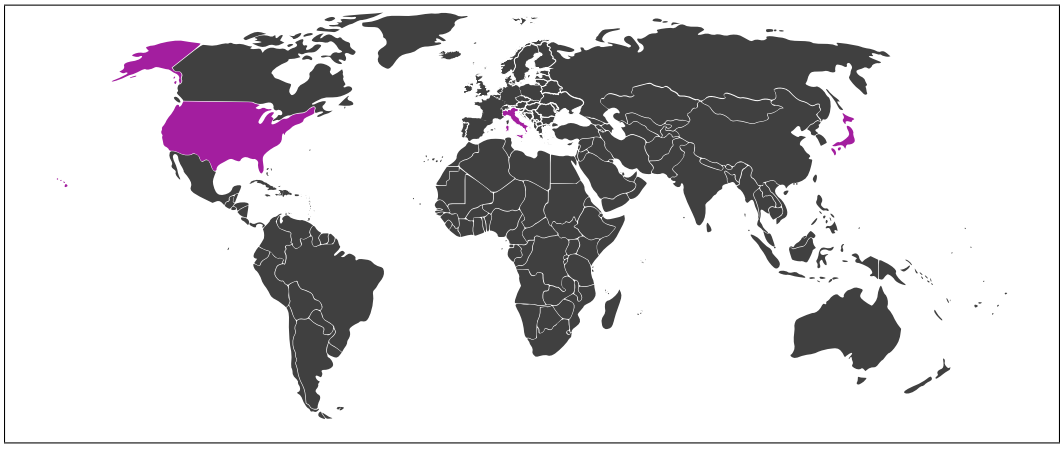

United States
NASA Goddard Space Flight Center (GFSC)
CRESST/NASA/GSFC and U. of Maryland
CRESST/NASA/GSFC and USRA
Washington University-St. Louis
Louisiana State University
University of Denver

Italy
Agenzia Spaziale Italiana Science Data Center
University of Bari and INFN Bari
INAF Istituto di Radioastronomia, Bologna
INAF-IASF, Milano
University of Pisa and INFN
INFN Padova
INFN Perugia
INFN Roma Tor Vergata
INFN Sezione di Bari
INFN Torino
INFN Trieste
University of Udine and INFN-Trieste

Japan
Aoyama Gakuin University
Hirosaki University
Ibaraki University
University of Tokyo and ICRR
JAXA/SEUC
JAXA/IAAS
Kanagawa University of Human Services
Kanagawa University
High Energy Accelerator Research Organization (KEK)
National Institute of Radiological Sciences
Nihon University
Ritsumeikan University
Saitama University
Shibaura Institute of Technology
Shinshu University
Tokyo Technology Institute
Waseda University (PI Institute)
Yokohama National University
Tokiwa University

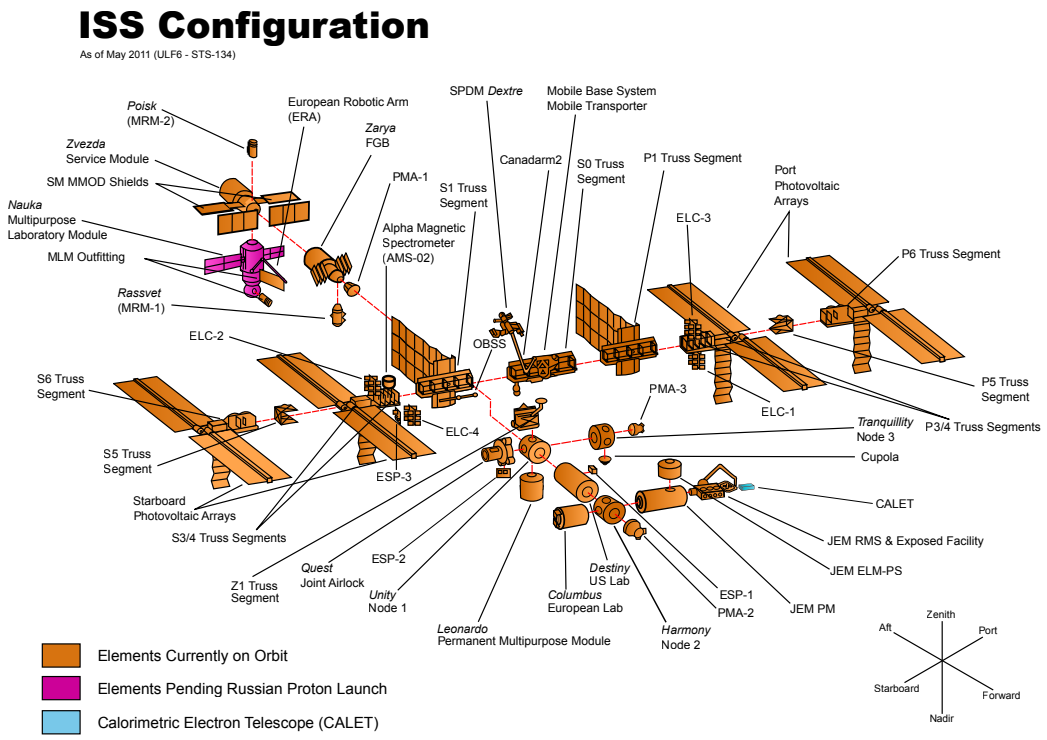

Figure 3.1: Exploded view of the International Space Station elements. Original schematic drawing, credit: NASA

3.1 The CALET Mission

CALET is a Japanese led mission supported by the participating countries respective space agencies: Japan Aerospace eXploration Agency (JAXA), the Italian Space Agency (ISA), and and NASA. The telescope is installed on the Japanese Experimental Module – Exposed Facility (JEM-EF) on the International Space Station (ISS) to perform long duration observations (Fig. 3.1). A recognized experiment of CERN, CALET will produce substantial contributions to the fields of astrophysics and particle physics by detecting cosmic electrons, nuclei, and gamma-rays. CALET will not only build upon results from other cosmic ray experiments but extend direct energy measurements well into the TeV range, with the main objective to measure the detailed shape of the electron spectrum above 1 TeV.

(a) (b)

Figure 3.2: (a) The launch of CALET aboard a Japanese H-IIB carrier rocket. Credit: `JAXA` (b) The extraction of the exposed pallet with CALET from HVT-5. Credit: `NASA/Scott Kelly`

The CALET payload was successfully launched aboard an H-IIB (H2B) carrier rocket from the Tanegashima Space Center in southern Japan on August 19, 2015 (as seen in Fig. 3.2a). Integrated in the H-II Transfer Vehicle (HTV5), CALET rendezvoused with the ISS (Fig. 3.2b) and was robotically positioned at JEM-EF Port # 9 on August 25, 2015. The payload accommodating the two instruments, the CAL and CGRB, has a mass of 650 kg and measures 1.85 L $\times$ 0.80 W $\times$ 1.00 H m^3 (Fig. 3.3). The orbit of the ISS (i.e. CALET) is approximately 400 km in altitude, with an orbital period of 93 minutes. The inclination of orbit is 51.65° relative to the equator and the period of precession is about 60 days. As of today[1], CALET is currently in the hardware *check-out* phase and science operations are set to begin in coming months. The CALET experiment has a mission period of more than 2 years, with the goal of operations to continue for 5 years.

[1] August 26, 2015

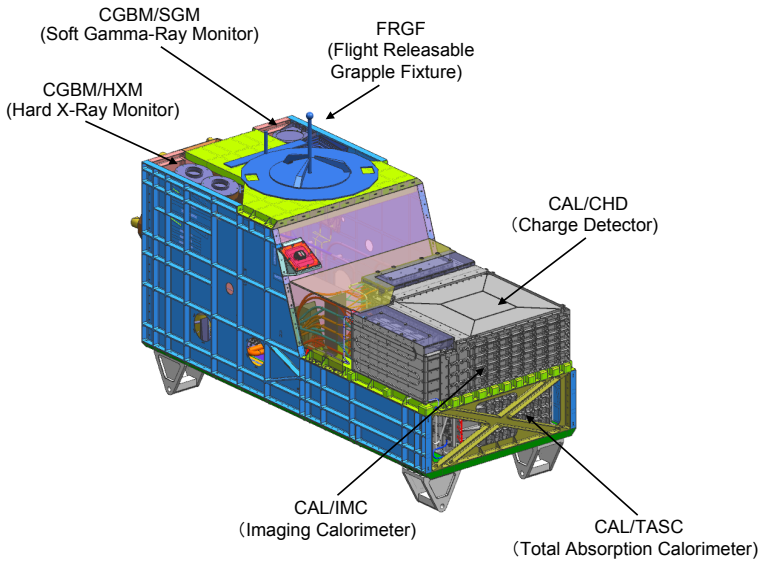

Figure 3.3: Schematic drawing of the CALET payload. Credit: `JAXA/CALET Collaboration`

3.2 Scientific Objectives

The design of the Calorimetric Electron Telescope will allow for identification of particles and nuclear fluxes over a wide energy range, investigating many unanswered questions in physics and astrophysics. The key scientific objectives of the CALET mission as describe in [11, 64] are:

(i) To search for evidence of nearby cosmic-ray sources: pulsars and SNRs;

(ii) To probe the nature of dark matter: cosmic-ray $e^+ + e^-$ and γ-ray observations;

(iii) To provide further understanding about the origin cosmic-rays: exploiting nuclei energy spectra up to iron and beyond;

(iv) To study cosmic-ray propagation in the galaxy: measuring the boron/carbon ratio above TeV per nucleon;

(v) To investigate solar physics: low energy cosmic-ray propagation in the heliosphere; and

(vi) To study the high-energy behavior of gamma-ray bursts and transients;

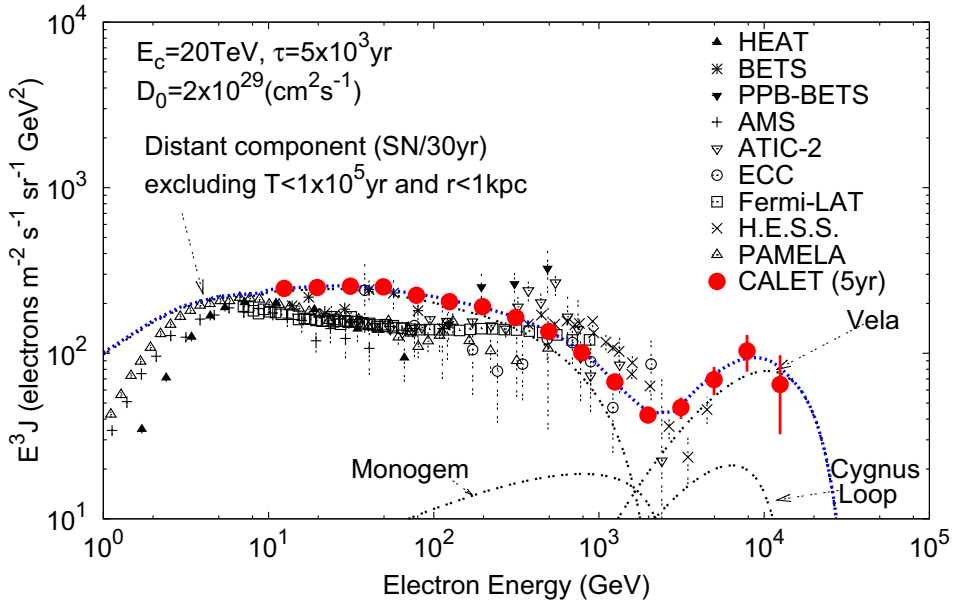

Figure 3.4: Simulated electron energy spectrum from a supernova remnant scenario model as compared with previous observational data from relevant experiments. From [11].

As already mentioned, the primarily scientific objective of CALET is to precisely measure the inclusive electron + positron component of the cosmic radiation for identification of CRE sources beyond a TeV. The potential of the instrument is shown in Fig 3.4. The red data points show a simulated electron energy spectrum composed of contributions from nearby SNR (Vela, Monogem and the Cygnus Loop). After 5 years of observations, CALET will be able to accurately resolve Vela in this model. CALET will also have the unique capability in searching for and resolving sharp spectral lines in the high energy diffuse background well beyond current limits of gamma-ray observations. These measurements will allow for CALET to perform a sensitive search for dark matter candidate signatures from annihilation and/or decay (see Sect. 1.4.3). Additionally, CALET will extend direct measurements of cosmic ray H, He, heavy-ion, and ultra-heavy (*trans*-Fe) spectra beyond practical limits

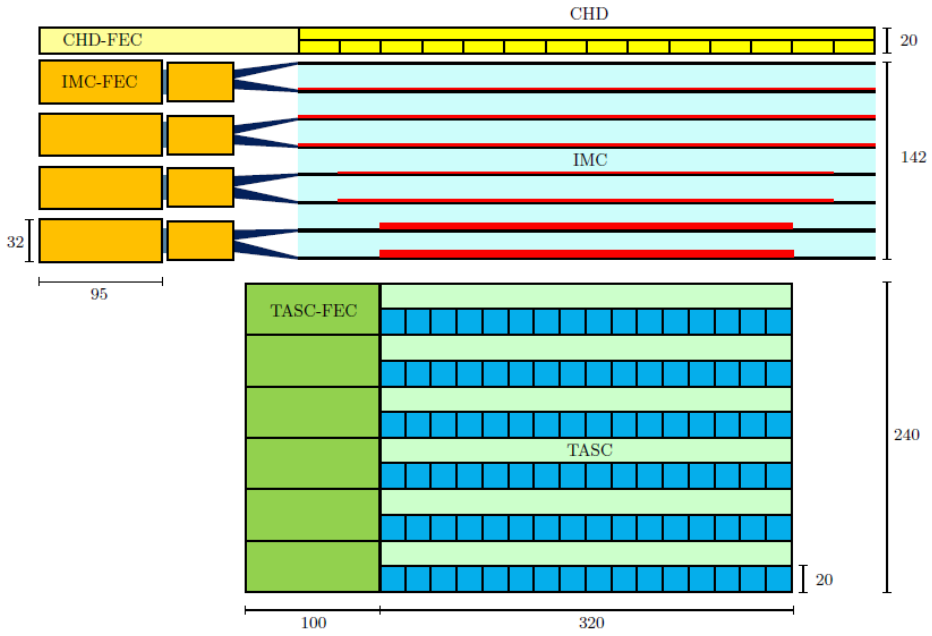

Figure 3.5: Schematic overview of the CALET CAL instrument with measurements of the individual components (in mm). Credit: `JAXA/CALET Collaboration`

of balloon experiments into a previously unexplored energy region, achievable only by long exposure of a space experiment. These observations are essential in testing cosmic ray propagation and acceleration models. For a more detailed discussion of the scientific objectives, the reader is encouraged to see the above references.

3.3 The CALET-CAL Instrument[2]

The CALET - CAL is designed to measure the directions, energies, and arrival times of incident charged cosmic rays (and gamma-rays) over a field-of-view of approximately 45° from the zenith of the detector. The CAL is constructed of a segmented, thin, charged particle detector, a particle tracking detector, and a calorimeter; each with an electronic module (*front-end circuits*) located adjacent in

[2]The subsections within use information from the respective references at the beginning of the subsection, see for more detailed review.

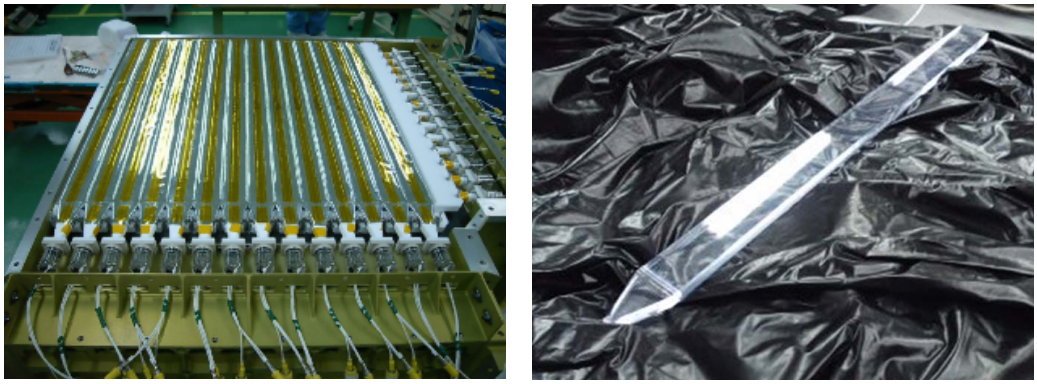

(a) (b)

Figure 3.6: (a) The fight model of the CHD, with 2 layers of 14 scintillating paddles and attached PMTs. (b) A prototype of a CHD plastic scintillator paddle. Credits: `JAXA/IA` (two figures).

the structure. The designations of the main subsystems of the CAL instrument are (see Fig. 3.3):

- Charge Particle Detector (CHD)
- Imaging Calorimeter (IMC)
- Total Absorption Calorimeter (TASC)

3.3.1 Charge Detector

The charge detector (CHD) [65] is designed to provide a measurement of the absolute charge of the incident particle before penetrating the main volume of the calorimeter. Using the fundamental principle of the energy loss dependence on Z^2, the CHD is able to resolve charged nuclei up to $Z = 40$. This allows for the control of the data rate at the trigger level while maintaining the capabilities to measure the flux of higher charge nuclei. One should note, that *quenching* effects in the scintillators result in weaker charge scaling as Z increases and in reality the energy loss dependence is $Z^{<2}$. The CHD is composed of two layers of plastic scintillators (Fig. 3.6b), where each layers consist of 14 paddles, each measuring 44.8 $\times$ 3.2 cm $\times$

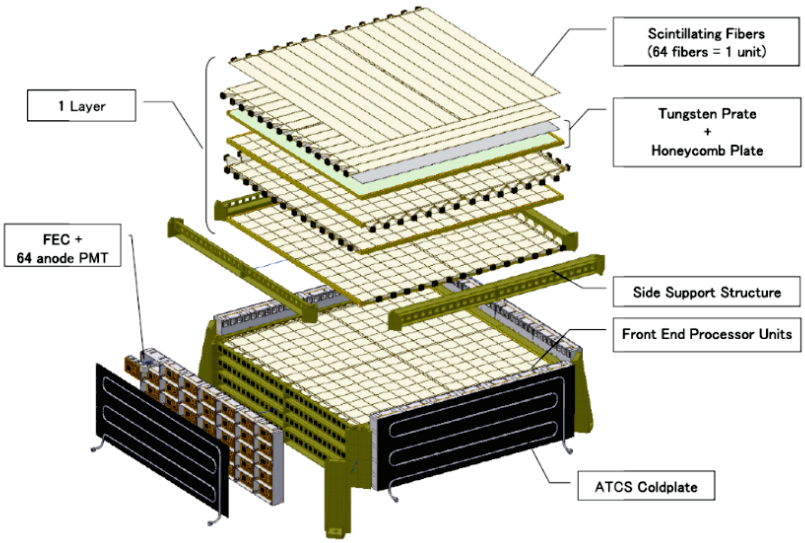

Figure 3.7: An exploded view of one layer of the imagining calorimeter, with support structure and front-end electronic components. Credit: `JAXA/CALET Collaboration`

1.0 cm (Fig. 3.6a). The layer geometry is arranged orthogonally to provide an X and Y view of the traversing particle with a granularity of about 3.2 $\times$ 3.2 cm^2. Each paddle is optically isolated and read out by a photomultiplier tube (PMT) located at the end of the CHD (alternates between views), through an acrylic light guide for the scintillating photons.

3.3.2 Imaging Calorimeter

The Imaging Calorimeter (IMC) [66, 11] is composed of 8 x-y planes (16 total layers) of scintillating polystyrene fiber (SciFi) belts orthogonally arranged to provide two independent transversal views of the shower development (see Fig. 3.7). The bottom 7 x-y planes are additionally interleaved with tungsten plates of increasing thickness and decreasing area, with approach to the bottom of the IMC. The first three tungsten plates measure 44.8 cm $\times$ 44.8 cm $\times$ 0.07 cm *thick* and next two are 38.4 cm $\times$ 38.4 cm $\times$ 0.07 cm *thick*, each with a radiation length (X_0) of 0.2. The

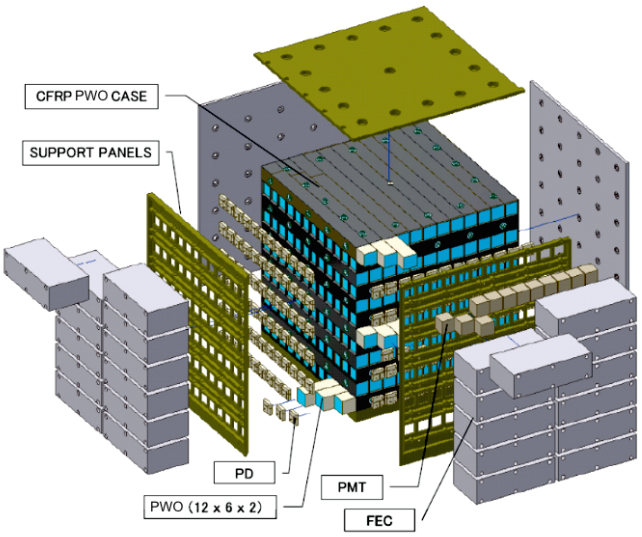

Figure 3.8: An exploded view of the total absorption calorimeter, with support structure and front-end electronic components. Credit: `JAXA/CALET Collaboration`

last two tungsten plates are each $1X_0$ thick and have a dimension of 32.0 cm $\times$ 32.0 cm $\times$ 0.35 cm, the equivalent area of the calorimeter below. The total depth of the IMC is $3X_0$ and with a nuclear interaction length λ_I of 0.11, in depth.

A single plane consists of 14 SciFi belts, each measuring 44.8 cm $\times$ 3.2 cm, approximately the size of a scintillating paddle in the CHD. The fibers are 44.8 cm long and have a cross section of 1 mm^2 with fine granularity. The total surface area of each SciFi plane is 44.8 $\times$ 44.8 cm^2 and the distance between layers is about 2 cm. The SciFi layers are readout by a multi-anode photomultiplier tube (MA-PMT) to the *front-end* electronics.

3.3.3 Total Absorption Calorimeter

The total absorption calorimeter (TASC) [67, 66, 68] is designed to provide the energy measurement of electromagnetic particles to produce crucial information for hadronic background rejection while imaging in the particle shower. The calorime-

ter subsystem (Figure 3.8) is composed of 12 layers of 16 lead tungstate (PWO) scintillation crystals, individually measuring 32.6 cm × 1.9 cm × 2.0 cm, for a total 192. The layers in the TASC are aligned in alternating x and y directions for all 12 layers, forming a horoscopic array of optically isolated crystals. The top layer is used for event triggering and the scintillation light is read out by PMTs. The remaining 11 layers are read out by a dual avalanche photodiode and photodiode (APD/PD). The TASC has a very high dynamic range, designed to detect signals from a few photoelectrons of minimum ionizing particles (MIPs) to about $\sim 10^6$ photoelectrons of electromagnetic showers in the trans TeV range. The TASC is a fully-active calorimeter with a surface area 32.6 × 32.6 cm^2 and a total depth of ∼27 X_0 or 1.2 λ_i at normal incidence, allowing for excellent longitudinal shower energy measurement, up to 10 TeV for electromagnetic particles. The estimated energy resolution of high energy electrons and gamma-rays up to 10 TeV is approximately 2%; where as for nuclei, a 1 TeV proton has an estimated resolution of about 40%, and heavier nuclei is roughly 30% at 50 GeV per atomic mass unit.

3.3.4 On-board Trigger System

One of the main challenges of cosmic rays experiments is suppressing the vast background in order to measure CREs efficiently. An on-board trigger system has been developed for CALET using beam test and simulation studies, to control the background of cosmic ray protons, ions, neutrons, albedo gamma-rays, etc. that will interact inside the calorimeter. There are two fundamental trigger systems for the calorimeter in CALET [69, 68]:

1. **High Energy Shower (`HES`) mode – the main observation trigger.** Selects events that produce large signals in the bottom two layers of the IMC and the first layer in the TASC, consistently associated with particles of energy

$E > 10$ GeV. The HES mode conditions are:

(a) IMC Layer 7 $>$ 7.5 MIPs[1],

(b) IMC Layer 8 $>$ 7.5 MIPs[1],

(c) TASC Layer 1 $>$ 55 MIPs[2].

These requirements ensure the selections of events that strongly interact within the detector, suppressing the extensive low energy proton background while preserving the electromagnetic sample. Since the HES trigger allows for the additional acceptance of gamma–rays, the IMC threshold has been established such that $> 98\%$ of 10 GeV gamma–rays that undergo conversion above layer 7 will be observed; and the TASC threshold allows for $> 95\%$ of 10 GeV electrons to be detected[67]. Furthermore, this trigger accepts events entering from the side of the detector at acute angles. The remaining events triggered by the HES mode are transmitted to the ground for further analysis.

2. **Single (`SI`) mode – in-space calibration trigger.**
Selects events that pass through the CHD, IMC, and TASC for the on-orbit calibration of the detector. The SI mode conditions are:

(a) CHD $>$ 0.7 MIPs,

(b) IMC Layers 1 – 8 $>$ 0.7 MIPs/per layer[1],

(c) TASC Layer 1 $>$ 0.7 MIPs[2].

These requirements ensure the selections of only events that traverse all subsystems in the instrument. Further selection criteria will be applied to these triggered events offline, with the objective to isolate protons (or helium) that do not interact in the CHD and create showers in the IMC for continuing energy calibration of the CALET calorimeter during it's lifetime.

There is a third trigger that will be employed periodically to study solar activity at high altitudes.

3. **Low Energy Shower (LES) mode – solar modulation trigger.**

   Selects events that produce increasing signals while passing through the CHD, IMC, and TASC; associated with particles of energy $E > 1$ GeV[70]. The LES mode conditions are:

   (a) CHD > 0.7 MIPs,

   (b) IMC Layers 1 – 6 > 0.7 MIPs/per layer[1],

   (c) IMC Layers 7 – 8 > 5 MIPs/per layer[1],

   (d) TASC Layer 1 > 7 MIPs[2].

   These requirements ensure a selection of interacting events with a detection efficiency of $> 95\%$ of 1 GeV electrons. This trigger will be used to study solar activity at cutoff rigidity less than 2 gigavolts (GV).

Note there is an additional CAL trigger that works in conjunction with the CGRB trigger, where the calorimeter threshold is reduced to 1 GeV to observe a GRB-induced signal.

[1]Within the IMC, 1 MIP unit number is $\sim$ 300 keV in 2 (X,Y) fibers.

[2]Within the TASC, 1 MIP unit number is $\sim$ 20 MeV in 1 PWO log at normal incidence.

Chapter 4

Fermi Gamma-ray Space Telescope Experiment

The Fermi Gamma-ray Space Telescope (*Fermi*), is a current gamma–ray space-borne observatory involving an international collaboration represented by universities and institutes from 12 different countries (see Table 4.1). The *Fermi* experiment brings together scientists from the astrophysics and particle physics communities, exploring the most extreme environments in the universe and studying subatomic particles at energies well above the achievable limit by terrestrial accelerators. There are two instruments aboard the *Fermi* spacecraft (Figure 4.1): the primary instrument is the Large Area Telescope (LAT), and the complimentary instrument is the Gamma-ray Burst Monitor (GBM); this study focuses on the former. In this chapter, we will provide an overview of the *Fermi* experiment in it's entirety. In section 4.1, we will briefly discuss the mission and deployment of the *Fermi* satellite. Section 4.2 will address the scientific objectives of the *Fermi* observations and notable contributions. Finally, section 4.3 will provide an technical overview of the principal scientific instrument, the LAT.

Table 4.1: Fermi Gamma-ray Space Telescope International Collaboration

***Fermi* Collaboration**

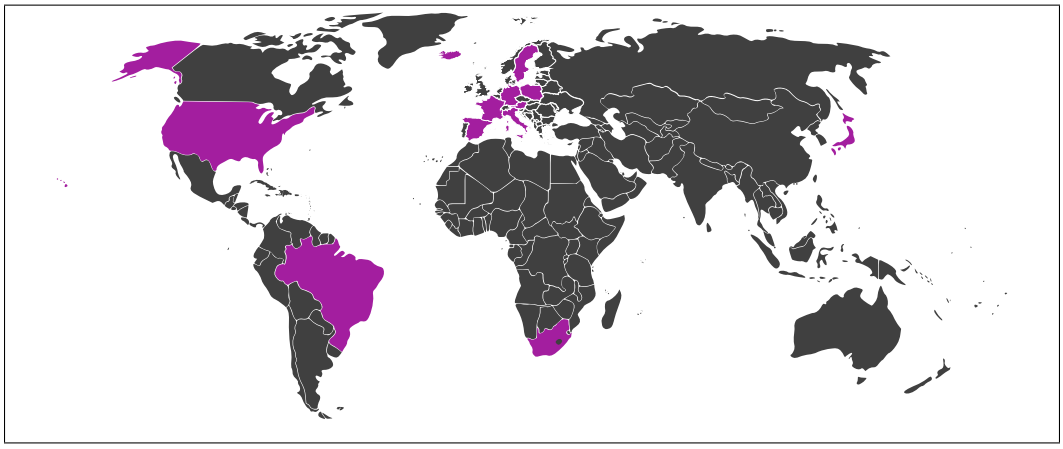

United States
CRESST
Clemson University, Kinard Lab of Physics
Naval Research Laboratory (NRL)
NRL and George Mason University
NRL and Praxis Inc
NASA Ames Research Center
NASA Goddard Space Flight Center
NASA Marshall Space Flight Center
NYCB Real-Time Computing Inc.
Purdue University - Calumet
SLAC National Accelerator Laboratory
Sonoma State University
Stanford University
W. W. Hansen Experimental Physics Laboratory
The Ohio State University
University of Alabama in Huntsville
University of California, Irvine
UCSC, Santa Cruz Institute for Particle Physics
University of Denver
University of Washington
Austria
Universität Innsbruck
Brazil
Universidade de São Paulo, Instituto de Astronomia
France
Centre Etudes nucleaires de Bordeaux Gradignan
IRAP CNRS
Laboratoire AIM, Saclay
Université d'Orléans and CNRS Laboratoire Leprince-Ringuet, École polytechnique
Laboratoire Univers et Particules de Montpellier
Germany
DESY Zeuthen
Erlangen Centre for Astroparticle Physics (ECAP)
Max-Planck Institut für extraterrestrische Physik
Max-Planck-Institut für Physik, München
Iceland
University of Iceland
Italy
Agenzia Spaziale Italiana Science Data Center
INAF Istituto di Radioastronomia, Bologna
INAF-IASF, Milano
INFN and University of Padova
INFN and University of Perugia
INFN and University of Pisa
INFN and University of Roma Tor Vergata
INFN and University of Sezione di Bari
INFN and University of Torino
INFN and University of Trieste
INFN and University of Udine
Japan
Hiroshima University, Astrophysical Science Center
Hiroshima University, Physical Sciences Department
Ibaraki University
JAXA/IAAS
Rikkyo University
Solar-Terrestrial Environment Lab, Nagoya
Tokyo Institute of Technology
University of Tokyo
Waseda University
Poland
Jagiellonian University
South Africa
University of Johannesburg
Spain
Institute of Space Sciences (IEEC-CSIC)
Sweden
KTH Royal Institute of Technology
Stockholms Universitet

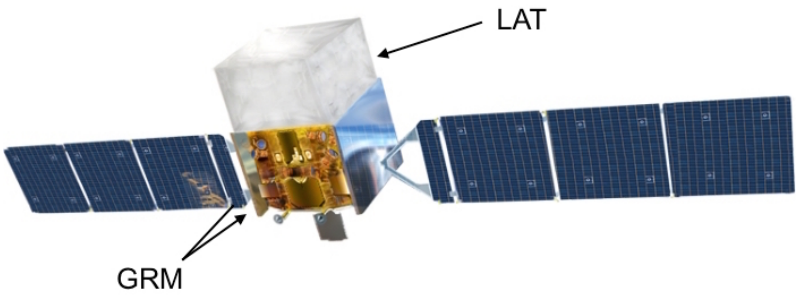

Figure 4.1: Artistic rendering of the Fermi Gamma-ray Space Telescope satellite. Credit: `NASA/Sonoma State University/Aurore Simonnet`.

4.1 The *Fermi* Mission

Fermi is a joint mission of NASA (National Aeronautics and Space Administration), the United States Department of Energy (DOE), and government agencies in France, Germany, Italy, Japan, and Sweden. Formerly known as the Gamma-ray Large Area Space Telescope (GLAST), the observatory was renamed shortly after first light in honor of Enrico Fermi, a pioneer in the field of high energy physics. The primary instrument, LAT, is considered to be the successor to the Energetic Gamma Ray Experiment Telescope (EGRET), with substantial improvements in sensitivity and resolution by more than a factor of 30, as well as extending the observational energy range up to 300 GeV [10]. *Fermi* was able to produce a comparable map of the entire diffuse gamma-ray sky in a matter of days, while EGRET spent years to accomplish this task. The observatory has made unprecedented contributions to further our understanding of the high energy Universe around us and this will be discussed in further detail in the next section.

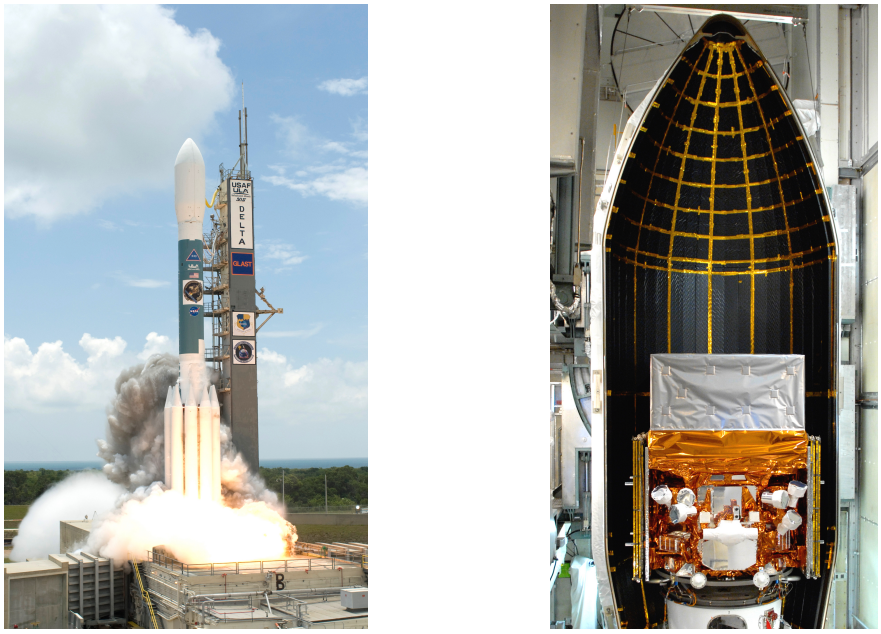

(a) (b)

Figure 4.2: (a) The launch of the *Fermi* (GLAST) spacecraft aboard a Delta II 7920-H rocket. (b) The *Fermi* spacecraft in the payload fairing, LAT is located at the top and GRB is on the front and back side. Credits: `NASA` (two figures).

The *Fermi* satellite was successfully launched into orbit on June 11, 2008 from Cape Canaveral, Florida, aboard a Delta II 7920-H rocket (as seen in Fig. 4.2a). The payload housing the two instruments, the LAT and GBM, weighs approximately 4,300 kg and measures 2.9 m in height and 1.8×1.8 m^2 in width (shown in Fig. 4.2b). The observatory was placed into low Earth orbit at an average altitude of 565 km, orbiting approximately every 96 minutes. The inclination of orbit is 25.6° relative to the equator and the period of precession is about 55 days. At any given moment in orbit, the telescope is able to observe $\sim$ 20% of the sky, which allows the an entire sky image to be taken in roughly 3 hours [10]. *Fermi* has been in orbit for more than 7 years now, and is currently in the extended mission phase. The design lifetime of the experiment was 5 years, although, the mission goal for operations is to continue through to 2018.

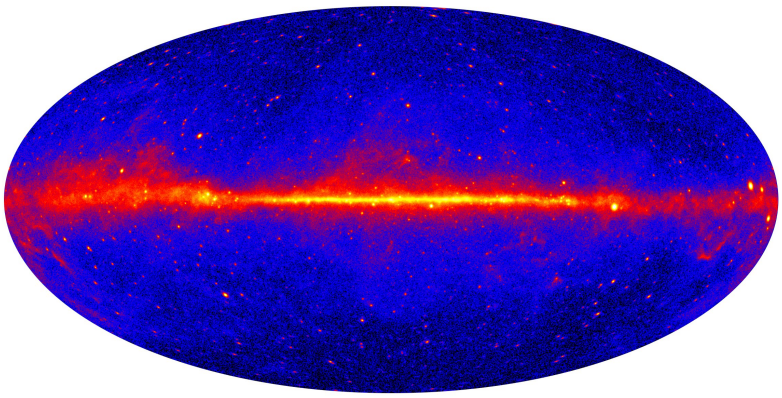

Figure 4.3: All-sky gamma-ray map in galactic coordinates, as seen by Fermi LAT with 5 years of data (Energy $>$ 1 GeV). Credit: `NASA/DOE/Fermi LAT Collaboration`.

4.2 Scientific Objectives

The design of the Fermi Gamma-ray Space Telescope has allowed for a wide array of investigations to address many unanswered questions in physics and astrophysics. The key scientific objectives of the *Fermi* mission as describe in [10]:

(i) To resolve the γ-ray sky: the nature of unidentified sources and origins of diffuse emission;

(ii) To provide understanding about the mechanisms of particle acceleration in various sources such as: active galactic nuclei, pulsars, supernovae remnants, and the Sun;

(iii) To study the high-energy behavior of the most powerful explosions in the Universe: gamma-ray bursts and transients;

(iv) To search for signs and identify the composition of dark matter through γ-ray observations (additionally, cosmic ray electron observations); and

(v) To probe the early universe and the evolution of high-energy sources of γ-rays sources.

Already stated, *Fermi* has made countless contributions in gamma-ray astronomy, addressing all above key objectives and is continually widening the purview of study. A Figure-of-Merit (FOM) of the experiment is shown in Figure 4.3, a high resolution all-sky map in the gamma-ray spectrum above 1 GeV, with a number of discovered gamma-ray sources. *Fermi* has also provided further insight of the seemingly intangible dark matter candidate (WIMP), observing what may be a gamma-ray signal from DM annihilation (see [71] and Refs. therein). Although, the LAT instrument was designed to observe gamma-rays, *Fermi* has produce high statistics measurements of the cosmic ray electron spectrum up to about 1 TeV (already shown in Figs 1.7 and 1.8). As this brief discussion does not do the observatory justice, the reader is encouraged to explore more about the notable contributions made by the Fermi Gamma-ray Space Telescope at Ref. [72].

4.3 The Fermi-LAT Instrument[1]

The Fermi-LAT is designed to measure the directions, energies, and arrival times of the incident gamma-rays (and other charged particles) over a wide Field-of-View. The LAT is constructed of a 4×4 array of identical towers (16 total), each composed of a particle tracking module, a calorimeter module, and an electronic module at the base of the tower. A segmented anticoincidence detector encloses the towers on the top and all four sides. The surface area of the LAT instrument is 1.8×1.8 m^2 and has a height of 0.72 m. The designations of the main subsystems of the LAT instrument are (see Fig. 4.4):

- Anticoincidence Detector (ACD)
- Precision Converter–Tracker (TKR)
- Calorimter (CAL).

[1]The subsections within use information from the respective references at the beginning of the subsection, see for more detailed review.

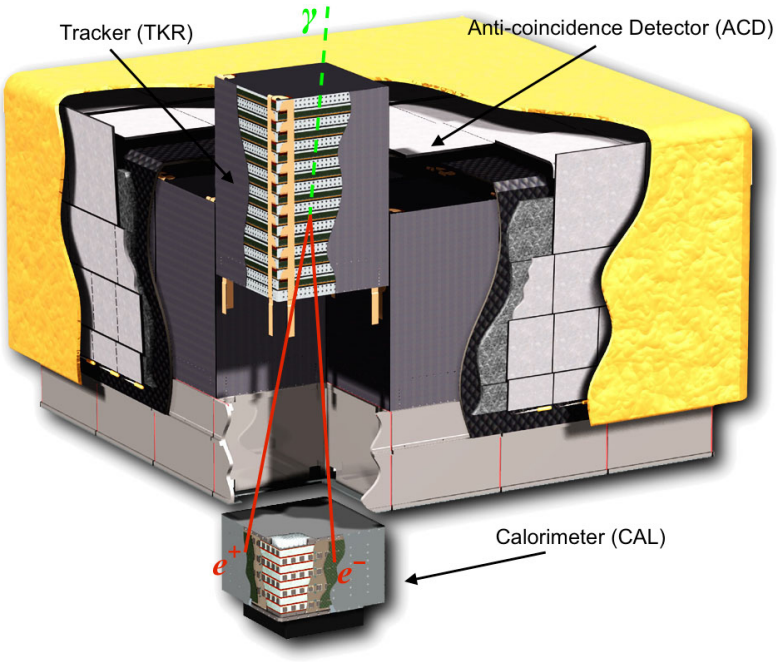

Figure 4.4: A schematic cutaway diagram of the LAT instrument with an incoming photon annihilating into an e^+e^- pair. Credit: NASA

4.3.1 Anticoincidence Detector

The anticoincidence detector (ACD) [73] has a primary purpose of tagging incident particle before they enter the main volume of the telescope. This allows LAT to distinguish charged cosmic rays from traversing gamma-rays. The ACD is segmented into a total of 89 plastic scintillator tiles (∼1 cm thick), decreasing in lateral dimension as the location approaches the calorimeter (see Fig 4.5). The top face of the ACD consists of a 5 × 5 array of 32 cm × 32 cm tiles. The sides contain 4 rows tiles reducing to 15 cm × 32 cm by the third row, with the bottom row consisting of one long tile measuring 17 cm × 170 cm. Each tile is read out by two photomultipliers tubes (PMTs) located at the bottom of the ACD, through wavelength-shifting fibers embedded within the tile to collect the scintillating photons. Satisfying design requirements, the ACD has shown to have a 0.9997 detection efficiency for the charged particles.

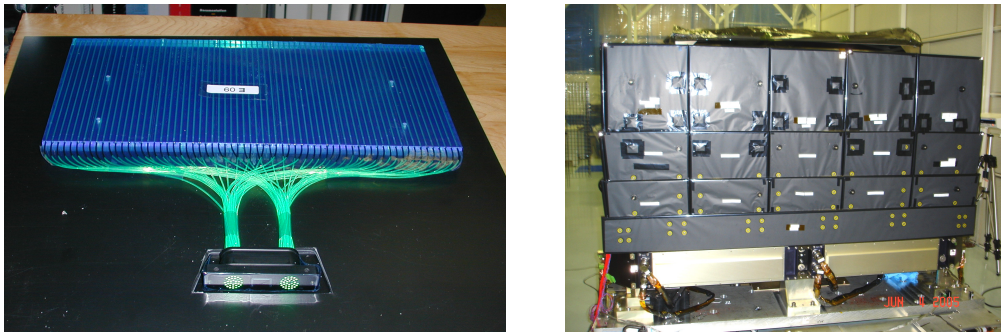

(a) (b)

Figure 4.5: (a) A flight model anticoincidence scintillator tile with wavelength-shifting fibers embedded. (b) The assembled ACD, integrated with the tracker and calorimeter modules. Credits: NASA (two figures)

4.3.2 Precision Converter–Tracker

The precision converter-tracker (TKR) [74] is composed of the 18 x, y planes (36 total layers) of single-sided silicon strip detectors (SSDs) with the top 16 planes interleaved with tungsten conversion foils. The physical structure of the TKR is divided into 19 *trays* (support panels), where the top and bottom trays contain parallel layers of SSDs in the y direction. The intermediate 17 trays consist of two parallel planes of the SSDs, alternating in direction orthogonally between trays, providing x, y position measurements of the traversing particle(s). The top 12 trays (*front* section) contain thin tungsten conversion foils located directly above the upper detector layer with a thickness of $0.035X_0$ (radiation length). The subsequent 4 trays (*back* section) consist of thick tungsten conversion foils at $0.18X_0$ each, and the bottom 3 trays do not contain any conversion material. The total depth of the tracker at normal incidence is $1.5X_0$, allowing electromagnetic particles to induce cascades.

A single SSD layer is constructed of 16 microstrip silicon sensors (8.85 $\times$ 8.95 cm^2) with a strip pitch of 228 μm, where four sensors are grouped together to form

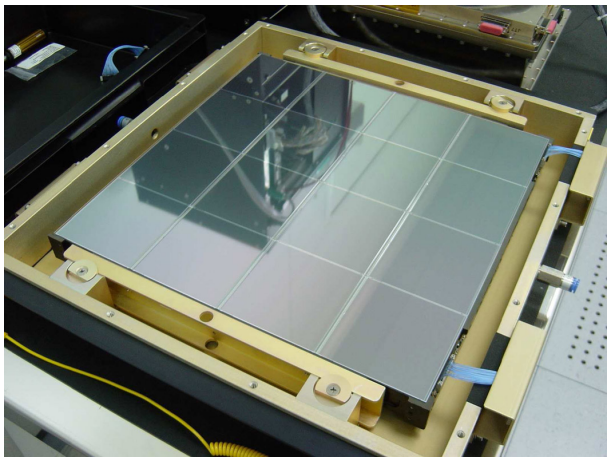

(a)

(b)

Figure 4.6: (a) A tracker tray in the flight model, with SSD Bi-layer, readout electronics, and support structure. (b) A complete tracker module, with a side wall removed. Credits: NASA (two figures)

readouts in four ladders (Fig. 4.6a). The tracking subsystem consists of over 9k single-sided sensors with a hit efficiency for charged particle better than 99%. The total effective area of approximately 73 m^2 for all towers with 880k readout channels (Fig. 4.6b).

4.3.3 Calorimeter

The calorimeter (CAL) [75] is designed to provide measurement of the energy of electromagnetic particles and image the shower development profile. The CAL provide crucial information for background rejection and energy *leakage* estimation for a partially contained shower. A calorimeter module (Fig. 4.7) is composed of 8 layers of 12 cesium iodide scintillator crystals doped with thallium (CsI(Tl)), individually measuring 2.7 cm $\times$ 2.0 cm $\times$ 32.6 cm, for a total of 96 in each tower. Each crystal element is optically isolated and the generated scintillation light is read out by two PIN diodes at each end. The layers in the CAL are aligned in alternating x and y directions for all 8 layers, forming a horoscopic array. The total depth of the

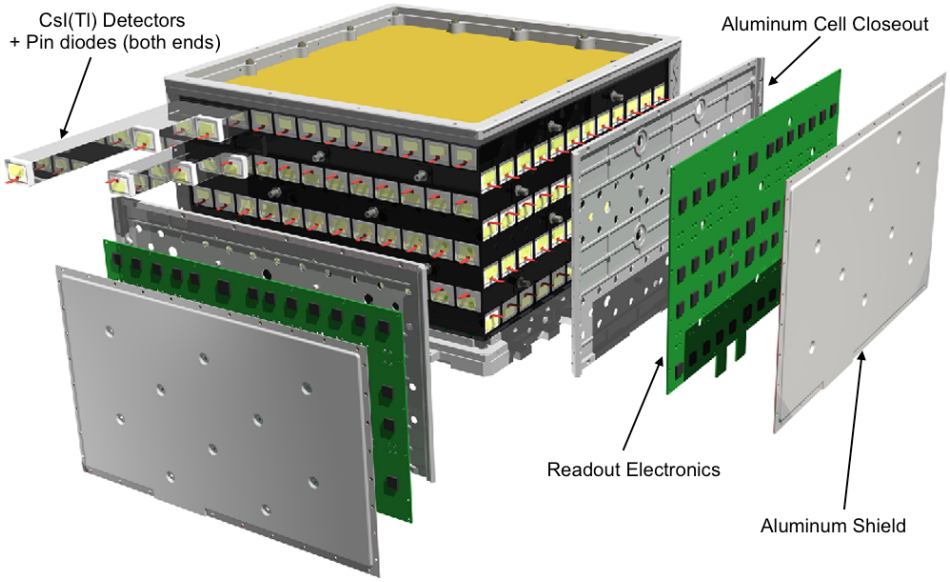

Figure 4.7: Schematic drawing of the calorimeter module, consisting of the 96 (CsI(Tl)) crystals in 8 layers, orthogonally arranged. Credit: NASA

calorimeter is $8.6X_0$ at normal incidence ($\lambda_i \sim 0.43$), allowing for sufficient longitudinal shower energy measurement, up to 1 TeV for electromagnetic particles.

The CAL can provides three spatial coordinates: the x coordinate and y coordinate of the crystal, as well as the position of the traversing particle along the crystal's axis alignment. The latter is achieved by measuring the intensity ratio of light received by the diodes at the ends of the crystal. Two diodes with widely different gains are employed to cover a wide dynamic range and provide position measurement accurate to a fraction of millimeter for energy deposit above 1 GeV. This enables the CAL to reconstruct a 3-dimensional image of the particle shower. There are a total of 1536 CsI(Tl) crystals in the LAT instrument, having an active area of 1080 cm^2 per module with $> 90\%$ active material. The energy resolution of the CAL is less than 10% at 10 GeV and reduces to less than 6% at 300 GeV for an incident angle of 60 degrees.

4.3.4 On-board Trigger and Filter System

An on-board event processing system has been developed for LAT using beam test and simulation studies, to control the cosmic background that continually bombards the detectors. The event processing is accomplished at two levels: (1) the hardware level, where particular signals in the detectors initiate a trigger; and (2) the software level, where event filtering occurs to reduce the data rate of transmission to the ground [76].

1. **Hardware Event Trigger**

   Each subsystem produces one or more *trigger primitives* when an incident particle enters the LAT instrument:

   - `TKR`: generated when signals above the threshold (0.25 MIPs) occur in three consecutive bi-layers (x and y), indicating possible track.
   - `CAL_LO`: generated when a signal in any single crystal is above $\sim$ 100 MeV at one end.
   - `CAL_HI`: generated when a signal in any single crystal is above $\sim$ 1 GeV at one end.
   - `ACD(Veto/RoI)`: generated when a signal in any single tile is above the threshold (0.45 MIPs). RoI primitive issued if tile shadows the tracker module where TKR primitive occurs.
   - `CNO`: generated when a signal in any single tile is above the heavy ion threshold (25 MIPs).
   - `Periodic`: generated periodically ($\sim$ 2 Hz) during data collection for diagnostic and calibration analysis.

The set of hardware trigger primitives are mapped into the *trigger engines*, where all possible combination are considered. If certain criteria are satisfied, a read out is initiated for all subsystems and an event is established for filtering.

2. **Software Event Filter**

   Multiple on-board filters are implemented on LAT allowing for rough event selection from the full instrument information:

   - `GAMMA`: selects gamma-rays through a sequence of veto tests, efficiently eliminating charged cosmic rays. One important feature is the High Energy Pass (or High Pass Filter), automatically accepts events that deposit energy greater than 20 GeV since the event rates are relatively low in this energy range.
   - `HIP`: selects heavy ion event candidates for calorimeter calibration
   - `DGN`: selects unbiased samples of all trigger types for instrument performance monitoring (every 250th event is tagged).

   Once an event passes a filter, it is tagged for downlink to the ground for further analysis. Since the filters are implemented at the software level, they allow for revisions and additions from the ground.

Part III

Multivariate Analysis Approach

Chapter 5

Boosted Decision Trees

In high energy physics and astrophysics, it has become common practice to identity rare events amongst a vastly larger background in order study nature at the most fundamental level. With the advent of modern particle detectors, data analysis became more complex and the demand for more robust techniques beyond traditional methods were required. The development of machine learning algorithms revolutionized multivariate data analysis, and demonstrated successful applications across various disciplines. In the last decade, many particle physics experiments have employed modern multivariate analysis techniques and have provided some of the most important results in physics today (see [77] and Refs. therein).

An important attribute of multivariate analysis (MVA) methods is its ability to reduce dimensionally of feature space through correlations between observed characteristics of objects or events and preform classification. The focus of this chapter will be on the MVA technique applied in this work for particle identification, known as, *Boosted Decision Trees* (BDTs). Section 5.1 will introduce the fundamentals of decisions trees, and the boosting implementation will be discuss in sections 5.2.

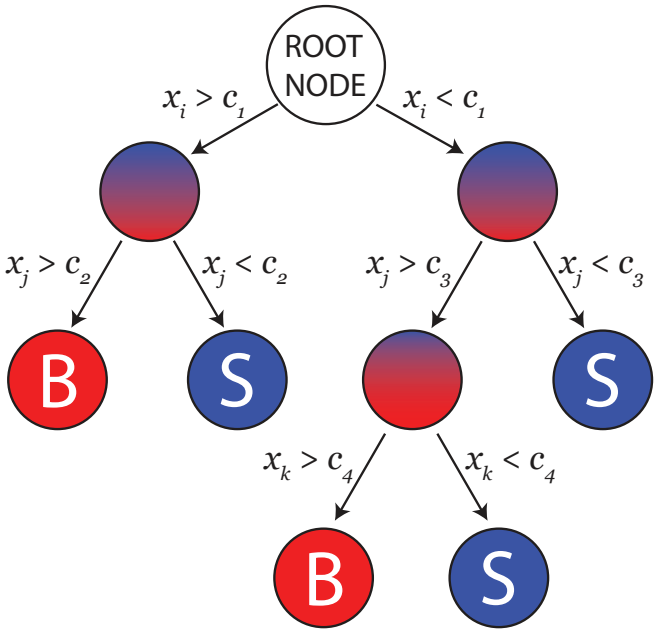

Figure 5.1: Simplified Decision Tree Schematic

5.1 Decision Trees

A *decision tree* (DT) is a supervised machine learning technique for classification[1] that employs recursive partitioning, or the *divide and conquer* strategy, on data to achieve a particular conclusion [78]. In practice, DTs are constructed using a data set with known inputs and outcomes to developed a predictive model for future application. The basic structure of a two-class DT is a binary tree, shown in Figure 5.1, where the result is classified as either signal or background. The binary tree begins at the so-called root node with the complete set of data from signal and background observables. The root node splits the events in two separate branches by the most discriminating attribute x_i of the data set, forming two internal nodes (child nodes). These nodes then partition the data using an additional observable x_j at an optimal split location that provides the largest reduction in impurity of respective data.

[1]Commonly used in regression analysis, however, our focus is classification.

This process continues (applying on $x_k, \dots$) until the terminal criteria is satisfied, resulting in a terminal node (or leaf) where the data is assigned to a class (i.e. signal or background).

When constructing a decision tree, there are different separation criteria that may be implemented to measure the impurity at given node, and provide the optimal partition attribute and location. The function we use in this analysis to quantify the impurity of signal relative to the background is the *Gini index* [79]:

$$Gini(D) = 1 - \sum_{i=1}^{c} p_i^2, \tag{5.1.1}$$

where p_i is the probability of data sample D belonging to class i of c total classes, estimated by $|D_i|/|D|$. In the case of two distinct classes, signal and background, the Gini index may be simplified to

$$Gini(D) = 2p(1-p), \tag{5.1.2}$$

where $p = S/(S+B)$ is the the measure of signal purity with $S(B)$ as total number of signal (background) events. This symmetric function is maximum at the point where the classes are equally distributed ($p = 0.5$), and a minimum when the data sample is pure of either signal or background ($p = 0$ or 1). The partitioning criterion at any given node considers all attributes and their respective Gini index, as well as, all cut values. The maximum separation gain by a binary split can be attained by maximizing the *Gini Gain* [78], defined as

$$\begin{aligned} \Delta Gini(x, D) &= Gini(D) - Gini(x, D) \\ &= Gini(D) - \frac{|D_1|}{|D|} Gini(D_1) - \frac{|D_2|}{|D|} Gini(D_2) \end{aligned} \tag{5.1.3}$$

where $D_{1,2}$ is the partition of D induced by the value of attribute x. The largest change from equation 5.1.3 corresponds to the largest reduction impurity, thus, the split location of data set D in the parent node to create the children nodes with data sets D_1 and D_2. The branching process with no longer continue once the node possesses the minimum number of events, and a purity value will be assigned to the leaf.

5.2 Boosting

Decision trees are robust classifiers, but can exhibit instability as a result of strong dependance on training data. Any slight variation or fluctuation within the data can considerably alter the tree and affect the predictive outcome on future inputs. The use of boosting was introduced to resolve the issue of stability by creating a forest of weak classification trees to construct one very powerful one. The trees are created in sequence where the misclassified training events in the current classifier are effectively weighted (or boosted) to increase their significance in the succeeding tree, and this procedure is continually repeated to build an ensemble. Ultimately, a single classifier is formed by the weighted average of the individual decision tree outcomes.

There are several boosting algorithms that may be applied to decision trees, and the main differences originate from the way the algorithm weights the training events. In this study, we adopt the discrete boosting method known as, *AdaBoost* or adaptive boosting [80]. A schematic of an AdaBoost classifier is shown in Figure 5.2 for m number of decision tress. The basic procedure Once a single classifier h_m is trained on data sample $\mathcal{D}_m(\mathbf{x})$, the misclassified events are identified and the error rate is calculated:

$$err_m(h) = \frac{\sum_{i=1}^{N} w_i \times \delta(y_i \neq h_m(x_i))}{\sum_{i=1}^{N} w_i}, \tag{5.2.1}$$

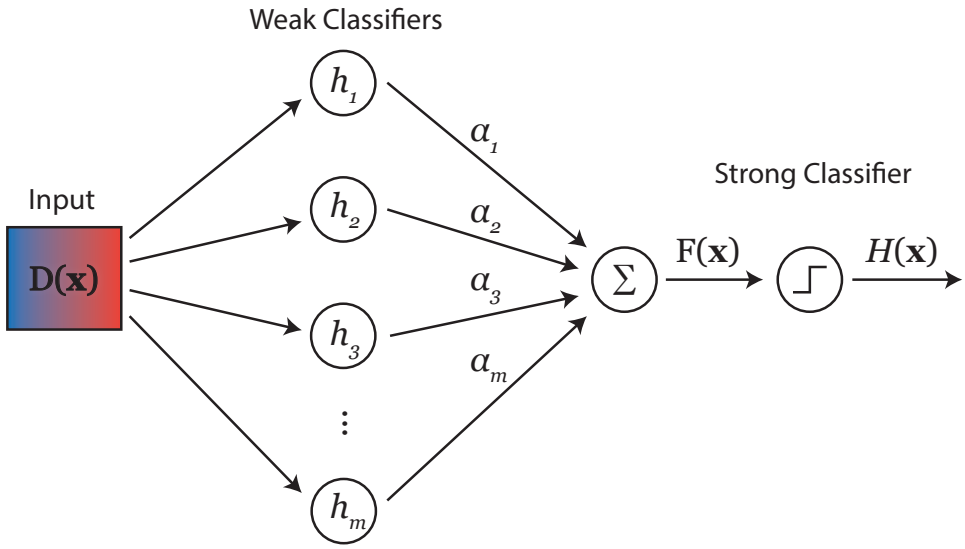

Figure 5.2: Schematic of a Boosted Decision Tree using AdaBoost

where w_i is the weight of the i^{th} event of N total events, and $\delta(y_i \neq h_m(x_i))$ is the test function for comparing the known class (signal $+1$ or background -1) to classifier designation, which results in a binary value. The boost weight assigned to tree m is based on the error rate, given by

$$\alpha_m = \beta \cdot \ln\left(\frac{1-\varepsilon_m}{\varepsilon_m}\right), \tag{5.2.2}$$

where β is the boosting parameter and controls the *learning rate*. The weight of the events are then updated and increased for misclassified events, modifying $\mathcal{D}_m$ to create $\mathcal{D}_{m+1}$:

$$w_i^m \to w_i^{m+1} = w_i^m \times e^{\alpha_m \times \delta(y_i \neq h_m(x_i))}. \tag{5.2.3}$$

One should note, the weights for the initial tree events are uniformly distributed as $1/N$, and the event weights of the subsequent trees are determined from the equations above. Proceeding on, the decision tree h_{m+1} is trained on $\mathcal{D}_{m+1}$, and this boosting procedure continues until the maximum number of the trees is created.

The final boosted decision tree is

$$F(\mathbf{x}) = \sum_{m=1}^{M} \alpha_m \cdot T_m(\mathbf{x}), \tag{5.2.4}$$

summing over all decisions trees and providing a real number response ranging from[2] -1 to 1. For a binary response, $H(\mathbf{x}) = \text{sign}[F(\mathbf{x})]$, will classify all negative values as background and positive ones as signal. However, we use the equation 5.2.4 in this study to have additional control on misclassified events.

There are various BDT parameters that may be *tuned* to achieve optimal classification, including the maximum depth of the a single decision tree, boosting rate β, the maximum number of trees, and the minimum size (number of events) of the a terminal node. The criterion of the optimal boosted classification tree has been studied extensively and its application will be presented in the following chapters employing the Toolkit for Multivariate Data Analysis (TMVA) [81] within the ROOT framework.

[2]Magnitude may vary depending on application, though will always be symmetric.

Chapter 6

Proton–Electron Discrimination in CALET

In the following study, I examine the proton – electron separation capabilities of the CALET instrument employing a multivariate technique introduced in the chapter 5. I will concentrate on two observed energy intervals, 100 - 1000 GeV and 1 -10 TeV, where a distinct classifier was development for each energy region. In section 6.1, an overview of the Monte Carlo simulation and event selection used for this analysis is presented. The discriminating variables developed to characterize electromagnetic particles and their showers is discussed in section 6.2. Section 6.3 demonstrates standard analysis techniques to measure the effectiveness of the MVA application. A detailed analysis and results using a boosted decision tree classifiers are presented in section 6.4. Finally, I will discuss the errors associated with such techniques and the significance of this investigation in section 6.5.

MC True Energy	Electron events	proton events
100 - 1000 GeV	4,000,256	39,503,313
1 - 10 TeV	4,000,256	4,000,256
10 - 30 TeV	948,223	
10 - 100 TeV		2,600,272
100 - 1000 TeV		100,352
Event Type	23,128	85,420
HET	22,697	28,021

Table 6.1: Monte Carlo simulation: number of generated events in each energy band. Observed energy verses MC true energy is shown in sect. A.1.

6.1 Monte Carlo Simulation

In order to study the performance of the detector at conditions beyond terrestrial laboratories potential, a detailed simulation must be developed and performed. Monte Carlo (MC) simulations based on the Electron – Photon Induced Cascade Simulator (`EPICS`) framework [82] were carried out using a detailed geometry model of the CALET instrument. The hadronic interactions are generated with `DPMJET-III` model [83] within the simulation. The MC package has been validated with beam test studies performed on the CALET prototype with the same geometry as the flight model [84], any disagreements were within statistical errors of the experimental data. The incident particles generated, electrons and protons, originate isotropically on a partial sphere ($\theta_z \leq 110°$) encompassing the detector to simulate observations in space. Table 6.1 displays the total number of events generated in the simulation over each energy bin simulated for the respective particle type. The spectrum for each energy interval of protons and electrons, follow a simple power distribution of $dN/dE \propto E^{-1}$, this ensure that a sufficient number of events at high energies is attained for analysis.

As not all of the generated particles will fully interact will the detector, further preselection criteria are applied to the proton and electron samples. We consider practical event types that would result in high quality events (see section A.2 for detailed description). These event types require particles that traverse the detector, at a minimum, have a trajectory passing through the 4^{th} layer of the IMC and a path length in the TASC of $27X_0$. This allows for electromagnetic showers to be completely contained in the fiducial volume of the calorimeter, for energies up to 10 TeV. The resulting number of events that are within event type acceptance are shown above in Table 6.1 each particle species. The final preselection cut applied to the events is the High Energy Trigger (HET), discussed in section 3.3.4, this efficiently eliminates a larger number of background events while maintaining a near pure high energy electromagnetic sample. In this analysis, approximately 67% of protons events are eliminated and over 98% of the electron sample in retained. These remaining events are the focus of the following analysis sections, bisected for development (training) and validation (testing) studies.

6.2 Discriminating Variables

To achieve a high level of separation amongst electron and proton candidates triggered in the calorimeter, it is imperative to have observables that accurately represent the particle shower within the detector. The following variables were developed to aid in the discrimination of electron and proton events using the fundamental concepts introduced in chapter 2, along with standard observables applied within the collaboration. Information provided by each subsystem in CALET is considered, and the respective variables are annotated by the prefix of the observable[1]: *Chd-*

[1]The variable names were selected for consistency within this presented study.

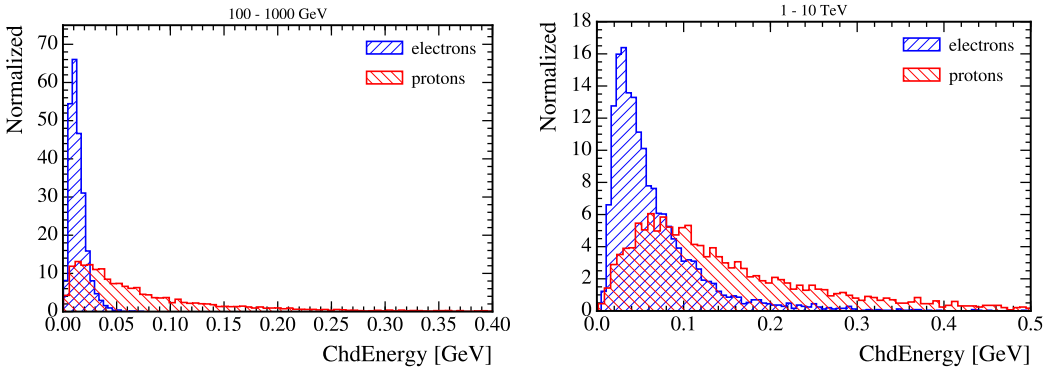

(a) (b)

Figure 6.1: Distribution of ChdEnergy for two energy regions of interest.

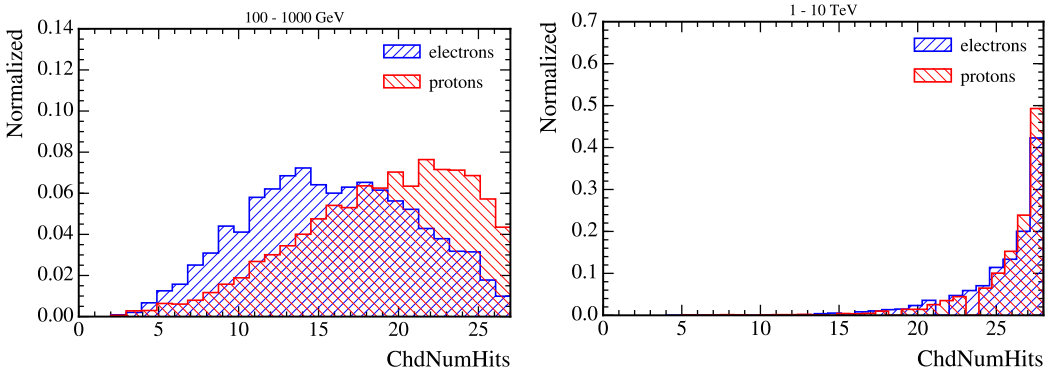

(a) (b)

Figure 6.2: Distribution of ChdNumHits for two energy regions of interest.

for the charge detector, *Imc-* for the imagining calorimeter, and *Tasc-* for the total absorption calorimeter (presented in sect. 3.3). A total 12 discriminating variables are used in this analysis and their respective distribution in the two observed energy intervals, 100−1000 GeV and 1−10 TeV, analyzed in this study are shown.

6.2.1 Variable Description

- **ChdEnergy:** The total energy deposited in the CHD paddles (Fig. 6.1).
- **ChdNumHits:** The total number of CHD paddles that registered a hit (Fig. 6.2).

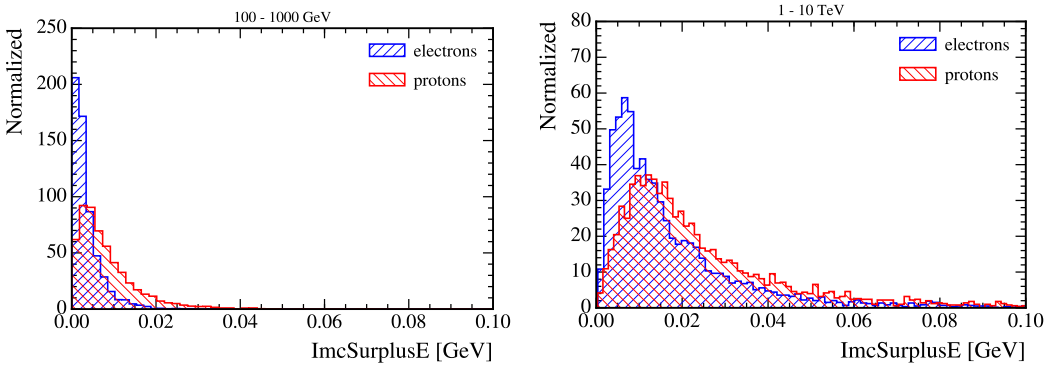

(a) (b)

Figure 6.3: Distribution of ImcSurplusE for two energy regions of interest.

- **ImcSurplusE:** The total energy deposited outside one Moliére radius in the last layer of the IMC (Fig. 6.3). R_M is set to 0.9327 cm (approximately $\pm$ 9 fibers), as the tungsten plates are predominately responsible for inducing interaction as result of the small radiation length of the material.

- **ImcEcoreRatio:** The ratio of the energy deposited in one Moliére radius in the last layer to the total energy deposited in the IMC (Fig. 6.4). R_M is set to 0.9327 cm (approximately $\pm$ 9 fibers), as the tungsten plates are predominately responsible for inducing interaction as result of the small radiation length of the material.

- **ImcHitRatio:** The ratio of the total number of hits in the thin layers to the total number of hits in the thick layers in the IMC (Fig. 6.5). The number of secondary particles of an electromagnetic shower may be analytically describe by $N(t) = 2^t$ in a simple shower model, where $t = x/X_0$ is the traversed depth.

The following two variables derive from the longitudinal shower fit of the energy deposited in the IMC. At small depths, an electromagnetic shower may be described by a parabolic equation:

$$\frac{dE}{dt} = p_0 t^2 + p_1, \tag{6.2.1}$$

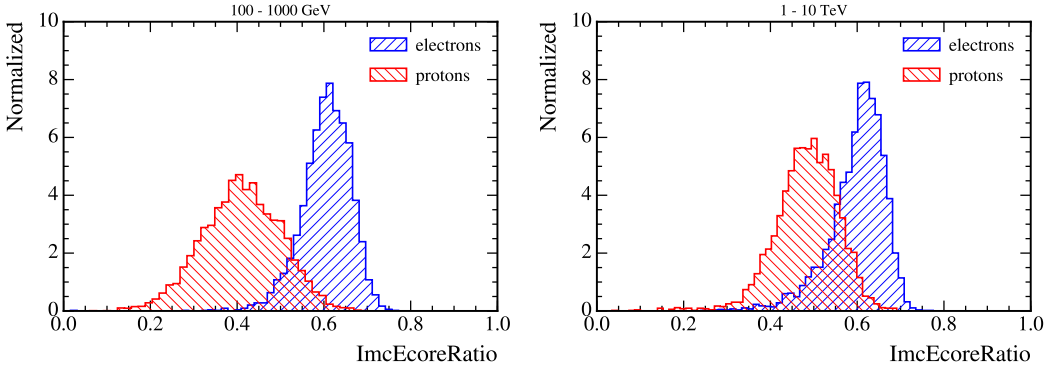

(a) (b)

Figure 6.4: Distribution of ImcEcoreRatio for two energy regions of interest.

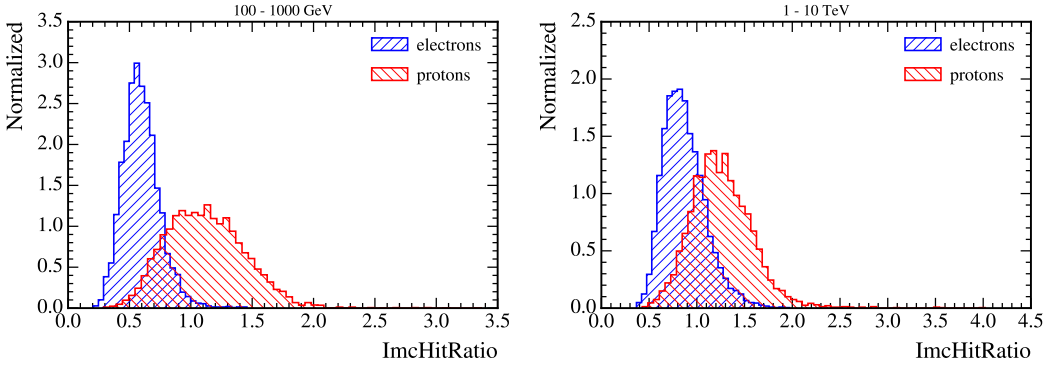

(a) (b)

Figure 6.5: Distribution of ImcHitRatio for two energy regions of interest.

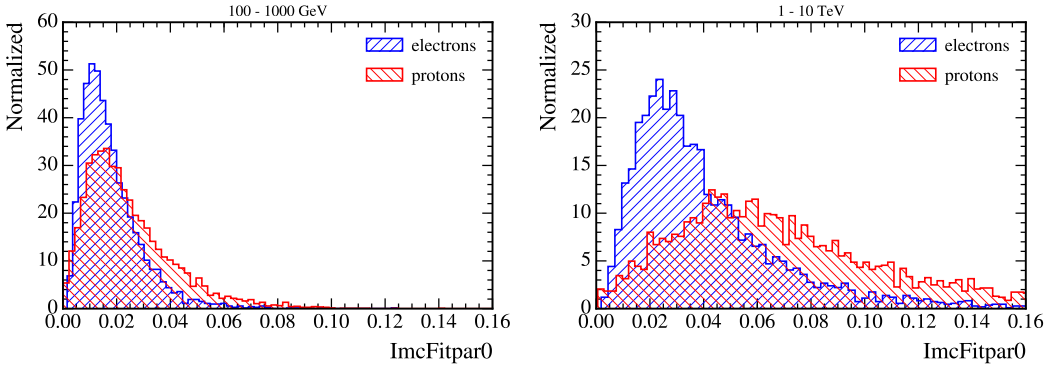

(a) (b)

Figure 6.6: Distribution of ImcFitpar0 for two energy regions of interest.

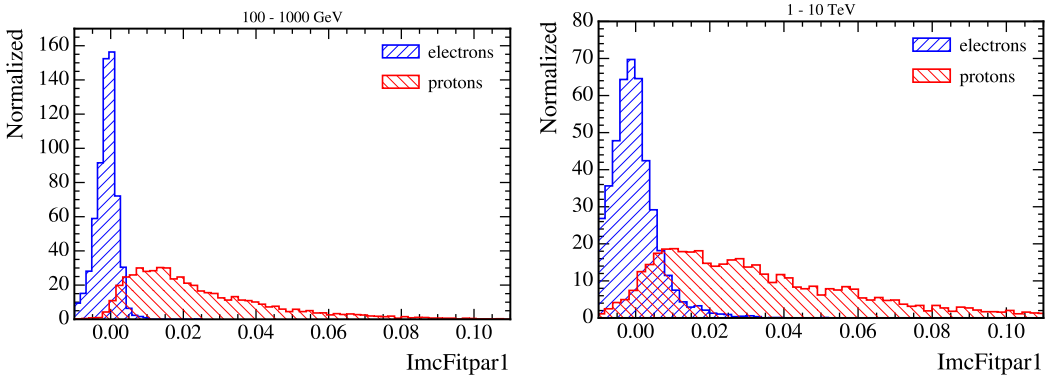

(a) (b)

Figure 6.7: Distribution of ImcFitpar1 for two energy regions of interest.

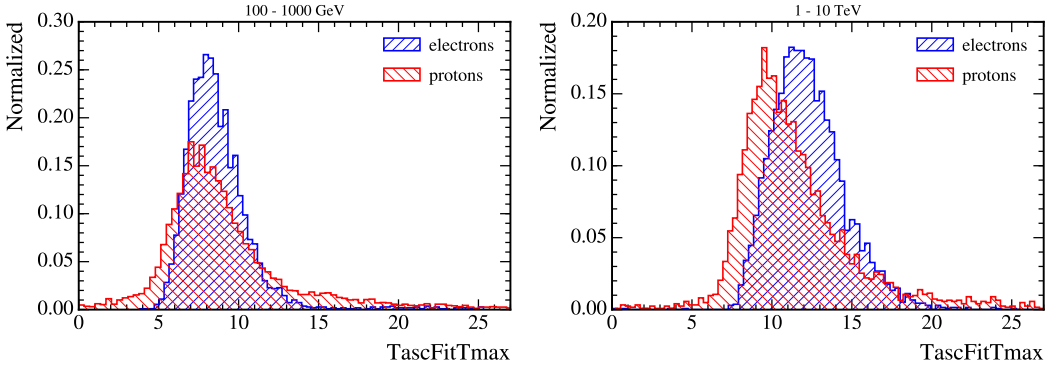

(a) (b)

Figure 6.8: Distribution of TascFitTmax for two energy regions of interest.

where $t = x/X_0$ is the traversed depth.

- **ImcFitpar0:** The parameter p_0 from equation 6.2.1, describing the degree of longitudinal development (Fig. 6.6).
- **ImcFitpar1:** The parameter p_1 from equation 6.2.1, describing the initial energy deposited (Fig. 6.7).

The following two variables derived from the longitudinal shower fit of the energy deposited in the TASC. As described in section 2.4, an electromagnetic shower in a

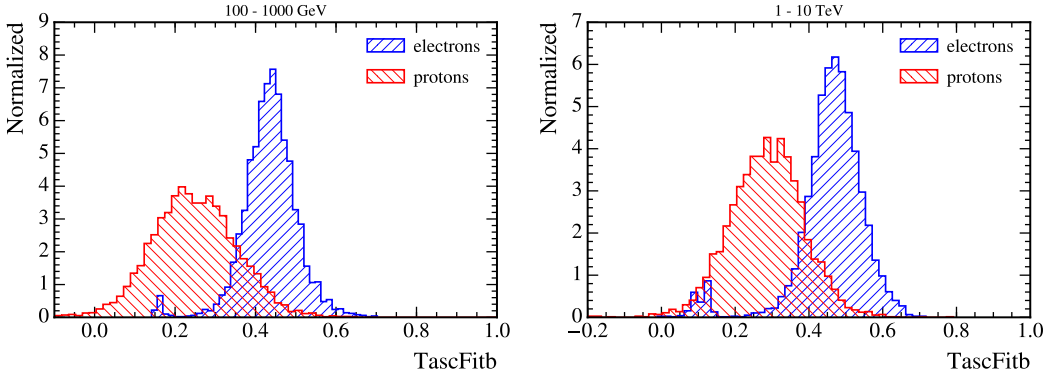

(a) (b)

Figure 6.9: Distribution of TascFitb for two energy regions of interest.

homogenous material may be described by:

$$\frac{dE}{dt} = E_0 b \frac{(bt)^{a-1} e^{-bt}}{\Gamma(a)} \tag{2.4.1}$$

where $t = x/X_0$ is the traversed depth.

- **TascFitTmax:** The location of the shower maximum in the TASC calculated from equation 2.4.1, where $t_{max} = a - 1/b$ (Fig. 6.8).

- **TascFitb:** The parameter b from the equation 2.4.1, describing the decrease of the shower development at large depths (Fig. 6.9).

The subsequent two variables are utilized in the collaboration for constructing the Figure of Merit (FoM), demonstrating the separation capabilities of the instrument. These variables has proven to provide a highest level quantitative description of the longitudinal and lateral shower development in the TASC.

- **TascEWS (R_E):** The energy weighted spread measures the lateral distribution of the shower exploiting the horoscopic arrangement of the TASC crystals

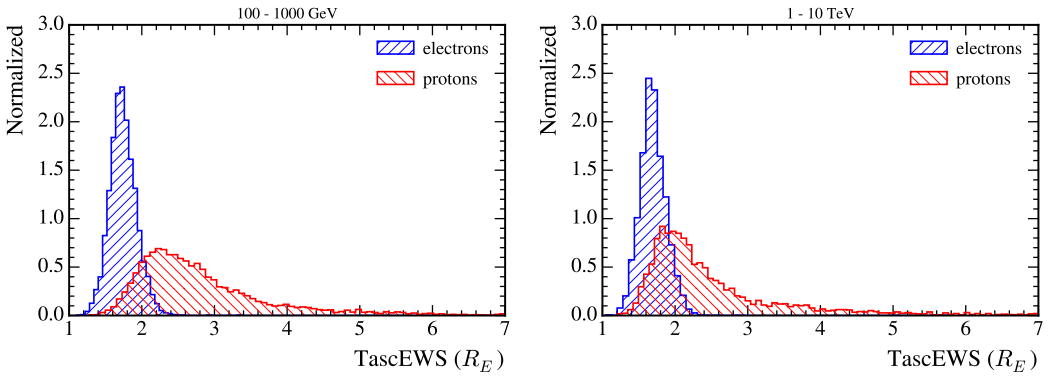

(a) (b)

Figure 6.10: Distribution of TascEWS (R_E) for two energy regions of interest.

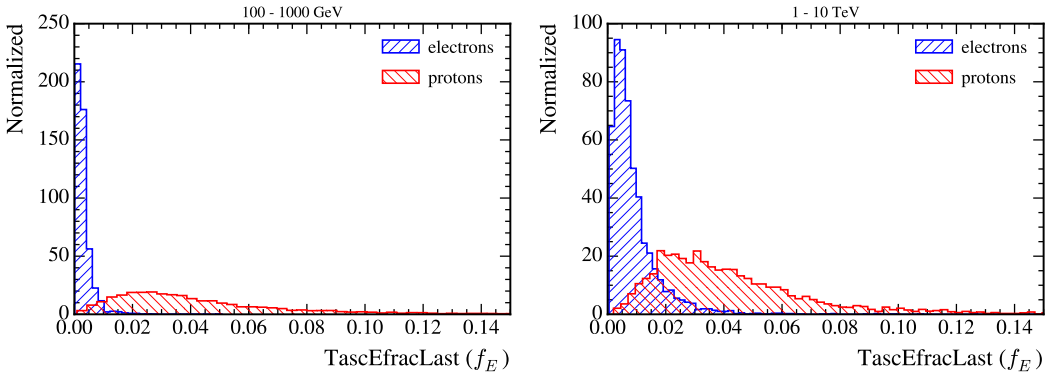

(a) (b)

Figure 6.11: Distribution of TascEfracLast (f_E) for two energy regions of interest.

(Fig. 6.10). Defined as:

$$R_E = \sqrt{\frac{\sum_i (\sum_j \Delta E_{i,j} \times R_i^2)}{\sum_i \sum_j \Delta E_{i,j}}}, \tag{6.2.2}$$

where $\Delta E_{i,j}$ is the energy deposited of the j^{th} crystal of the i^{th} layer. R_i is the root mean square of the spread at the i^{th} layer is expressed as:

$$R_i = \sqrt{\frac{\sum_j (\Delta E_{i,j} \times (x_{i,j} - x_{i,c})^2)}{\sum_j \Delta E_{i,j}}},$$

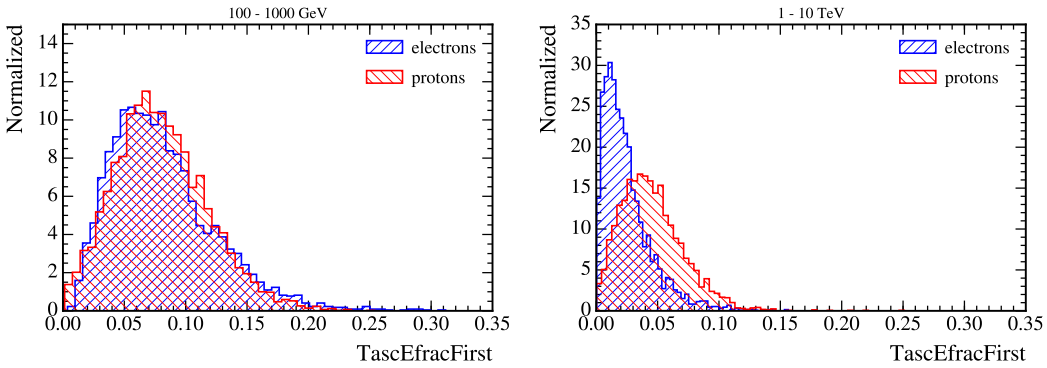

(a) (b)

Figure 6.12: Distribution of TascEfracFirst for two energy regions of interest.

where $x_{i,j} - x_{i,c}$ is the distance from the center of the j^{th} crystal in the i^{th} layer to the intercept of the particle shower axis with the i^{th} layer.

- **TascEfracLast (f_E):** The fractional energy deposited in the last hit layer, where the incident particle shower axis exits, relative to the total energy deposited in the TASC (Fig. 6.11).

- **TascEfracFirst:** The fractional energy deposited in the first hit layer relative to the total energy deposited in the TASC (Fig. 6.11).

6.2.2 Variable Correlation

As many of the above variables describe the same physical quantities employing varied definitions, one would expect that some discriminating variables will be correlated. The linear correlation matrix of the variables is shown in Figure 6.13. As a result to the limit of information that may be extracted from the subsystems regarding the particle showers in the detector, correlation between CHD and IMC variables are higher than that of the TASC. While this does not diminish the discriminating capabilities of the observables, as the values will vary in different energy bands, this can allow for optimization of the BDTs. The performance of the BDT classifier will

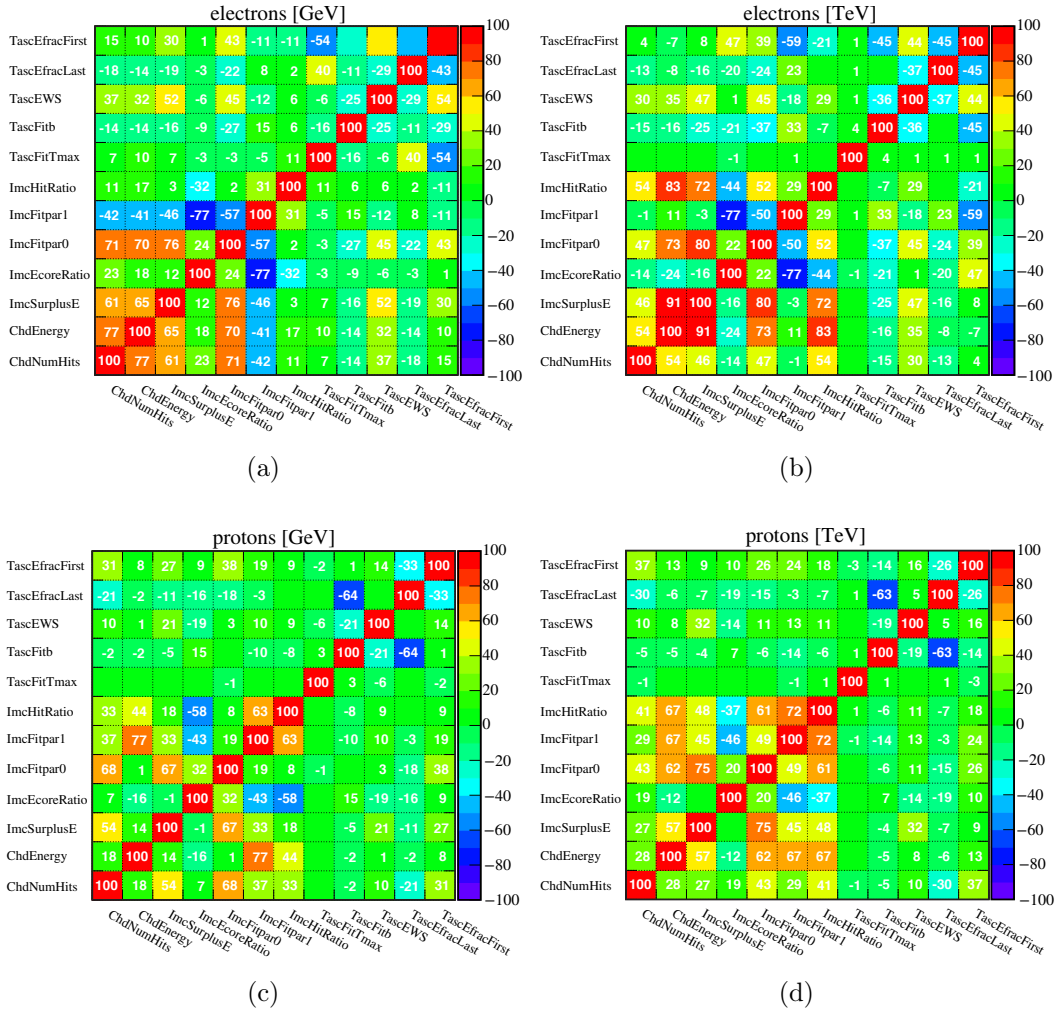

Figure 6.13: Correlation matrix of discriminating variable in the GeV and TeV energy ranges.

not be affected by including highly correlated variables, however, the training time may be decreased by reducing the number of the input parameters. All discussed discriminating variables in this section are included in the development of the BDTs for consistency with standard analysis comparisons.

6.3 Standard Analysis

A straightforward and more transparent method of analysis, known simply as *rectangle cuts*, is historically the standard (or traditional) approach to select events of interest (i.e. signal) against a background of events. The event selection commonly proceeds in stages of individual cuts on relevant observables to reach maximum purity without severely altering the overall distribution of the signal. There are limitations to this approach, as the process of executing cuts may be arbitrary and the cuts may have not utilize all information available in regards to the events. Additionally, rectangular cuts do not generally take into account *hidden* correlation amongst variables to fully exploit possible discriminating aspects and optimize event selection. Below demonstrates this approach on the test samples of the electron and proton data for later comparison to that of the multivariate analysis. Following the simple guideline to standard analysis, *cut hard and fast*, I examine this method in the two observe energy ranges of our data.

6.3.1 GeV Analysis

The following analysis is on the observed energy range of 100 - 1000 GeV for electrons and protons, with an objective of selecting a high purity sample of electrons while maintaining a high signal efficiency. The consecutive set of cuts are as follows:

`Cut 1:` $f_E < 0.3R_E^{-7.436}$

`Cut 2:` ImcEcoreRatio > 0.425

`Cut 3:` ImcHitRatio < 1.1

`Cut 4:` ImcFitpar1 < 0.007

As presented in [67], the correlation between f_E and R_E provides the most significant selection of electrons from protons due to their different shower topology in the

No.	Cut	electrons	protons
Initial Sample		3562	6661
1	$f_E < 0.3 R_E^{-7.436}$	3087	35
2	ImcEcoreRatio >0.425	3076	28
3	ImcHitRatio <1.1	3058	25
4	ImcFitpar1 <0.007	3047	22
$efficiency$		0.86	0.0033

Table 6.2: Standard Analysis in the 100 GeV - 1000 GeV energy range.

TASC (see Figure 6.14a). Cut 1 was chosen as the optimal location within the sample, allowing for the exclusion of more than 99.4% of the proton sample while retaining $\sim$ 87% of the signal. Cuts 2 – 4 are responsible for selecting electrons according to their *preshower* development in the IMC, shown in Figures 6.14b – 6.14d. Additional cuts could not be applied without severely reducing the efficiently of the electron data. The final result after applying the above cuts is an $\sim$ 86% signal efficiency while the proton efficiency is $\sim$ 0.33% in the test sample. The product of the respective cuts are summarized in the Table 6.2.

6.3.2 TeV Analysis

The following analysis is on the observed energy range of 1 - 10 TeV electrons and protons, with an objective of selecting a high purity sample of electrons while maintaining a high signal efficiency. The consecutive set of cuts are as follows:

`Cut 1:` $f_E < 0.5 R_E^{-7.194}$

`Cut 2:` ImcEcoreRatio > 0.465

`Cut 3:` ChdEnergy < 0.32 GeV

`Cut 4:` ImcFitpar1 < 0.0175

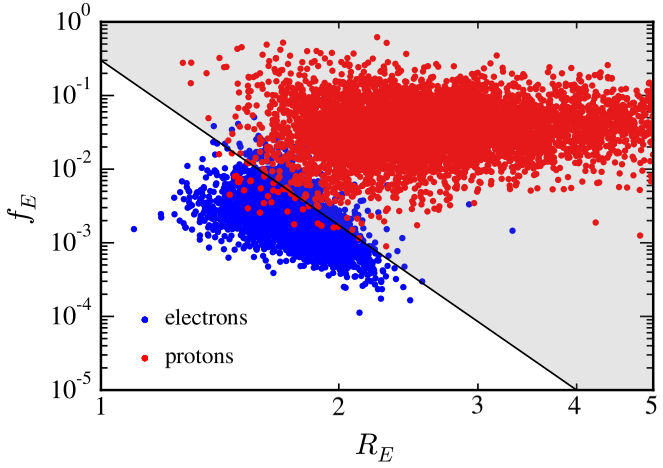

(a) Cut 1

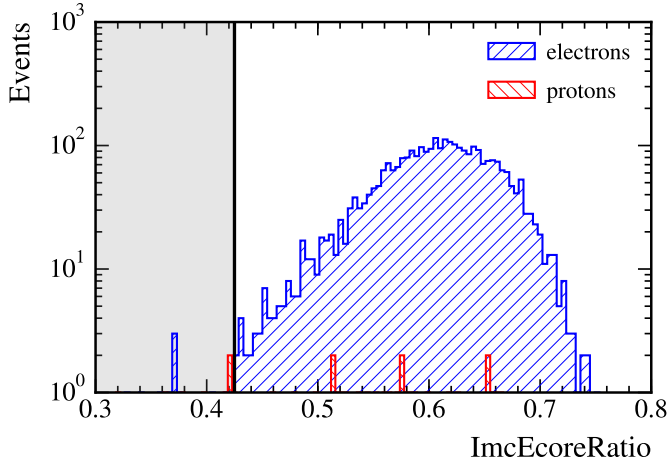

(b) Cut 2

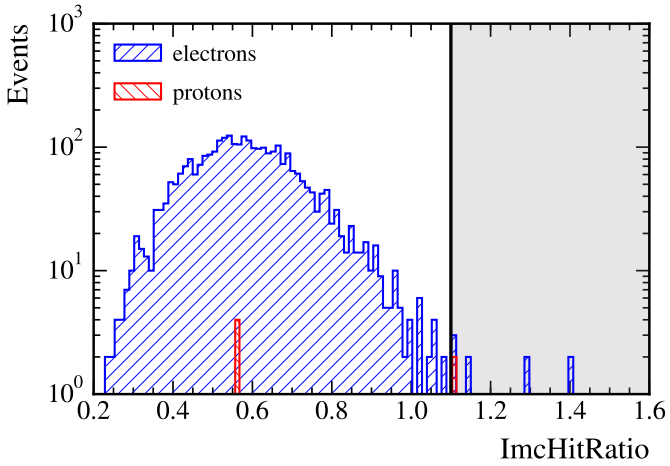

(c) Cut 3

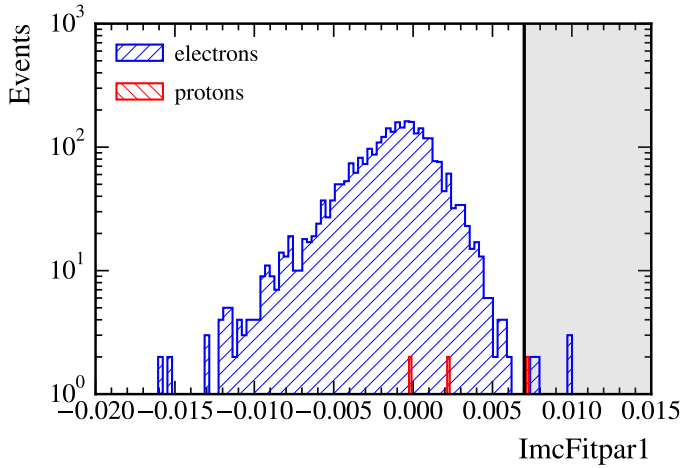

(d) Cut 4

Figure 6.14: Standard analysis cuts applied to distributions in 100 – 1000 GeV energy range.

No.	Cut	electrons	protons
Initial Sample		4252	4022
1	$f_E < 0.5R_E^{-7.194}$	3344	103
2	ImcEcoreRatio > 0.465	3266	87
3	ChdEnergy < 0.32 GeV	3249	79
4	ImcFitpar1 < 0.0175	3237	65
$efficiency$		0.76	0.01616

Table 6.3: Standard Analysis cuts in 1 - 10 TeV energy range.

As in the GeV analysis, the correlation between f_E and R_E provides the most significant selection of electrons from protons due to their different shower topology in the TASC (see Figure 6.15a). Cut 1 was chosen as the optimal location within the sample, allowing for the exclusion of more than 97.4% of the proton sample while retaining $\sim$ 79% of the signal. Cuts 2 – 4 are responsible for selecting elections according to their preshower development in the IMC and their interaction in the CHD [85], shown in Figures 6.15b – 6.15d. Additional cuts could not be applied without severely reducing the efficiently of the electron data. The final result after applying the above cuts is an $\sim$ 76% signal efficiency while the proton efficiency is $\sim$ 0.16%. The response of the cuts are summarized in the Table 6.3.

6.4 Multivariate Analysis

As the development of the Boosted Decisions Trees are commonly achieved in two phases: training and testing, the Monte Carlo data sets are distributed equally for each phase. The training and testing data sets exhibit similar characteristics in the count per energy bin, and the power law spectrum for each particle type. The objective of the development stage is construct a classifier that adequately generalizes your training data for a predictive model for future observations without *overtraining*, or creating bias in the classifier due to statistical fluctuations in the

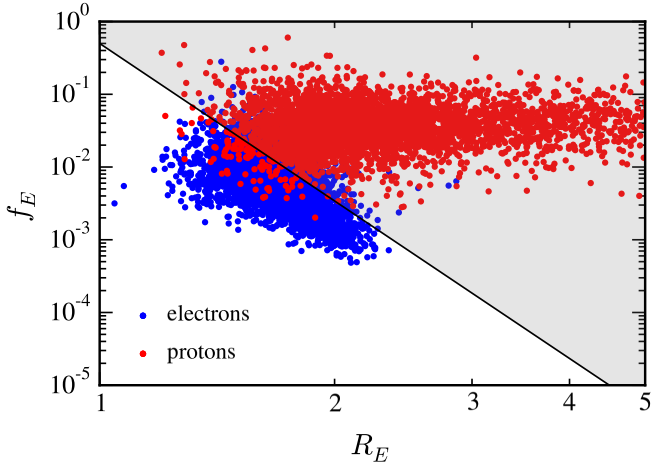

(a) Cut 1

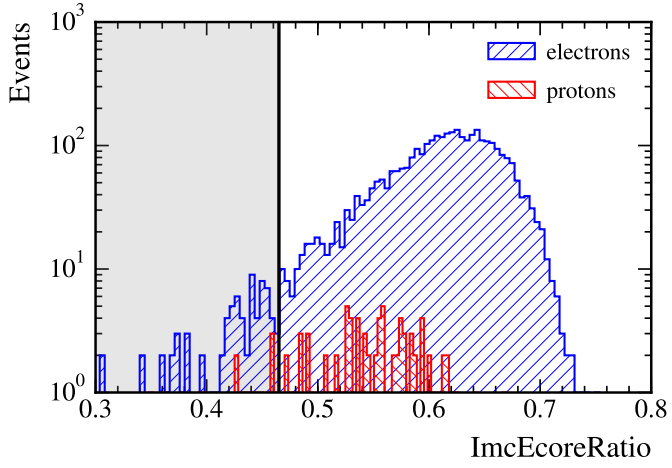

(b) Cut 2

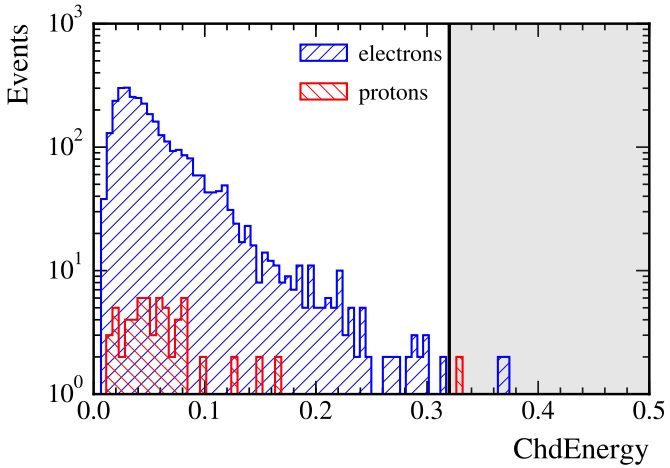

(c) Cut 3

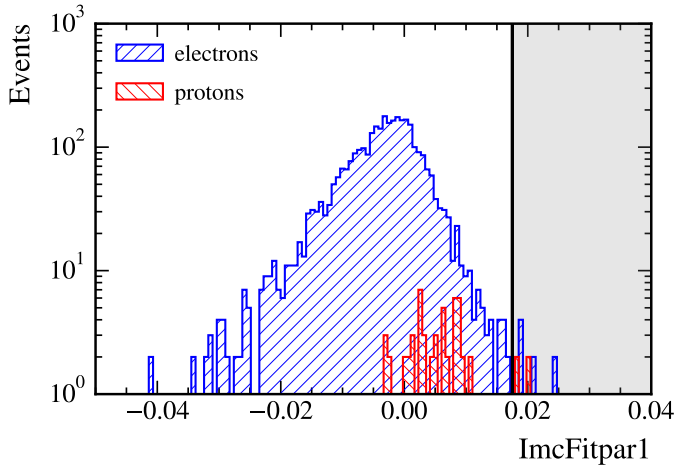

(d) Cut 4

Figure 6.15: Standard analysis cuts applied to distributions in 1 - 10 TeV energy range.

Parameters	GeV	TeV
Number of Trees	650	450
AdaBoost β	0.4	0.6
Minimum Node Size	2.5%	2.5%
Tree Maximum Depth	3	3

Table 6.4: Tuning parameters of each BDT classifier developed.

training data set. One should note, the development of the multivariate methods are usually constructed with three independent data samples for training, validation, and testing. The first two samples will display some bias as result of adapting the classifier to the validation sample, and the third would allow for an independent review. However, physics based experiments rarely follow this paradigm, as this results in sacrificing a large portion of the simulation data.

6.4.1 Training of the Boosted Decision Trees

As previously mentioned, the analysis is conducted over two energy intervals of 100 – 1000 GeV and 1 – 10 TeV; each BDT will be referred to as GeV and TeV classifier considering their respective energy emphasis. The parameters of the two BDTs developed are outlined in Table 6.4 and the *tuning* parameters were chosen through an iterative process to find the classifier with optimal performance for each training set as applied to the testing sample. An actual decision tree for the GeV classifier is shown in Figure 6.16 for an illustrative view, one of the 650 decisions trees that composes the forest of the BDT applied in this analysis. The response of the developed BDTs are shown in Figures 6.17, projecting the outputs of the classifier for the training sample on the testing sample of the GeV ($left$) and TeV ($right$) classifiers. The performance of the classifiers provide considerable power in the identification of electrons from protons. The discrepancies in the distributions of the training and

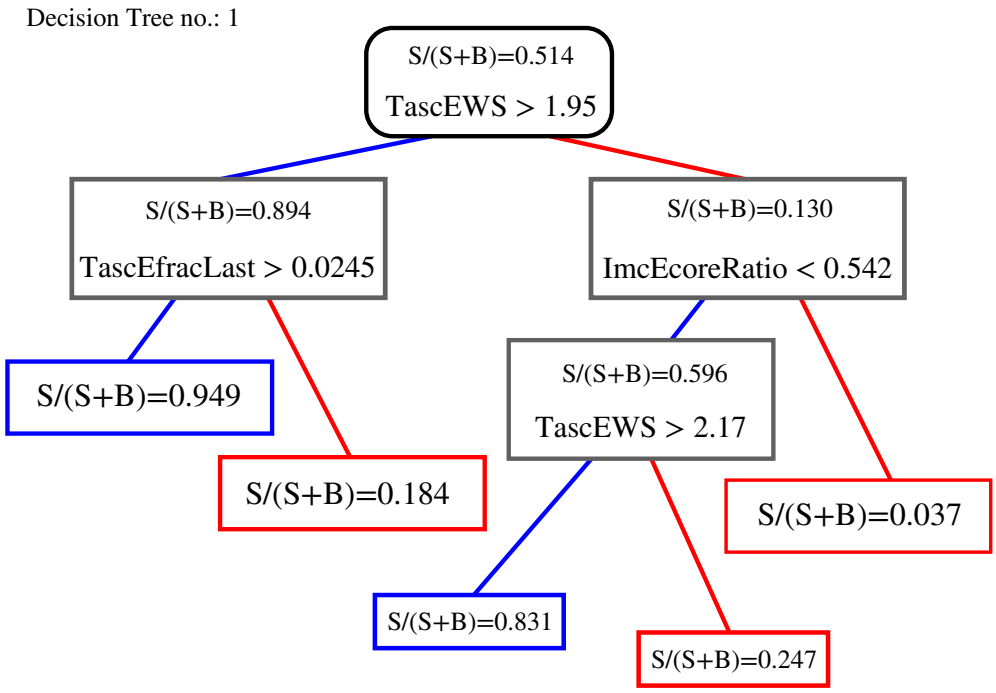

Figure 6.16: One of the decision trees from the boosted decision tree forest that was used in this analysis in the GeV observed energy range. The variable and cut value used at each branching node is shown, along with the individual node purity $P = S/(S + B)$. The weighted number of true signal and background events are S and B, respectively. The blue/red color nodes represent terminal nodes of signal-like and background-like classified events.

testing samples may be attributed to some overtraining, however, this has very little influence on the overall classification. Employing the Kolmogorov–Smirnov (K–S) test [86] on the two sets, the statistical probability that two samples are drawn from the same distribution is: 0.756 (0.814) for the signal (background) sample in the GeV classifier and 0.201 (0.246) for the signal (background) sample in the TeV classifier. The differences in K–S values arise from difficulties in optimization of the two classifier, where higher energy particle shower discrimination is more challenging. These values are more than acceptable and suggest minimal bias relating to overtraining, in principal, a K–S value > 0.05 is sufficient.

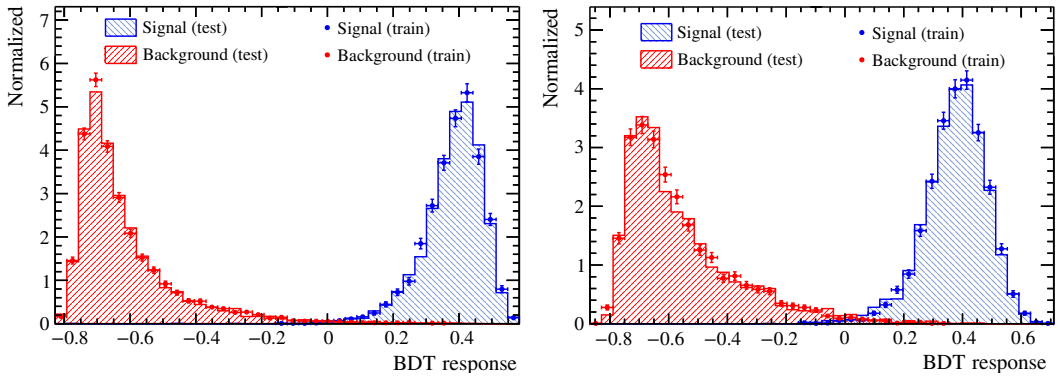

(a) 100 - 1000 GeV Classifier.

(b) 1 - 10 TeV Classifier.

Figure 6.17: BDT Classifier output of the training and test samples.

6.4.2 Final Cut on the Boosted Decision Trees

There are several measures in determining the optimal cut location on the response of a classification tree and this is dependent on the desired conclusion. As in the standard analysis approach, we are concern with a high purity signal sample while maintaining a high signal efficiency. To establish the cut location on the BDT output of the training sample, I examine the the the statistical significance, defined as $S/\sqrt{S+B}$, where is the S is the signal efficiency and B is the background efficiency. While minimizing the background contamination without forfeiting considerable amount of signal, the final cut locations to applied on the testing data sets are chosen to be: BDT response $>$ 0.28 on the GeV classifier and BDT response $>$ 0.25 on the TeV classifier. The significance, electron, and proton efficiencies are shown in Figure 6.18, with the cut locations superimposed. The resulting signal efficiency of of the GeV and TeV classifier is 87.8% and 89.6%, with 0.09% and 0.15% background efficiency on the training samples.

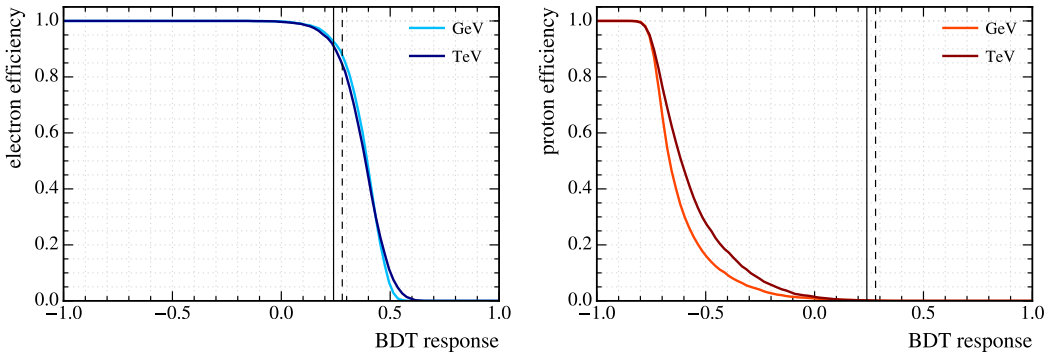

(a)

(b)

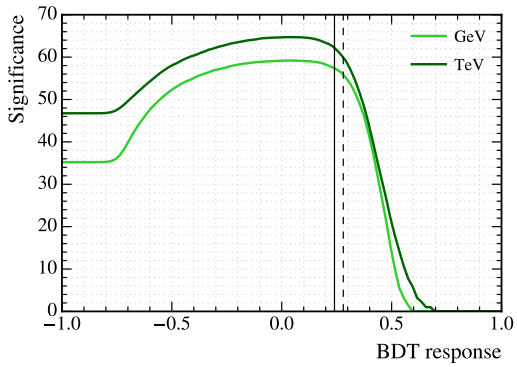

(c)

Figure 6.18: The (a) signal efficiency, (b) background efficiency, and (c) significance of the training sample against the BDT response of the GeV and TeV classifiers. The *dash* black line indicates the cut location of 0.28 of the GeV BDT and the *solid* black line indicates the cut location of 0.25 on the TeV BDT.

6.4.3 Monte Carlo Results

The results of the BDT classifiers as applied to the testing samples are shown in Figures 6.19a and 6.19b, as function of observed energy. This allows us to examine the stability of classifiers over the respective energy intervals, which very important considering observations of CALET will conducted over such a large energy range. The final cut value for each BDT is shown, where all events above the grey area of the distributions are to identified as the electron candidates. Both BDTs exhibit approximately energy independent responses to electrons events. There is slight de-

BDT	GeV		TeV	
	electrons	protons	electrons	protons
Initial Sample	3562	6661	4252	4022
BDT cut	3104	12	3770	15
efficiency	0.8714	0.0018	0.8866	0.0037
Standard Difference	+1.6%	+0.15%	+12.53%	+1.24

Table 6.5: BDT results with comparison of standard analysis.

viation of the proton events, shifting towards the electron candidate region. This can be expected as high energy protons losing energy through electromagnetic showers will emulate electron events and become increasling difficult to discriminate. The classification results are additionally compared with the Monte Carlo truth energy Figures 6.19c and 6.19d to demonstrate the nature of interacting protons contaminating the lower energy bins of observations. The small proton sample at energies above 4 TeV can be attributed to energy leakage of the calorimeter for hadronic events.

The resulting signal and background efficiencies are presented in Table 6.5. Electron identification employing BDTs showed a slight increase in signal efficiency and background reduction from the standard analysis in the 100 – 1000 GeV observed energy range. In the 1–10 TeV range, the BDT classification approach substantially improved the signal efficiency while notably reducing the contamination of protons events.

6.4.4 Energy Dependent Results

The method shown in the previous sections is know as applying *hard* cuts, and does presents some limitations. As seen in Figure 6.19a and 6.19b, introducing energy dependent selection could substantially benefit the overall signal efficiency,

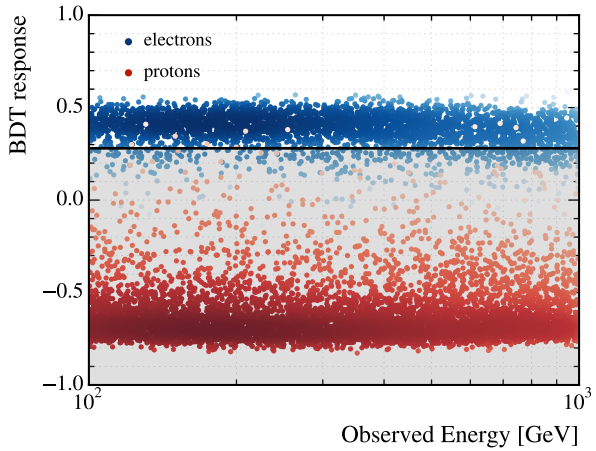

(a) 100 - 1000 GeV Classifier.

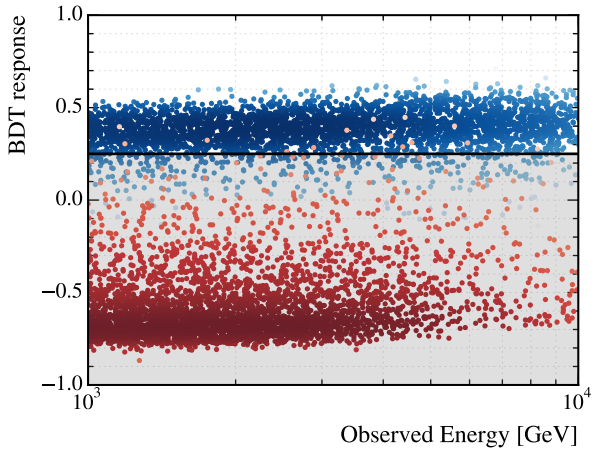

(b) 1 - 10 TeV Classifier.

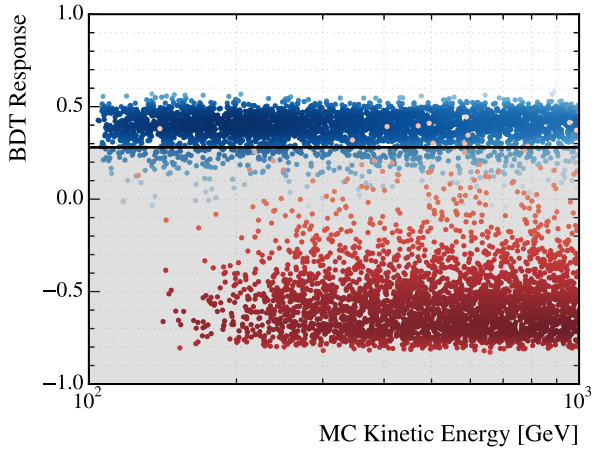

(c) 100 - 1000 GeV Classifier.

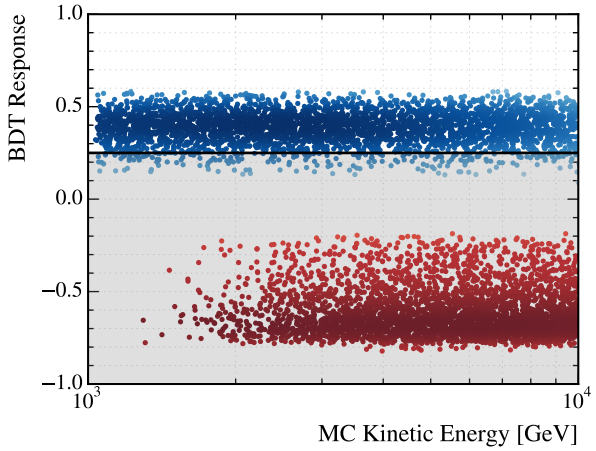

(d) 1 - 10 TeV Classifier.

Figure 6.19: BDT Classifier output of the testing samples compared with energy.

especially in the energy regions below and above 1 TeV. Using the derived hard cuts for the GeV and TeV classifiers as baseline, I employ the optimal dynamic cuts on the samples to increase the efficiency of signal without selecting an abundance of true background events. Each of samples in the 100 – 1000 GeV and 1 TeV - 10 TeV are divided into 9 equal *log-space* width energy bins. The GeV *loose* cuts start at the original hard cut value of 0.28 and decreases with a gradient of -0.10 with the log of observed energy. The TeV *loose* cuts ends near the original hard cut value of 0.25, increasing with a gradient of 0.10 with the log of observed energy for 0.155. The loose and hard cuts are shown in Figure 6.20 for the GeV and TeV classifiers.

The results of introducing the energy dependent cuts is shown in Table 6.6, per energy bin, as compared with the hard cuts. As one would expect, an increase in background efficiency is a product of applying looser cuts, migrating to lower BDT values. This affect is very modest as compared to the increase in signal with an overall efficiency of $\sim$ 94%. Figure 6.21 displays the signal efficiencies of the two cuts, where the *loose* cuts exhibit a more stable behavior over the entire energy range. Notably, in the crucial energy range of $\sim$ 400 GeV – 4 TeV where the two classifiers adjoin, a large increase in signal efficiency and stability is shown. For further characterization, a common parameter used in astroparticle physics is the *rejection power* of background, defined as

$$\mathcal{R} = \frac{\varepsilon_{sig}}{\varepsilon_{bkg}}, \tag{6.4.1}$$

where ε_{bkg} is the proton efficiency and ε_{sig} is the electron efficiency of the total number of the respective particle type within the Monte Carlo acceptance in the energy range. By applying the energy dependent and independent BDT cuts, the total rejection powers achieved are $\sim$ 2.0 $\times$ 10^3 and $\sim$ 2.8 $\times$ 10^3, respectively.

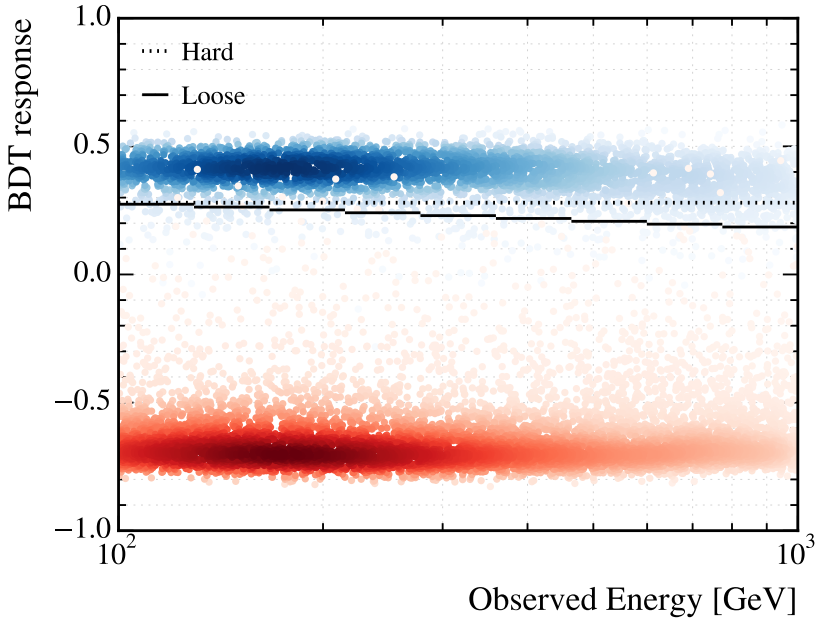

(a) 100 - 1000 GeV Classifier.

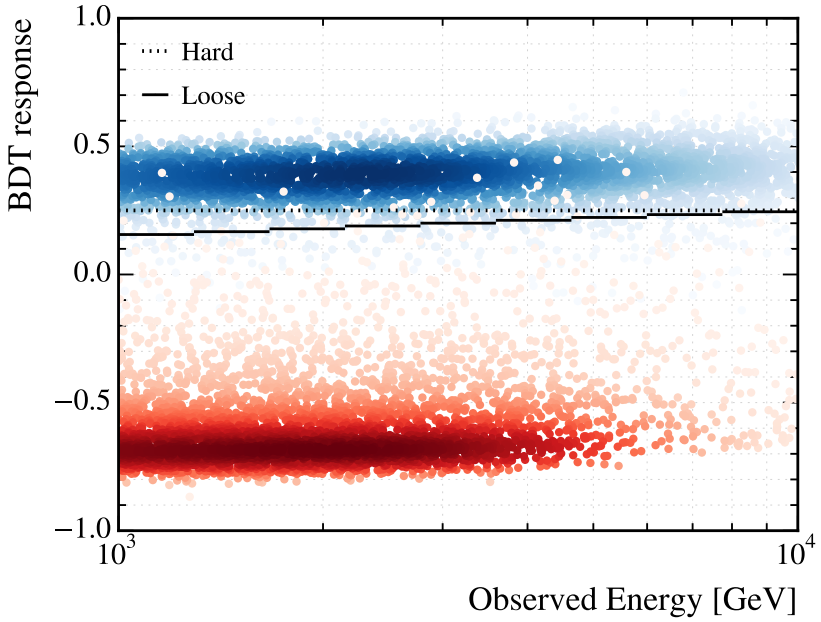

(b) 1 - 10 TeV Classifier.

Figure 6.20: BDT Classifier output of the testing samples compared as a function of energy, superimposed with hard and loose cuts. The opacity of the distributions were decreased to show *hard* and *loose* cuts applied. Blue represents *true* electrons and red represents *true* protons.

Energy (GeV)	ε_{sig} (Loose)	ε_{sig} (Hard)	$\Delta\varepsilon_{bkg}$
100 - 129.2	0.888	0.888	0.0
129.2 - 166.8	0.919	0.902	+0.0024
166.8 - 215.4	0.961	0.943	0.0
215.4 - 278.3	0.941	0.903	+0.0051
278.3 - 359.4	0.920	0.865	0.0
359.4 - 464.2	0.952	0.896	0.0
464.2 - 599.5	0.959	0.868	+0.0025
599.5 - 774.3	0.945	0.801	0.0
774.3 - 1000	0.942	0.775	0.0
1000 - 1291.5	0.940	0.867	+0.0049
1291.5 - 1668.1	0.938	0.866	0.0
1668.1 - 2154.4	0.961	0.888	+0.0024
2154.4 - 2782.6	0.966	0.917	+0.0024
2782.6 - 3593.8	0.945	0.889	+0.0048
3593.8 - 4641.6	0.947	0.915	+0.0133
4641.6 - 5994.8	0.925	0.902	+0.0052
5994.8 - 7742.6	0.932	0.914	0.0
7742.6 - 10000	0.919	0.910	+0.0030

Table 6.6: Signal efficiency of *loose* and *hard* cuts applied per energy bin with the difference in background efficiency.

These values are both within range of current experiments rejection power and are sufficient for observing cosmic ray electrons, as discussed in section 1.4.1. One should note, other authors have reported much higher rejection powers ($\mathcal{R} \sim 10^5$) in the literature; however, this discrepancy is a result of varied definition within the field and calculations with a much smaller energy bins. In considering the same energy interval of 912–1000 GeV examined in [85], a rejection power of 7.8×10^4 is achieved with energy dependent selections, consistent with previous studies.

6.5 Conclusion

This chapter demonstrated the advantages of employing multivariate analysis techniques to that of standard analysis approaches. The systematics uncertainties

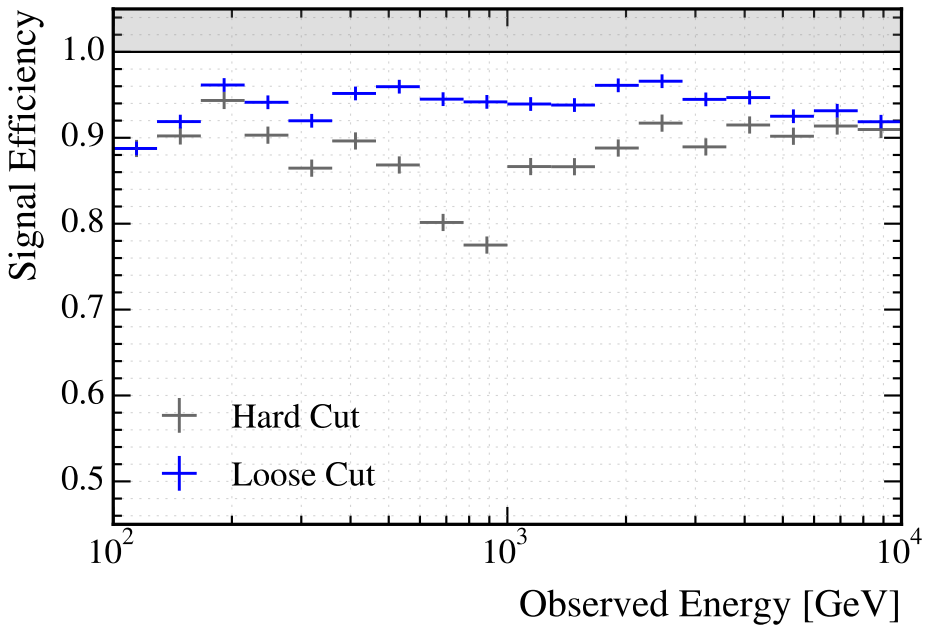

Figure 6.21: Signal efficiency of the GeV and TeV classifiers applied with energy independent (hard) and dependent (loose) cuts as a function of energy.

of such methods is often hard to characterize, as there is complete control of the development process of the classifiers, though reducing the testing data sample bias is paramount. Classification ensembles are commonly cross validated by examining the error associated with different configurations of training events. Using 10-$fold$ cross validation procedure, I found the average error in signal efficiency with identical cuts was $\sim$3%. This still allows for signal efficiencies of more than 90% on average, with little background contamination. In addition to hadrons, gamma–rays may also contaminate the electron signal; however, a study has shown that CALET is able to separate 10^4 electrons for every incident γ–ray employing the observed signals solely from the CHD [87]. Although not presented here, energy dependent standard cut may also be applied, however, this is much more time consuming than reducing the dimensionality to one variable (i.e. BDT response). This work is the first of its kind, examining nearly the entire observable energy range of CALET. As the mission has

just begun, this work is still preliminary and the implementation such techniques in the future analysis of flight data will be preformed in order to provide a greater discriminating power of electrons from the vast proton background.

Chapter 7

Electron Identification in the Fermi LAT Tracker

In this chapter, I present my efforts in the development of a particle identification algorithm using dedicated information from the tracking region of the Fermi LAT detector. I employ a multivariate technique introduced in the chapter 5 to aid in the identification of non-interacting protons, electromagnetic and hadronic *preshowers*. I begin in section 7.1, providing an overview of the motivation and strategy I have taken for this analysis. Section 7.2 describes the background of the calibration data collected during the beam test campaigns and the LAT prototype detector used in the calibration studies. In section 7.3, I will discuss the beam test analysis of the calibration unit with emphasis on measurements in the tracker. The results of employing a boosted decision tree classifier is presented in section 7.5. Less focus will be on the classifier itself as in the Fermi Analysis, classification trees are standard practice. Finally, I will review the results and discuss the outlook of the analysis moving forward in the section 7.6.

7.1 Analysis Approach

The LAT electron analysis results as seen in the literature has relied on high level variables used for the study of energetic gamma–rays, and may have not taken full advantage of the particle identification capabilities of the tracker. The high energy electron selection depends on the ability of LAT to distinguish electromagnetic (EM) showers from hadronic showers, employing information from both the tracker and calorimeter subsystems [88]. Although gamma rays produce EM showers through pair production, electron cascades are fundamentally different as mentioned in Chapter 2. The *preshower* detected in the tracker may provide additional information beyond the characterization of the photon analysis and allow for further discrimination of electrons from the hadronic background. Measurements of the lateral distribution of the particle shower provides valuable information in distinguishing between non-interacting hadrons, electromagnetic cascades and hadronic showers. I have developed a new set of discriminating variables for analyzing the event topology in the tracker describing the particle *preshower* laterally and longitudinally of the traversing particle, and will be discussed further in the section 7.4. This method has been studied employing Monte Carlo simulations, and this chapter demonstrates the capability on beam test data.

7.2 Beam Test Campaign

A series of beam test campaigns were conducted at the SLAC, CERN, and GSI accelerator facilities in support of the *Fermi* mission. This provided verification of the LAT instrument design, and validation of the Monte Carlo simulation developed to model the detector performance and accuracy. An extensive operation was carried out in 2006 on the LAT Calibration Unit (CU), a *cut-down* prototype of the

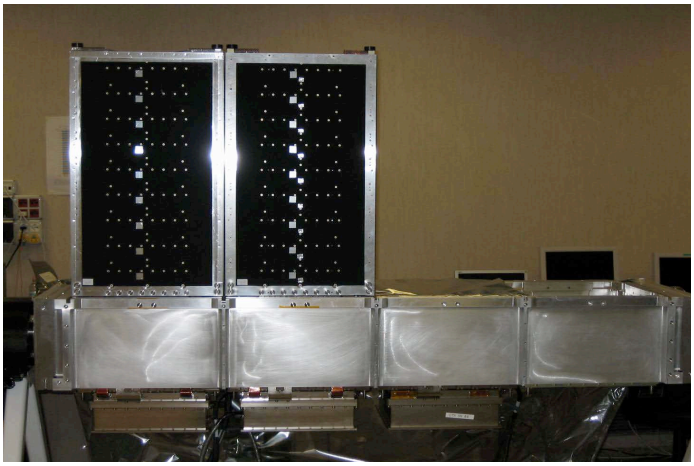

Figure 7.1: The Large Area Telescope Calibration Unit (CU). The two complete flight towers (left) consist of a TKR module (black tower) and CAL module (integrated in the aluminum bay). The third tower consists of a CAL module and the fourth tower is empty. The metal enclosure and the ACD tiles are not shown. Credit: `Fermi Collaboration`

actual instrument constructed with reserve components of the subsystems. The CU was subjected to multiple particle beams of photons, electrons/positrons, protons, and pions at CERN and heavy-ions consisting of carbon and xenon at GSI to analyze the performance of the detector. This allowed for examination of the physical processes (i.e. particle showers, multiple scattering, etc.) undergoing in the LAT instrument, and important detector parameters (i.e. point spread functions, energy reconstruction, ACD veto/backsplash) to be studied in a *controlled* environment.

7.2.1 Calibration Unit

The Calibration Unit is shown in Figure 7.1, composed of two complete flight towers, both with a tracker and calorimeter module. In addition, a single calorimeter module was integrated adjacent to the two tower in a 1×4 aluminum support grid structure, identical to the flight grid. The fourth bay of the CU was left vacant, as the majority of events observed by LAT involve two individual flight towers or calorimeter modules. The independent calorimeter module was used exclusively

Particle Type	Beam Energy (GeV)	Incidence Angle (°)
e^-	10	0, 10, 20, 30, 45, 60
e^-	20	0, 10, 20, 30, 45, 60
e^-	50	0, 10, 20, 30, 45, 60
e^-	100	0, 10, 20, 30, 45, 60
e^-	196	0, 10, 20, 30, 45, 60
e^-	282	0, 10, 20, 30, 45, 60
p	20	0
p	100	0, 45, 90
p	150	0

Table 7.1: Summary of beam tests performed at SPS using the Calibration Unit.

for high inclination angles, events that are directly incident the calorimeter and not passing through the tracker. The $L-$shape construction allowed for nearly all possible events within acceptance in space to be studied. The structure was enclosed in an aluminum casing with 5 ACD tiles positioned on the exterior at different locations that varied during the campaigns. As in the flight LAT, each of the 2.5 towers were controlled by a Tower Electronic Module (TEM) connected to the Global trigger Anticoincidence Signal distribution Unit (GASU). During the flight operations, the TEM is responsible for generating trigger requests if one or more of the hardware event trigger (as seen in section 3.3.4) criteria is satisfied, however, during the beam tests the GASU was externally triggered.

7.2.2 SPS Beam Test

The concentration of the analysis is on beam test runs from the H4 line of the Super Proton Synchrotron (SPS) at CERN, as the beams extracted provide the highest energies of the campaigns with momenta from 10 up to 300 GeV/c. This enabled studies to be conducted on high energy particle showers with high occupancy in the tracker modules. A summary of the beam test parameters of the SPS campaign for particles of interest, proton and electron runs, are shown in Table 7.1. The impact

point of the beam and the incident angle varied over the collection of 17.8×10^6 electrons and 0.8×10^6 protons statistics. The configuration of the SPS campaign consisted of, in traversing order, two helium gas threshold Cherenkov counters for the particle identification and two plastic scintillators providing the external trigger signal.

7.3 Beam Test Analysis

The emphasis of this study is placed on beam tests of 50 GeV electron, 100 and 150 GeV proton runs, in order examine high energy showers that may begin in the tracker with comparable energy deposition in the calorimeter. As describe in chapter 2, nuclear interaction lengths are much longer than electromagnetic radiation length in high density material, thus, hadronic events at higher energies will contaminate lower energy bins. A Monte Carlo Simulation based on the `Geant4` [89] toolkit is employed here to compare with observed data during the beam tests. The electron MC runs were generated with the Landau-Pomeranchuk-Migdal (LPM) effect accurately applied [13]. The LPM effect results in the energy dependent reduction of the bremsstrahlung cross section due to multiple scattering [90]. The proton MC runs employ the `QGSP_BERT` [91] physics lists for hadronic interactions. Additionally, the MC runs include $0.075X_0$ of lead in front of the CU as for the setup at the SPS beam test.

7.3.1 Event Quality

Although beam tests are essentially accomplished in a *controlled* environment, there still remains potential for contamination and additional diminishing effects on the measured signals. The following are possible origins that effect the quality of the data:

- *Cosmic Radiation Contamination*:

  At sea level, the cosmic ray muons may interact in the detector, creating tracks and depositing energy in the calorimeter as minimum ionizing particles. If coinciding with the particle beam, the reconstructed track can be distorted and misaligned with the centroid of the energy in the calorimeter. Furthermore, muons can create independent events in the adjacent tracker and calorimeter modules of CU.

- *Beam Contamination*:

  The particle beams may not only be contaminated by an outside source (i.e. coincidence cosmic muons), but also particle of different species within the beam itself. The contamination of the electron beam was considered negligible, the proton beam did contain pions and external triggers by the Cherenkov detectors were used to aid in the separation of the species.

- *Multi-particle Beam Events*:

  Multi-particle beam events or *pile-up* events can occur if the beam rate is high enough to be comparable to the minimum instrument readout dead-time. This results in interference between detector electronic pulses and may lead to false readings.

Fiducial cuts were applied to the beam test data to effectively suppress these effects, constraining the minimum and maximum raw energy deposited in the calorimeter and restricting the time between events. Additional effects on the measured beam test data may originate from the noise within the detector and gaps in the geometry of instruments. The tracker has been designed to be low noise instrument and is not of concern in this study. Events were also chosen for tracks confined to one tower to minimize gap effects.

7.3.2 Energy Resolution

The energy resolution of the LAT instrument has been studied extensively, as presented in [12], with a total energy resolution of approximately 20% up to 1 TeV electrons. The object of this section is not to reassess the energy resolution, but to compare the raw energy deposited by electromagnetic showers compared to hadronic showers for further analysis. The raw energy deposited (CalEnergyRaw) and the *optimal*[1] reconstructed energy (CTBBestEnergy) in the calorimeter is shown in Figures 7.2a and 7.2b, respectively for the 100 and 150 GeV protons, and the 50 GeV electrons. The proton energies are shifted greatly to lower energy as the detector has poor resolution for hadronic particles. The reconstructed energy for the higher energy protons becomes better, as the fraction of energy loss of a hadrons through the electromagnetic channel increases with energy and the reconstruction algorithm(s) are developed for EM events. The raw energy deposited and energy reconstruction in the calorimeter by 50 GeV electrons display much better resolution. As one can see, a relatively large number of high energy protons deposited energy that overlaps the deposited energy of the electrons. It should be noted, the energy deposited in each calorimeter crystal was 9% higher for the beam test data than of the simulation data. The deposited energy of the beam test data was scaled by 9% to eliminate the discrepancy, although, flight data does not exhibit the same characteristic. This believed to be isolated to the CU and the conditions of the beam test campaigns.

7.3.3 Tracker Energy Profile

As I am concerned with event information provided by the tracker, the energy profile of two *merit* variables in the LAT analysis are shown in Figures 7.3a and 7.3b. The TkrSurplusHitRatio describes the ratio of the number of tracker hit clusters

[1]CTBBestEnergy is the best reconstructed energy employing a classification tree to determined the *best* reconstruction method of the parametric, profile, and likelihood methods.

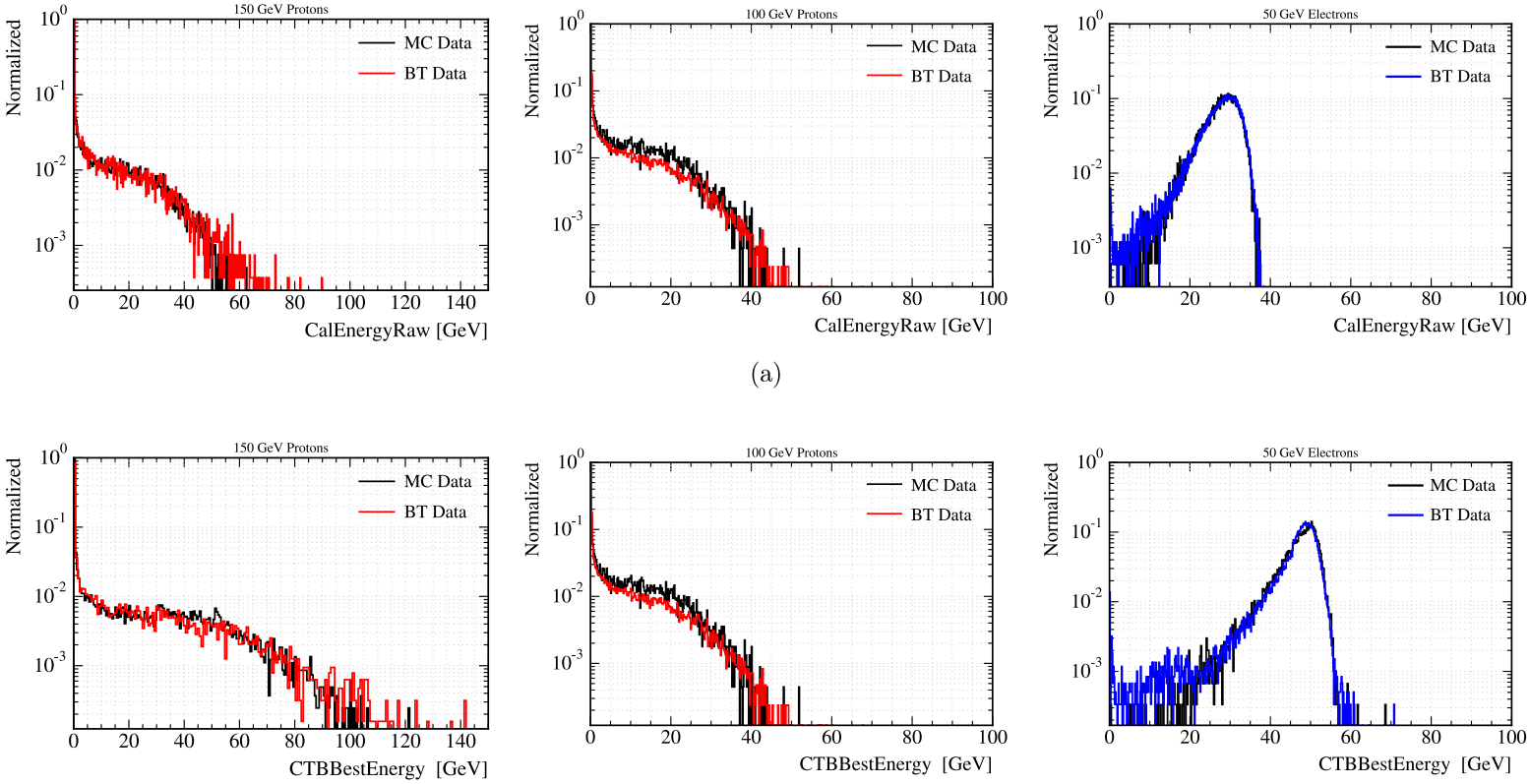

Figure 7.2: Comparison of the (a) CalEnergyRaw and (b) CTBestEnergy quantities observed in the MC simulations and data for the beam test run at 150 GeV (*left*), 100 GeV (*middle*), and 50 GeV (*right*) at 0°.

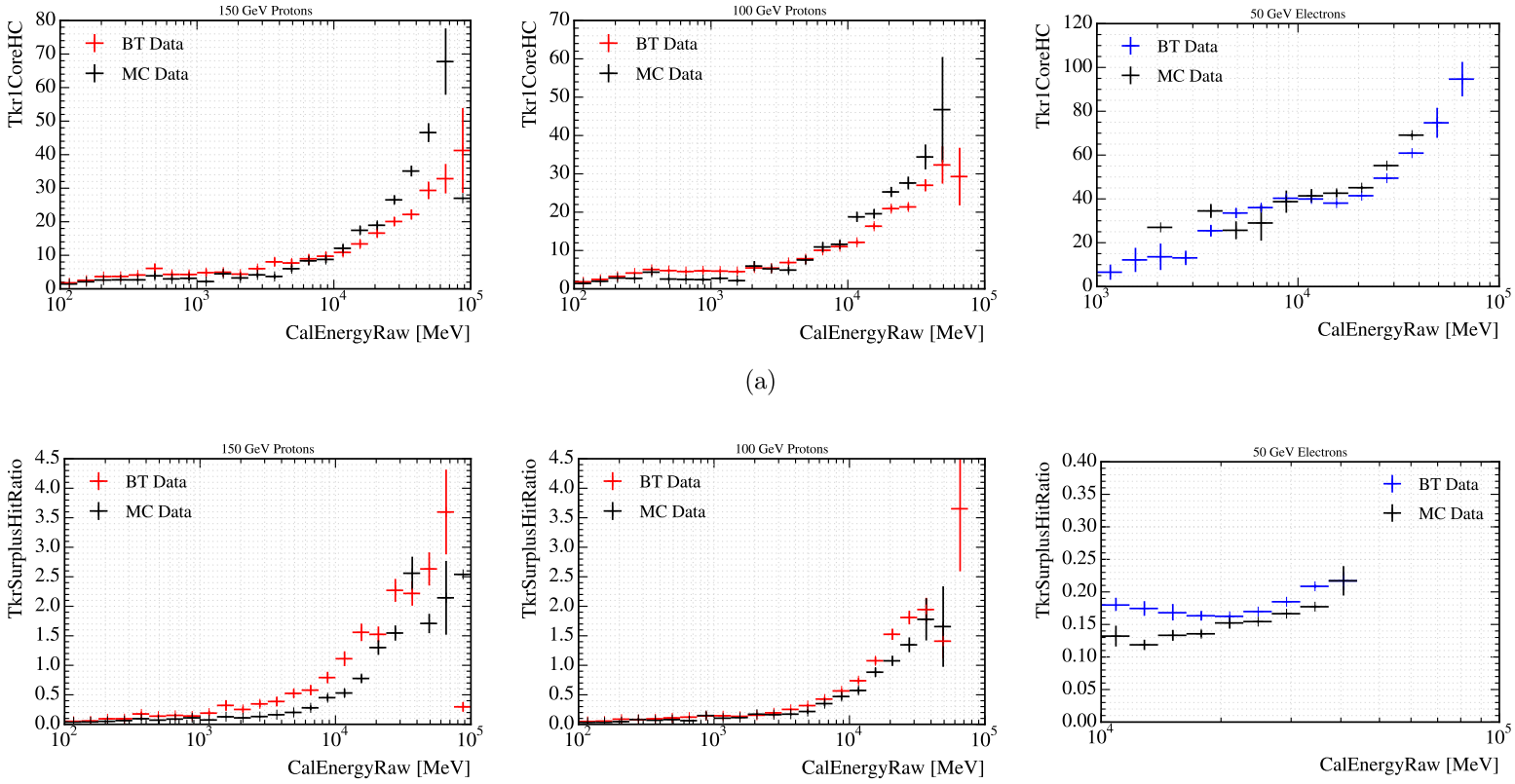

Figure 7.3: Energy profile comparison of the (a) Tkr1CoreHC and (b) TkrSurplusHitRatio quantities observed in the MC simulations and data for the beam test run at 150 GeV (*left*), 100 GeV (*middle*), and 50 GeV (*right*) at 0°.

outside an energy and angle dependent cone around the reconstructed axis of the best track to the number hit clusters inside. The Tkr1CoreHC observable is the number of hit clusters within a roughly cylindrical region, radius of roughly one Moliére radius of tungsten, the around the hits in each plane between the first and last on the best track, not including the hit clusters that belong to the track itself. As shown, the number of hits (secondaries) increases with raw energy, this directly shows that the particles, electrons and protons, begin their cascades or *preshower* in the tracker. Above 20 GeV, where these events will pass the on-board `Gamma` filter discussed in section 4.3.4, and be sent to ground for further analysis. The analysis in the following sections focuses on these events, as the protons may be easily misidentified as electrons due to their shower profile.

7.4 Discriminating Variables

I have developed the following TKR variables to aid in electron identification while discriminating against protons. Eight variables were constructed to examine the lateral distribution utilizing concentric cylinders at various radii around the reconstructed particle track, approximately scaling with the Moliére radius of tungsten. As the lateral distribution of electromagnetic showers deposit energy around the track at: 90% within 1 MR, 95% within 2 MR, and 99% within 3.5 MR, the constructed variables exploit these fundamentals. Two additional variables are constructed to examine the distribution within 0.5 MR tin order to study non-interacting events in the tracker. To characterize the longitudinal distribution of the shower, four variables were developed using the inherent sections of the tracker (*front, back, and bottom*). All variables calculate: (i) Time-over-Threshold, an estimator of the charge collected by the silicon strips from the time the signal(s) are above a given threshold, and (ii) the hit count within the defined region. Each variable is describe below:

- **Tkr1InnerCoreToT** Total ToT count within a roughly cylindrical region (radius of 5 mm) around the hits in each plane between the first and last on the best track (Fig. 7.4 $left$).

- **Tkr1InnerCoreHC** Number of clusters within a roughly cylindrical region (radius of 5 mm) around the hits in each plane between the first and last on the best track (Fig. 7.4 $right$).

- **Tkr1CoreToT** Total ToT count within a roughly cylindrical region (radius of 10 mm) around the hits in each plane between the first and last on the best track (Fig. 7.5 $left$).

- **Tkr1CoreHC**[2] Number of clusters within a roughly cylindrical region (radius of 10 mm) around the hits in each plane between the first and last on the best track (Fig. 7.5 $right$).

- **Tkr1HaloToT** Total ToT count within a roughly cylindrical region (radius of 20 mm) around the hits in each plane between the first and last on the best track (Fig. 7.6 $left$).

- **Tkr1HaloHC** Number of clusters within a roughly cylindrical region (radius of 20 mm) around the hits in each plane between the first and last on the best track (Fig. 7.6 $right$).

- **Tkr1OuterHaloToT** Total ToT count within a roughly cylindrical region (radius of 35 mm) around the hits in each plane between the first and last on the best track (Fig. 7.7 $left$).

[2]An original variable, used in analysis for consistency with relation to new variables.

- **Tkr1OuterHaloHC** Number of clusters within a roughly cylindrical region (default radius 35 mm) around the hits in each plane between the first and last on the best track (Fig. 7.7 *right*).

- **TkrFrontBackRatioToT** Ratio of the total ToT count inside an energy and angle dependent cone in the front region to the back region of the tracker (Fig. 7.8 *left*).

- **TkrFrontBackRatioHC** Ratio of the total number of clusters inside an energy and angle dependent cone in the front region to the back region of the tracker (Fig. 7.8 *right*).

- **TkrBackBottomRatioToT** Ratio of the total ToT count inside an energy and angle dependent cone in the back region to the bottom region of the tracker (Fig. 7.9 *left*).

- **TkrBackBottomRatioHC** Ratio of the total number of clusters inside an energy and angle dependent cone in the back region to the bottom region of the tracker (Fig. 7.9 *right*).

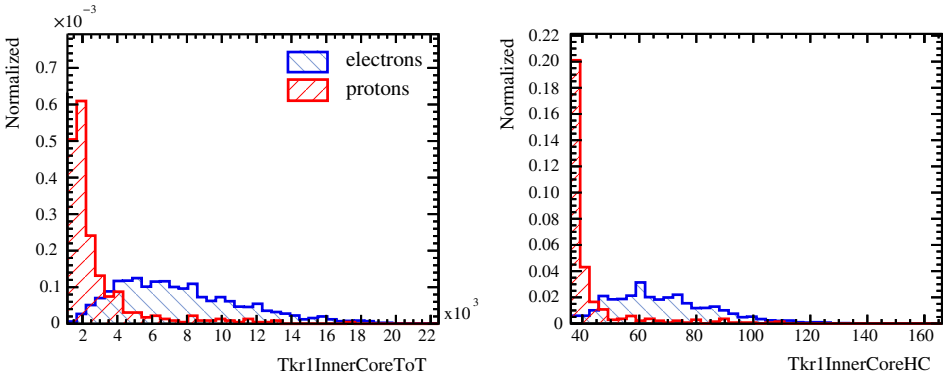

Figure 7.4: Distribution of Tkr1InnerCoreToT (*left*) and Tkr1InnerCoreHC (*right*) for electron and proton events.

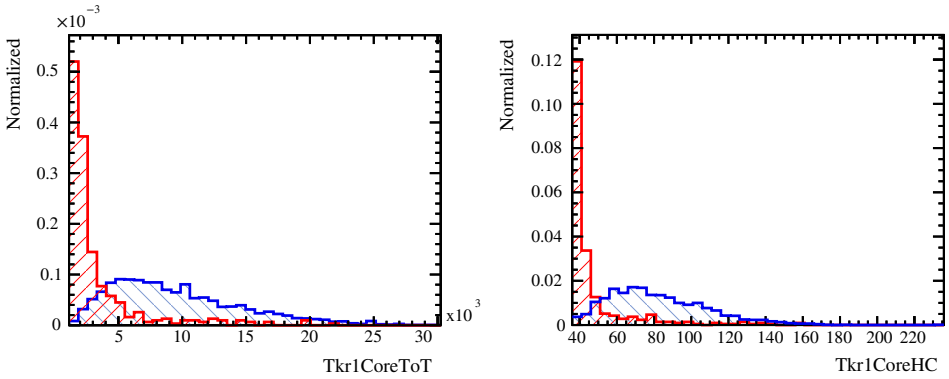

Figure 7.5: Distribution of Tkr1CoreToT (*left*) and Tkr1CoreHC (*right*) for electron and proton events.

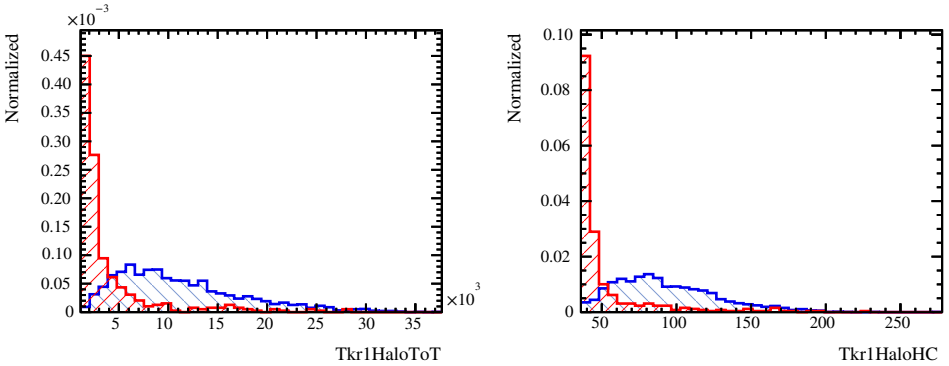

Figure 7.6: Distribution of Tkr1HaloToT (*left*) and Tkr1HaloHC (*right*) for electron and proton events.

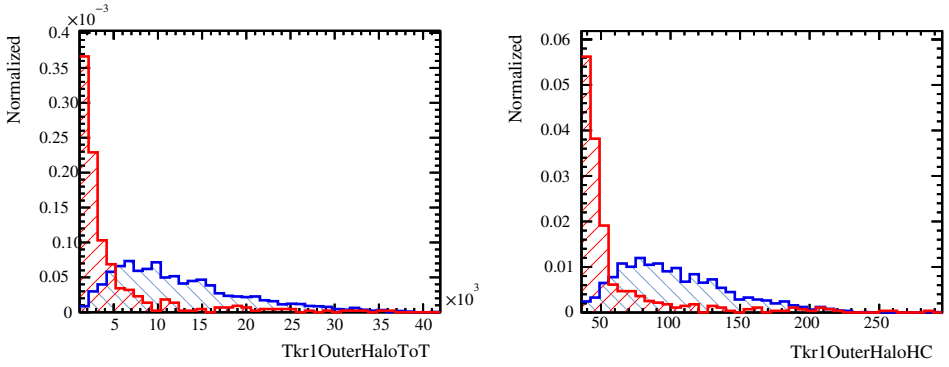

Figure 7.7: Distribution of Tkr1OuterHaloToT (*left*) and Tkr1OuterHaloHC (*right*) for electron and proton events.

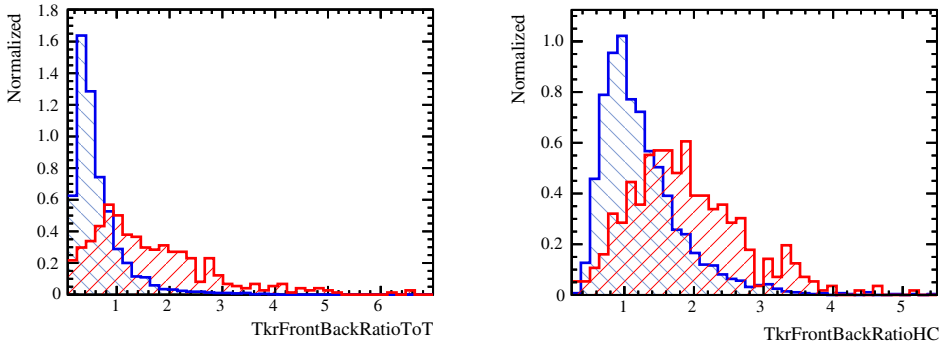

Figure 7.8: Distribution of TkrFrontBackRatioToT (*left*) and TkrFrontBackRatioHC (*right*) for electron and proton events.

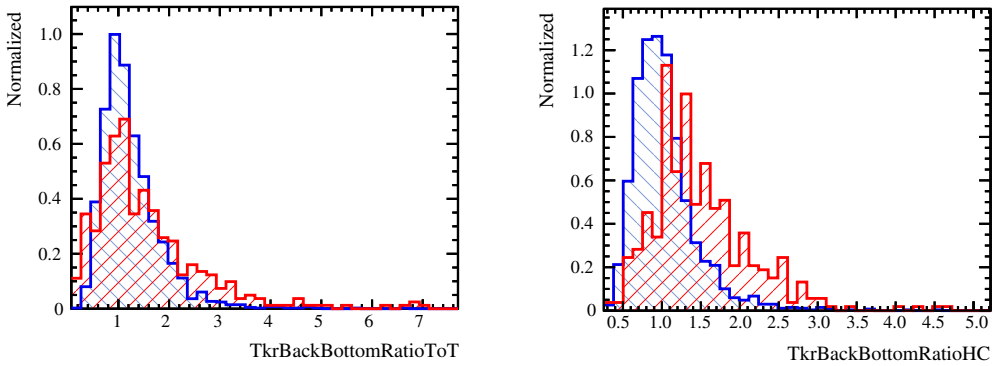

Figure 7.9: Distribution of TkrBackBottomRatioToT (*left*) and TkrBackBottomRatioHC (*right*) for electron and proton events.

The variable distributions in Figures 7.4–7.8, show a clear separation between electrons and protons. In Figure 7.9, the ratio of the *bottom* to *back* layers in the ToT count and hit count display a clear overlap of the electron and protons. This can be expected as events the were selected within the beam test were interacting hadronic events, and the cascades began in the tracker.

Parameters	GeV
Number of Trees	250
AdaBoost β	0.45
Minimum Node Size	5
Tree Maximum Depth	3

Table 7.2: Tuning parameters of the BDT classifier developed.

7.5 MVA Analysis

The overall LAT analysis of $\gamma-$rays, electrons, and protons, heavily rely on multiple classification trees (CTs) [10, 12, 14, 13, 92]. The Pass7[3] data analysis of electrons utilized two CTs, one with all TKR variables, and the other with all CAL variables as in the $\gamma-$ray background rejection analysis to map the event topology [88]. The following classifier was developed to provide an independent classifier based on variables that were developed to describe electromagnetic showers. All variables described the preceding section are used in the development of the following BDT. The parameters of the BDT created are outlined in Table 7.2 and the tuning parameters were chosen through an iterative process to find the classifier with optimal performance for the training set as applied to the testing sample. The samples were divided randomly. The response of the developed BDT is shown in Figures 7.10, projecting the outputs of the classifier for the training sample on the testing sample.

As in the previous study, the discrepancies in the distributions of the training and testing samples may be attributed to some overtraining, however, this has very little influence on the overall classification. Employing the Kolmogorov–Smirnov (K–S) test on the two sets, the statistical probability is: 0.263 (0.168) for the signal (background) sample in the near test classifier. The classifier the does not perform

[3]The Fermi collaboration analysis framework are designated by Pass#, currently on Pass8.

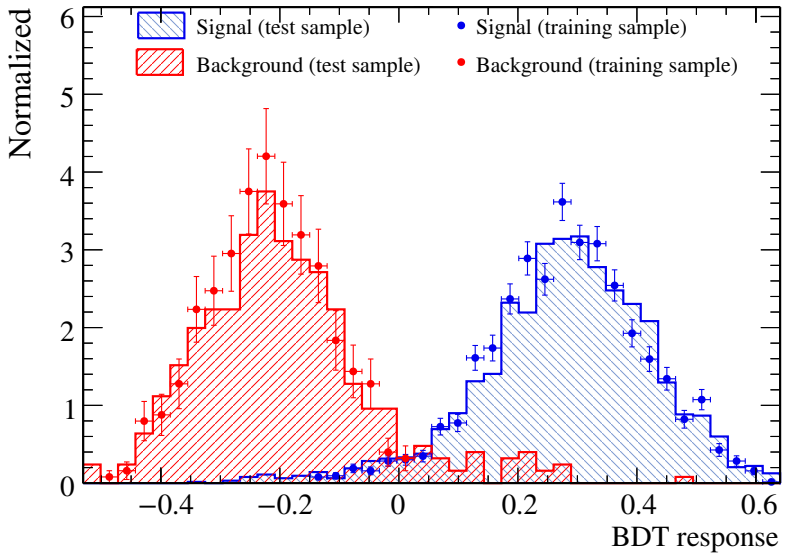

Figure 7.10: Beam Test BDT classifier response on training and testing samples.

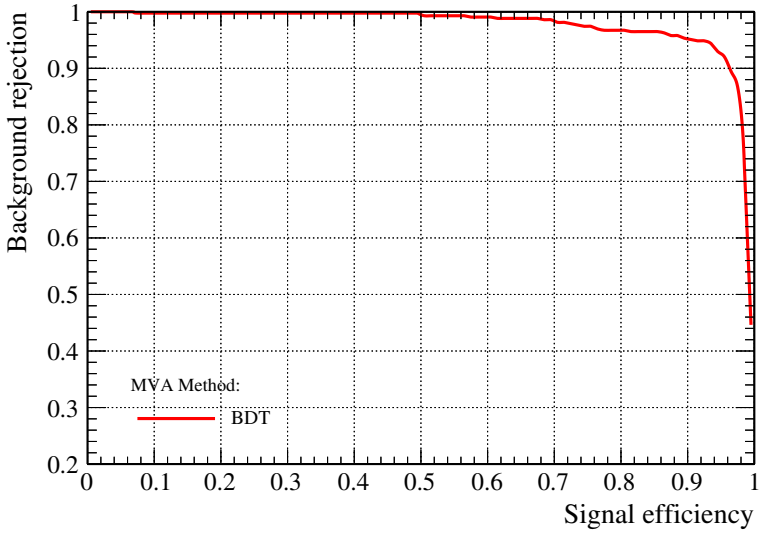

Figure 7.11: Beam Test BDT classifier ROC curve.

as well as the classifiers developed in the previous chapter, which can be expected as the CALET study uses all information of each subsystem. A common FoM of a binary classifier is the receiver operating characteristic (ROC) curve (as shown in Figure 7.11), here illustrates the performance of the classifier at different threshold of

the background (proton) rejection. The overall result of applying the classifier on the Beam Test data produced an electron sample with a relative hadronic background contamination of approximately 10^{-2} whilst maintaining an electron efficiency of $\sim$70%.

7.6 Conclusion

The result presented in the previous section is substantial considering only information extracted from the tracker was employed, and no characteristics from the particle shower in the calorimeter. As noninteracting protons were excluded from this analysis, previous studies conducted on beam test and simulation data have shown an increase as much as to 95% electron efficiency with a relative hadronic background contamination of approximately 10^{-2}, when included. The variables presented here are now implemented in the full Fermi LAT Monte Carlo simulation and preliminary studies in the Pass8 framework has shown to produce similar results (as presented above) over the entire observable energy range. This technique was able to achieve approximately 88% electron efficiency at a 10% relative background contamination, with 10^6 background events at a 10 to 1 ratio with electrons. This approach has proven to be very effective and the significance on flight data is still being investigated.

Closing Remarks

The main goal of this dissertation was the study of electron identification in both the CALET and Fermi LAT instruments. In particular, how can I improve the performance of discriminating against the vast background to increase the electron efficiency. Since CALET is just beginning observations, implementing such techniques in the analysis would allow for higher purity electron observations and increase the chances of resolving a feature in the electron spectrum. As for the Fermi LAT electron analysis, we expect a current spectrum to be in press by early 2016 and hope the results are as successful as the first published ones. Nonetheless, the success of the Fermi LAT and the future of the CALET mission has reinvigorated the field of cosmic rays and does not show signs of slowing down. Recently, during the checkout phase of the instrument, CALET has made it's first $\sim$1 TeV candidate observation (shown in Fig. ii), and will continue to build upon this achievement. Both collaborations have an amazing team of scientists, engineers, and support staff working together in the pursuit of science, and it has been a pleasure working with them. The impacts of both experiments will definitely remain in the forefront for years to come.

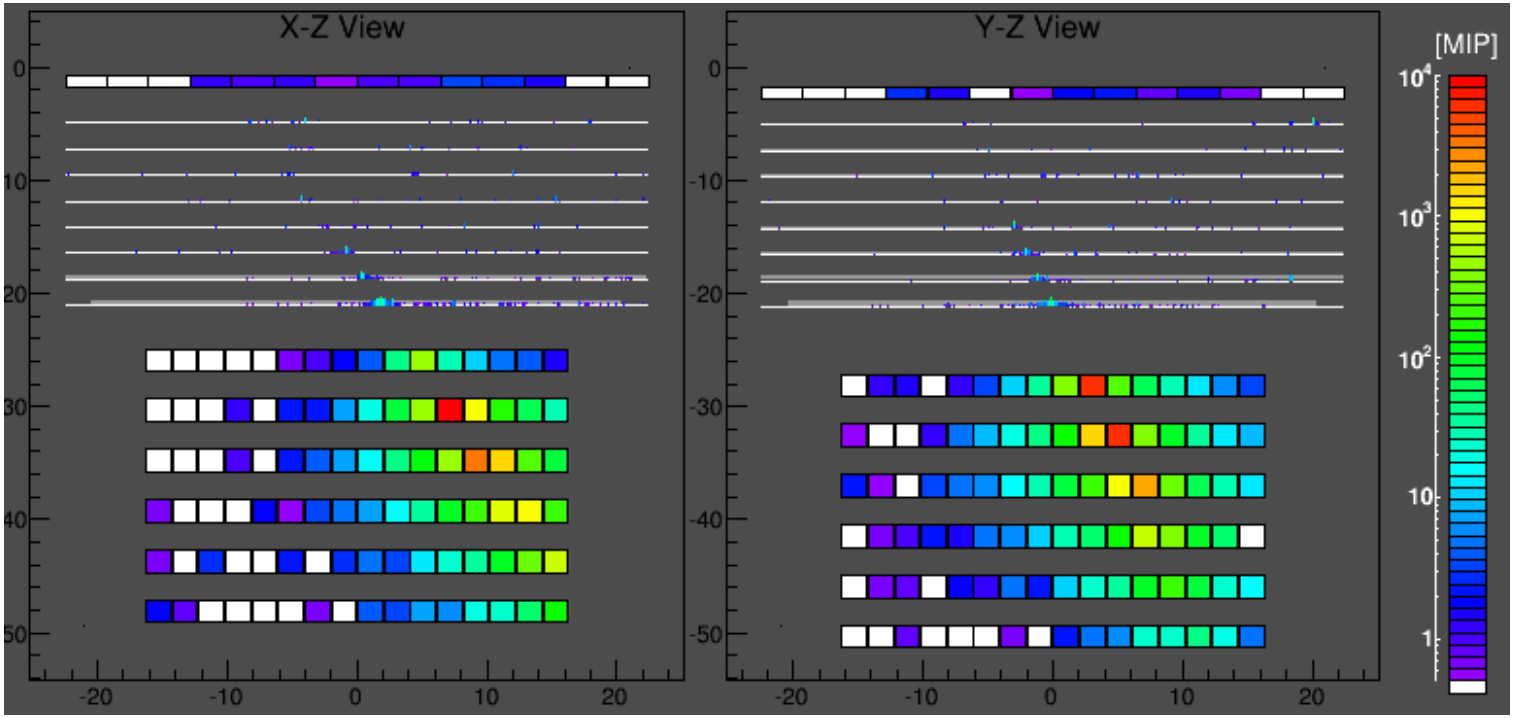

Figure ii: An electron candidate ($\sim$ 1 TeV) observed on October 14, 2015 during the initial verification and data calibration. Credit: JAXA

Appendix A

CALET Analysis Supplement

A.1 Energy Measurement

The energy measurements of electrons and protons as compared with there incident energy are shown Figure A.1(a) and A.1(b), respectively. These measurements are post - High Energy Trigger.

A.2 Event Type

The four event types reference in section 6.1 are shown in Figure A.2. The conditions of each event type requires that the trajectory of the particle must traverse the following:

Event Type I:

`(1)` CHD - top layer, `(2)` TASC - top inside layer, and `(3)` TASC - bottom insider layer.

Event Type II:

`(1)` CHD - top layer, `(2)` TASC - top lateral layer, and `(3)` TASC - bottom insider layer.

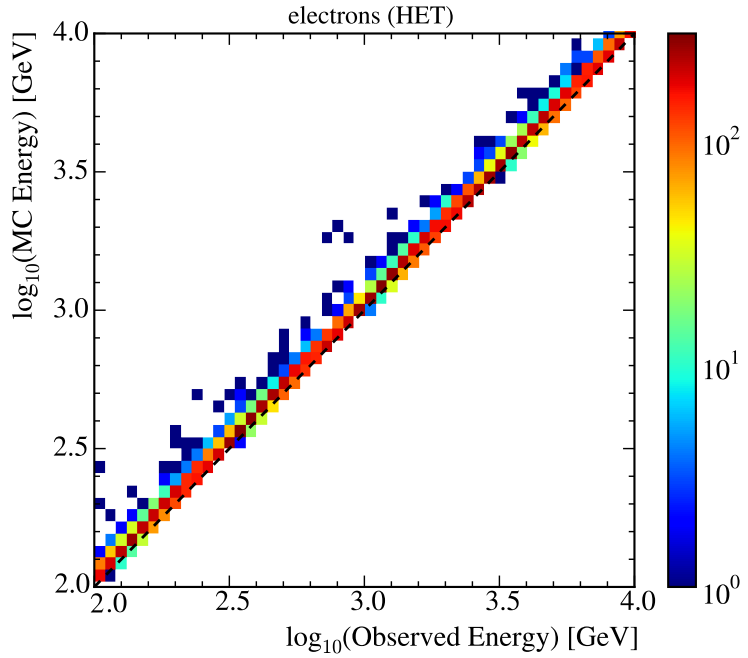

(a)

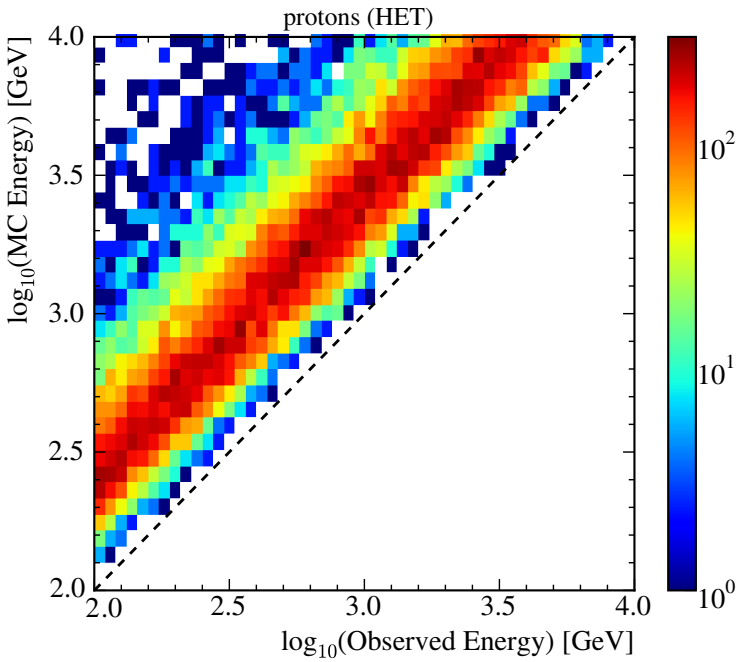

(b)

Figure A.1: Observed Energy vs. MC Incident Energy for (a) electrons and (b) protons. The *dash* line represents observed energy equal to incident energy.

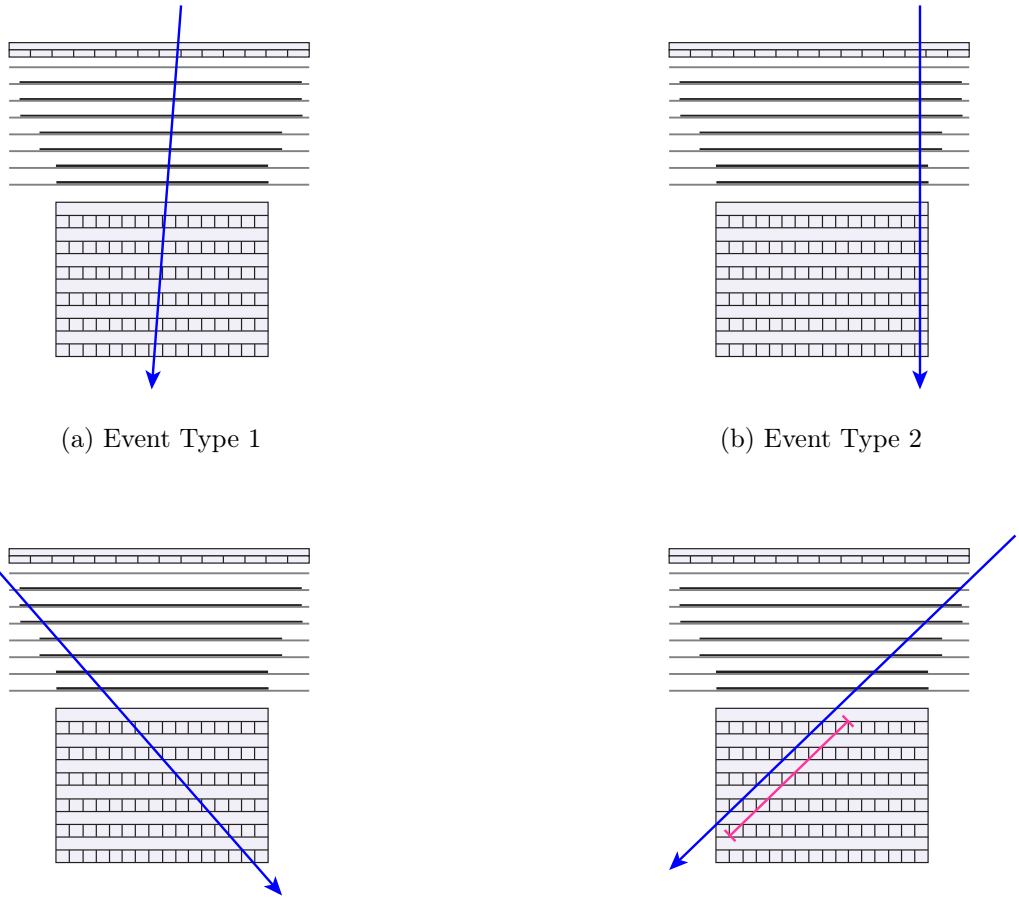

(a) Event Type 1

(b) Event Type 2

(c) Event Type 3

(d) Event Type 4

Figure A.2: Event Types of Acceptance.

Event Type III:

`(1)` IMC: not top layer, `(2)` IMC: 4^{th} layer, `(3)` TASC - top inside layer, and `(4)` TASC - bottom insider layer.

Event Type IV:

`(1)` IMC: not top layer, `(2)` IMC: 4^{th} layer, `(3)` TASC - top inside layer, and `(4)` TASC - not bottom insider layer and >27 X_0.

Bibliography

[1] V. F. Hess. Über Beobachtungen der durchdringenden Strahlung bei sieben Freiballonfahrten. *Physikalische Zeitschrift*, 13:1084–1091, November 1912.

[2] C. Anderson. The Positive Electron. *Physical Review*, 43(6):491–494, March 1933.

[3] J. Earl. Cloud-Chamber Observations of Primary Cosmic-Ray Electrons. *Physical Review Letters*, 6(3):125–128, February 1961.

[4] P. Meyer and R. Vogt. Electrons in the Primary Cosmic Radiation. *Physical Review Letters*, 6(4):193–196, February 1961.

[5] J. De Shong, R. Hildebrand, and P. Meyer. Ratio of Electrons to Positrons in the Primary Cosmic Radiation. *Physical Review Letters*, 12(1):3–6, January 1964.

[6] J. Alcaraz, B. Alpat, G. Ambrosi, et al. Leptons in Near Earth Orbit. *Physics Letters B*, 484(1-2):10–22, June 2000.

[7] J. Chang, J. H. Adams, H. S. Ahn, et al. An Excess of Cosmic Ray Electrons at Energies of 300 - 800 GeV. *Nature*, 456(7220):362–5, November 2008.

[8] K. Yoshida, S. Torii, T. Yamagami, et al. Cosmic-Ray Electron Spectrum above 100 GeV from PPB-BETS Experiment in Antarctica. *Advances in Space Research*, 42(10):1670–1675, November 2008.

[9] O. Adriani, G. C. Barbarino, G. A. Bazilevskaya, et al. An Anomalous Positron Abundance in Cosmic Rays with Energies 1.5-100 GeV. *Nature*, 458(7238):607–9, April 2009.

[10] W. B. Atwood, A. A. Abdo, M. Ackermann, et al. The Large Area Telescope on the Fermi Gamma-ray Space Telescope Mission. *The Astrophysical Journal*, 697(2):1071–1102, June 2009.

[11] S. Torii. The Calorimetric Electron Telescope (CALET) for High Energy Astroparticle Physics on the International Space Station. In *Proceedings of the 33rd International Cosmic Ray Conference*, Rio de Janeiro, 2013.

[12] A. Abdo, M. Ackermann, M. Ajello, et al. Measurement of the Cosmic Ray e++ e- Spectrum from 20 GeV to 1 TeV with the Fermi Large Area Telescope. *Physical Review Letters*, 102(18):181101, May 2009.

[13] M. Ackermann, M. Ajello, W. B. Atwood, et al. Fermi LAT Observations of Cosmic-Ray Electrons from 7 GeV to 1 TeV. *Physical Review D*, 82(9):092004, November 2010.

[14] M. Ackermann, M. Ajello, A. Allafort, et al. Measurement of Separate Cosmic-Ray Electron and Positron Spectra with the Fermi Large Area Telescope. *Physical Review Letters*, 108(1):011103, January 2012.

[15] J. A. Simpson. Elemental and Isotopic Composition of the Galactic Cosmic Rays. *Annual Review of Nuclear and Particle Science*, 33(1):323–382, December 1983.

[16] P. Sokolsky. *Introduction to Ultrahigh Energy Cosmic Ray Physics*. Westview, 2004.

[17] K. Abe, H. Fuke, S. Haino, et al. Measurements of Cosmic-Ray Proton and Helium Spectra from the BESS-Polar Long-Duration Balloon Flights over Antarctica. *eprint arXiv:1506.01267*, 2015.

[18] J. Blümer, R. Engel, and J. R. Hörandel. Cosmic Rays from the Knee to the Highest Energies. *Progress in Particle and Nuclear Physics*, 63(2):293–338, October 2009.

[19] C. Merino, editor. *Lectures on Particle Physics, Astrophysics and Cosmology*, volume 161 of *Springer Proceedings in Physics*. Springer International Publishing, Cham, 2015.

[20] K. Greisen. End to the Cosmic-Ray Spectrum? *Physical Review Letters*, 16(17):748–750, April 1966.

[21] G. T. Zatsepin and V. A. Kuz'min. Upper Limit of the Spectrum of Cosmic Rays. *Journal of Experimental and Theoretical Physics Letters*, 4, 1966.

[22] J. Abraham, P. Abreu, M. Aglietta, et al. Measurement of the Energy Spectrum of Cosmic Rays above 1018 eV using the Pierre Auger Observatory. *Physics Letters B*, 685(4-5):239–246, March 2010.

[23] I. I. Tkachev. Telescope Array Observatory observations of the Greisen - Zatsepin - Kuzmin effect. *Physics-Uspekhi*, 54(9):954–961, September 2011.

[24] E. S. Seo, J. F. Ormes, R. E. Streitmatter, et al. Measurement of Cosmic-Ray Proton and Helium Spectra during the 1987 Solar Minimum. *The Astrophysical Journal*, 378:763, September 1991.

[25] N. L. Grigorov, Y. V. Gubin, B. M. Jakovlev, et al. Energy Spectrum of Primary Cosmic Rays in the 1011-1015 eV According to the Data of Proton-4 Measurements. In *Proceedings of the 12th International Conference on Cosmic Rays*, volume 1, Hobart, 1971.

[26] M. Nagano, M. Teshima, Y. Matsubara, et al. Energy Spectrum of Primary Cosmic Rays above 10 17.0 eV determined from Extensive Air Shower Experiments at Akeno. *Journal of Physics G: Nuclear and Particle Physics*, 18(2):423–442, February 1992.

[27] T. Antoni, W. Apel, A. Badea, et al. KASCADE Measurements of Energy Spectra for Elemental Groups of Cosmic Rays: Results and Open Problems. *Astroparticle Physics*, 24(1-2):1–25, September 2005.

[28] The Pierre Auger Collaboration, P. Abreu, M. Aglietta, et al. The Pierre Auger Observatory I: The Cosmic Ray Energy Spectrum and Related Measurements. In *Proceedings of the 32nd International Cosmic Ray Conference*, Beijing, July 2011.

[29] R. U. Abbasi, T. Abu-Zayyad, M. Allen, et al. First Observation of the Greisen-Zatsepin-Kuzmin Suppression. *Physical Review Letters*, 100(10):101101, March 2008.

[30] D. H. Perkins. *Particle Astrophysics*. Oxford University Press, 2003.

[31] P. Bhattacharjee and G. Sigl. Origin and Propagation of Extremely High-Energy Cosmic Rays. *Physics Reports*, 327(3-4):109–247, April 2000.

[32] E. Fermi. On the Origin of the Cosmic Radiation. *Physical Review*, 75(8):1169–1174, April 1949.

[33] M. S. Longair. *High Energy Astrophysics*. Cambridge University Press, 2011.

[34] W. I. Axford, E. Leer, and G. Skadron. The Acceleration of Cosmic Rays by Shock Waves. In *Proceedings of the 15th International Conference on Cosmic Rays*, volume 11, pages 132–137, Plovdiv, 1977.

[35] A. R. Bell. The Acceleration of Cosmic Rays in Shock Fronts. *Monthly Notices of the Royal Astronomical Society*, 182:147–156, 1978.

[36] R. D. Blandford and J. P. Ostriker. Particle Acceleration by Astrophysical Shocks. *The Astrophysical Journal*, 221:L29, April 1978.

[37] P. Lagage and C. Cesarsky. The Maximum Energy of Cosmic Rays Accelerated by Supernova Shocks. *Astronomy and Astrophysics (ISSN 0004-6361)*, 125:249–257, 1983.

[38] E. Berezhko. Maximum Energy of Cosmic Rays Accelerated by Supernova Shocks. *Astroparticle Physics*, 5(3-4):367–378, October 1996.

[39] T. K. Gaisser. *Cosmic Rays and Particle Physics*. Cambridge University Press, 1990.

[40] M. Su, T. R. Slatyer, and D. P. Finkbeiner. Giant Gamma-ray Bubbles from Fermi-LAT: Active Galactic Nucleus Activity or Bipolar Galactic Wind? *The Astrophysical Journal*, 724(2):1044–1082, December 2010.

[41] V. S. Ptuskin and A. Soutoul. Cosmic-ray Clocks. *Space Science Reviews*, 86(1-4):225–238, 1998.

[42] R. Blandford and D. Eichler. Particle Acceleration at Astrophysical Shocks: A Theory of Cosmic Ray Origin. *Physics Reports*, 154(1):1–75, October 1987.

[43] R. Schlickeiser. *Cosmic Ray Astrophysics*. Springer Science & Business Media, 2002.

[44] K. Yoshida. High-Energy Cosmic-Ray Electrons in the Galaxy. *Advances in Space Research*, 42(3):477–485, August 2008.

[45] V. S. Ptuskin and J. F. Ormes. No Expected Anisotropy of Very High Energy Electrons. In *Proceedings of the 24th International Cosmic Ray Conference*, pages 56–59, Roma, 1995.

[46] M. Boezio, P. Carlson, T. Francke, et al. The Cosmic-Ray Electron and Positron Spectra Measured at 1 AU during Solar Minimum Activity. *The Astrophysical Journal*, 532(1):653–669, March 2000.

[47] M. A. DuVernois, S. W. Barwick, J. J. Beatty, et al. Cosmic-Ray Electrons and Positrons from 1 to 100 GeV: Measurements with HEAT and Their Interpretation. *The Astrophysical Journal*, 559(1):296–303, September 2001.

[48] A. W. Strong, I. V. Moskalenko, and V. S. Ptuskin. Cosmic-Ray Propagation and Interactions in the Galaxy. *Annual Review of Nuclear and Particle Science*, 57(1):285–327, November 2007.

[49] I. V. Moskalenko and A. W. Strong. Production and Propagation of Cosmic-Ray Positrons and Electrons. *The Astrophysical Journal*, 493(2):694–707, February 1998.

[50] A. W. Strong and I. V. Moskalenko. Propagation of Cosmic-Ray Nucleons in the Galaxy. *The Astrophysical Journal*, 509(1):212–228, December 1998.

[51] F. Aharonian, A. G. Akhperjanian, U. Barres de Almeida, et al. Energy Spectrum of Cosmic-Ray Electrons at TeV Energies. *Physical Review Letters*, 101(26):261104, December 2008.

[52] M. Aguilar, D. Aisa, A. Alvino, et al. Electron and Positron Fluxes in Primary Cosmic Rays Measured with the Alpha Magnetic Spectrometer on the International Space Station. *Physical Review Letters*, 113(12):121102, September 2014.

[53] O. Adriani, G. C. Barbarino, G. A. Bazilevskaya, et al. Cosmic-Ray Electron Flux Measured by the PAMELA Experiment between 1 and 625 GeV. *Physical Review Letters*, 106(20):201101, May 2011.

[54] O. Adriani, G. C. Barbarino, G. A. Bazilevskaya, et al. Cosmic-Ray Positron Energy Spectrum Measured by PAMELA. *Physical Review Letters*, 111(8):081102, August 2013.

[55] A. D. Panov. Electrons and Positrons in Cosmic Rays. *Journal of Physics: Conference Series*, 409(1):012004, February 2013.

[56] C. E. Fichtel and J. I. Trombka. Gamma-Ray Astrophysics: New Insight Into the Universe. *NASA Reference Publication*, 1386, October 1997.

[57] K. Olive. Review of Particle Physics. *Chinese Physics C*, 38(9):090001, August 2014.

[58] C. Leroy and P. G. Rancoita. *Principles of Radiation Interaction in Matter and Detection*. World Scientific, 2009.

[59] W. R. Leo. *Techniques for Nuclear and Particle Physics Experiments: A How-to Approach*. Springer Science & Business Media, 2012.

[60] R. Wigmans. Calorimetry. In *AIP Conference Proceedings*, volume 674, pages 144–168. AIP, July 2003.

[61] E. Longo and I. Sestili. Monte Carlo Calculation of Photon-Initiated Electromagnetic Showers in Lead Glass. *Nuclear Instruments and Methods*, 128(2):283–307, October 1975.

[62] R. K. Bock and A. Vasilescu. *The Particle Detector BriefBook*. Springer Science & Business Media, 1998.

[63] D. E. Groom. Energy Flow in a Hadronic Cascade: Application to Hadron Calorimetry. *Nuclear Instruments and Methods in Physics Research Section A: Accelerators, Spectrometers, Detectors and Associated Equipment*, 572(2):633–653, March 2007.

[64] K. Yoshida. The Science Objectives for CALET. In *Proceedings of the 32nd International Cosmic Ray Conference*, volume 6, Beijing, 2011.

[65] Y. Shimizu. The CALET CHD for Determination of Nuclear Charge. In *Proceedings of the 32nd International Cosmic Ray Conference*, pages 391–394, Beijing, 2011.

[66] P. Maestro. High-Energy Astroparticle Physics with CALET. *Journal of Physics: Conference Series*, 409:012026, February 2013.

[67] Y. Akaike. Expected CALET Telescope Performance from Monte Carlo Simulations. In *Proceedings of the 32nd International Cosmic Ray Conference*, volume 6, pages 371–374, Beijing, 2011.

[68] T. Niita, S. Torii, Y. Akaike, et al. Energy Calibration of Calorimetric Electron Telescope (CALET) in Space. *Advances in Space Research*, 55(11):2500–2508, June 2015.

[69] Y. Ueyama, S. Torii, and K. Katsuaki. The Event Trigger System for CALET. In *Proceedings of the 32nd International Cosmic Ray Conference*, volume 6, pages 387–390, Beijing, 2011.

[70] U. Y. Oshitaka, T. S. Hoji, K. K. Atsuaki, et al. The CALET Structure and Thermal Model used for Beam Test at CERN. In *Proceedings of the 33rd International Cosmic Ray Conference*, Rio de Janeiro, 2013.

[71] M. Ackermann. Search for Gamma-ray Spectral Lines with the Fermi Large Area Telescope and Dark Matter Implications. *Physical Review D*, 88:082002, May 2013.

[72] http://fermi.gsfc.nasa.gov.

[73] A. Moiseev, R. Hartman, J. F. Ormes, et al. The Anti-Coincidence Detector for the GLAST Large Area Telescope. *Astroparticle Physics*, 27(5):339–358, June 2007.

[74] F. Belli, L. Andreanelli, F. Angelini, et al. The GLAST LAT Tracker Construction and Test. *Nuclear Instruments and Methods in Physics Research Section A: Accelerators, Spectrometers, Detectors and Associated Equipment*, 570(2):276–280, January 2007.

[75] J. E. Grove, W. N. Johnson, M. S. Strickman, et al. The Calorimeter for the GLAST Large Area Telescope. In *AIP Conference Proceedings*, volume 921, pages 550–551. AIP, 2007.

[76] M. Ackermann, M. Ajello, A. Albert, et al. The Fermi Large Area Telescope on Orbit: Event Classification, Instrument Response Functions, and Calibration. *The Astrophysical Journal Supplement Series*, 203(1):4, November 2012.

[77] P. C. Bhat. Multivariate Analysis Methods in Particle Physics. *Annual Review of Nuclear and Particle Science*, 61:281–309, October 2011.

[78] L. Breiman, J. Friedman, C. J. Stone, and R. A. Olshen. *Classification and Regression trees*. CRC Press, 1984.

[79] I. Narsky and F. C. Porter. *Statistical Analysis Techniques in Particle Physics: Fits, Density Estimation and Supervised Learning*. John Wiley & Sons, 2013.

[80] Y. Freund and R. Schapire. Experiments with a New Boosting Algorithm. *ICML*, 1996.

[81] P. Speckmayer, A. Höcker, J. Stelzer, and H. Voss. The Toolkit for Multivariate Data Analysis, TMVA 4. *Journal of Physics: Conference Series*, 219(3):032057, April 2010.

[82] http://cosmos.n.kanagawa-u.ac.jp/EPICSHome/index.html.

[83] http://sroesler.web.cern.ch/sroesler/dpmjet3.html.

[84] Y. Akaike. CALET Observational Performance Expected by CERN Beam Test. In *Proceedings of the 33rd International Cosmic Ray Conference*, Rio de Janeiro, 2013.

[85] F. Palma. Simulation Studies of the Expected Proton Rejection Capabilities of CALET. In *Proceedings of the 34th International Cosmic Ray Conference*, Hague, 2015.

[86] F. James. *Statistical Methods in Experimental Physics.* World Scientific Publishing, 2006.

[87] N. Cannady and M. L. Cherry. Gamma-Ray Observations with CALET: Exposure Map, Response Functions, and Simulated Results. In *Proceedings of the 34th International Cosmic Ray Conference*, Hague, 2015.

[88] M. N. Mazziotta and f. t. F.-L. Collaboration. Data Analysis for the Measurement of High Energy Cosmic Ray Electron/Positron Spectrum with Fermi-LAT. In *Proceedings of the 31st International Cosmic Ray Conference*, page 4, Lodz, July 2009.

[89] https://geant4.web.cern.ch/geant4/.

[90] S. Klein. Suppression of Bremsstrahlung and Pair Production due to Environmental Factors. *Reviews of Modern Physics*, 71(5):1501–1538, October 1999.

[91] J. Apostolakis, G. Folger, V. Grichine, et al. GEANT4 Physics Lists for HEP. In *2008 IEEE Nuclear Science Symposium Conference Record*, pages 833–836. IEEE, October 2008.

[92] P. D. Smith, R. E. Hughes, B. L. Winer, and T. W. Wood. Methods for Measuring the Cosmic-Ray Proton Spectrum With the Fermi LAT. In *2009 Fermi Symposium Proceedings*, page 4, December 2009.